Migration des fluides issus de la déshydratation des serpentinites : une étude naturelle et expérimentale

Maxime Clément

THÈSE POUR OBTENIR LE GRADE DE DOCTEUR DE L'UNIVERSITÉ DE MONTPELLIER

En Géosciences

École doctorale GAIA – Biodiversité, Agriculture, Alimentation, Environnement, Terre, Eau

Unité de recherche Géosciences Montpellier – UMR 5243

Migration des fluides issus de la déshydratation des serpentinites: une approche naturelle et expérimentale

Présentée par Maxime Clément

Le 02 Novembre 2018

Sous la direction de José Alberto Padrón-Navarta et Andréa Tommasi

Devant le jury composé de

M. José Alberto Padrón-Navarta, Chargé de Recherches, Géosciences Montpellier	Directeur de thèse
Mme. Andréa Tommasi, Directeur de Recherche, Géosciences Montpellier	Co-directrice de thèse
Loïc Labrousse, Professeur, Institut des Sciences de la Terre de Paris, ISTeP Paris	Rapporteur
Vicente López-Sánchez-Vizcaíno, Professor, Université de Jaén, Espagne	Rapporteur
Alberto Vitale Brovarone, Chargé de Recherches, IMPCMC Paris	Examinateur
Frédéric Gueydan, Professeur, Géosciences Montpellier	Examinateur et Président du Jury

UNIVERSITÉ DE MONTPELLIER

RÉSUMÉ

La migration de fluides peut être responsable de nombreux processus d'importance sociétale et économique puisqu'elle est associée à des dépôts de minerai où à la formation de volcans d'arc à éruption explosive. La migration de fluides issus des réactions de déshydratation des serpentinites est aussi associée à des changements de comportement rhéologique de ces serpentinites dans les zones de subduction. Ce changement de rhéologie peut être responsable du déclenchement de tremblement de terre dans les zones de subduction. Toutefois, le couplage entre propriétés mécaniques des serpentinites, migration de fluide et cinétique de réaction de déshydratation reste encore peu contraint à l'heure actuelle. Cette thèse apporte des contraintes supplémentaires sur les liens qui existent entre ces propriétés en combinant une étude de serpentinites déshydratées de manière naturelle, de manière expérimentale et en étudiant l'impact de la compaction, moteur de déplacement des fluides, lors de la déshydratation des serpentinites.

La déshydratation naturelle et la déshydratation expérimentale des serpentinites produisent des métapéridotites qui présentent des olivines granulaires ou allongées dans le plan de foliation. Ces deux types d'olivines montrent une forte orientation cristallographique préférentielle et une corrélation avec l'antigorite du fait du parallélisme de leurs axes [100] pour les olivines granulaires et de leurs axes [010] pour les olivines allongées avec les axes [001] de l'antigorite. Des marqueurs de déformations sont observés dans les métapéridotites foliées.

Les serpentinites déshydratées de manière naturelle et expérimentale montrent des plans de fractures dans lesquels les olivines ont des textures de croissance rapide. Dans le cas des fractures naturelles, l'orientation cristallographique préférentielle des olivines est forte et corrélée au plan de la veine.

La serpentinite partiellement déshydratée du massif de Cerro del Almirez montre occasionnellement des lamelles de clinoenstatite dans des grains d'orthoenstatite orientées aléatoirement qui peuvent potentiellement résulter d'une transformation martensitique (maclage mécanique) de l'orthoenstatite. Ces lamelles sont plus nombreuses dans la serpentinite complètement déshydratée et montrent deux orientations. La direction de contrainte calculée est orientée aléatoirement

dans la serpentinite partiellement déshydratée et présente une seule orientation dans l'autre serpentinite.

L'interprétation de ces résultats proposée dans cette thèse est que la migration de fluides est enregistrée par les textures des produits de réaction, notamment l'olivine. La migration lente et pervasive de fluides produit des olivines granulaires dont les orientations sont apparemment héritées de l'antigorite via des relations topotactiques (développement préférentiel des axes cristallographiques par croissance orientée entre deux minéraux). La migration focalisée de fluide change le mécanisme de croissance des grains conduisant à de la croissance orientée dans le plan de foliation ou dans le plan de la veine, sous l'effet du gradient de pression de fluides. L'extraction des fluides entraine une compaction qui expulse les fluides résiduels dans les pores et qui génère un champ de contrainte non-hydrostatique. Ce champ de contrainte est responsable de la déformation observée et de la transformation martensitique de l'orthoenstatite en clinoenstatite.

ABSTRACT

Fluid migration may be associated to several processes involved in ore deposit or the formation of forarc volcanoes that have explosive eruption. Fluid migration may also be also associated to change of rheological behavior of dehydrating serpentinite responsible of earthquakes triggering in subduction zones. However, the coupling between mechanical properties of dehydrating serpentinites, fluid migration and kinetics of dehydration reactions remains poorly constrained. This thesis provides new constraints on the link between these properties by combining a study on natural dehydrated serpentinites and experimentally dehydrated serpentinite and by evaluating the impact of metamorphic compaction, which drives fluids motion, on dehydrated serpentinites.

Both natural and experimental dehydration of serpentinites produce metaperidotites that shows granular olivines or olivines elongated in the foliation plane. Both types of olivine have strong crystal preferred orientation and are correlated to antigorite as it is visible with [100] axes of granular olivines and [010] axes of elongated olivines parallel to [001] axes of antigorite. Markers of deformation were observed in foliated metaperidotites.

Both naturally and experimentally dehydrated serpentinites shows fractures in which olivines have texture of rapid growth. Olivines from fractures in naturally dehydrated samples have strong crystal preferred orientation correlated to the plane of the fractures

Partially dehydrated serpentinite from Cerro del Almirez massif shows minor amount of clinoenstatite lamellae in orthoenstatite grains randomly oriented that may have been formed by martensitic transformation (mechanical twinning) of orthoenstatite. Completely dehydrated serpentinites at two meters of distance have higher amount of clinoenstatite that have two different orientations. Stress direction calculated is randomly oriented in partially dehydrated serpentinite and strongly oriented in completely dehydrated serpentinite.

Results are consistent and the interpretation proposed in this thesis is that fluid migration is recorded by textures of products of dehydration reactions. Slow and pervasive fluid migration produces granular olivines with crystal preferred orientation

correlated to crystal preferred orientation of antigorite by topotaxial relationships, which are fixed arrangements of crystallographic axes between two minerals due to oriented growth. Focused fluid migration change mechanisms of grain growth resulting in oriented growth of olivines in foliation plane or in plane of veins because of fluid pressure gradient. Fluid extraction lead to metamorphic compaction, which expulse residual fluids from the pores and triggered non-hydrostatic stress field. This non-hydrostatic stress field is responsible of deformation and the martensitic transformation of orthoenstatite to clinoenstatite.

REMERCIEMENTS

J’y suis arrivé !

8 ans d’études supérieures. Cela laisse songeur. Je me revois encore fraîchement débarqué du lycée dans un univers complètement inconnu qu’était l’université. Mon parcours est un peu inhabituel, étant donné qu’initialement je suis venu en géologie sur un coup de tête absolu. Jamais je ne me serai imaginé continuer en thèse à ce moment-là. Et jamais je ne regretterai ce coup de tête.

Après une année passée en science de la terre avec une expérience de terrain particulièrement traumatisante de cartographie en terrain sédimentaire, ma décision fut prise de me consacrer corps et âme à la pétrologie endogène. L’année suivante (L3 !) je me retrouvais donc à plancher (durement) sur tous les domaines qui y attrayaient. A la fin de la troisième année de Licence, je me suis rendu compte que j’étais totalement fasciné par les processus profonds de formation des roches et j’ai pris alors la décision de poursuivre en recherche. L’été de transition entre ma troisième année de Licence et le Master je me suis trouvé un stage de recherche fondamentale pour mes deux années de master sur la formation des sulfures dans les chondrites à enstatite (des processus profonds vous ai-je dis ?). A l’issue de ces deux années de cosmochimie, j’ai décidé qu’il était temps de me tourner vers de nouveaux horizons de recherche, ce qui m’a amené à postuler sur cette thèse.

J’en arrive donc aux deux premières personnes que je souhaite remercier sincèrement et le plus chaleureusement possible : José Alberto et Andréa. Merci à vous deux de m’avoir donné cette merveilleuse opportunité. Merci pour votre soutien, merci pour vos conseils, merci pour votre aide, merci pour votre patience, pour avoir pris le temps de m’expliquer les choses et de me les avoir ensuite répéter quand ça ne voulait pas rentrer (surtout toi José !) Tout le long de la thèse, je me suis senti extrêmement chanceux de vous avoir tous les deux comme encadrants et je m’en féliciterai encore probablement après. Je pense pouvoir dire de la manière la plus objective possible que je ne pouvais pas tomber mieux niveau encadrement.

Un énorme merci à Sylvie également ! Qui, bien que n’étant pas mon encadrante, m’a donné de très précieux conseil et a fait de moi (je crois ?) un meilleur expérimentaliste. Ou expérimentateur ? Je ne sais jamais. Mais grâce à toi je sais ce qu’est un pied à coulisse !

Merci aussi, à tous les gens avec qui j'ai été amené à travailler. Je ne pense pas que je serai exhaustif mais je pense pouvoir citer les principaux :

Merci à Fabrice pour m'avoir dépanné chaque fois que le besoin se présentait lors de mes longues (très longues…) sessions d'analyses EBSD et qui avait toujours un trait d'humour à partager. Crois moi, ça a fait une différence ; J'espère que tu auras l'occasion de t'amuser avec la nouvelle caméra

Merci à Christophe et Doriane, qui ont dû bossé comme des machines avec la quantité un peu élevée de lames minces que j'avais à faire préparer.

Merci à David, pour tes conseils et ton aide précieuse quand je coinçais (vraiment) sur MTEX

Merci à Bernard pour ton assistance lors des analyses à la microsonde électronique

Merci à Romain pour tes suggestions sur Malenco et pour les analyses XRD ;

Mais aussi aux autres personnes des laboratoires :

Fleurice, pour tout ce que tu as fait déjà pour moi avec les enseignements et ton aide + conseils sur le concours qui s'annonce

Philippe, pour m'avoir sorti une énorme épine du pied avec ma vacation non-reconnue et pour tes informations sur le concours, également

Merci à Emilien, pour ta sempiternelle bonne humeur et pour ta patience en toute circonstance. C'est le naturel des Lorrains ;

Merci à Manuel, pour nos discussions musicale passionnantes !

Merci à Benoit, Margot, Fabrice, Stéphane, Catherine, Hélène, José, Françoise, et tous les autres ;

Je remonte le temps à présent, et vers le Nord aussi accessoirement, en direction des gens du plateau de Brabois :

Merci à Yves de m'avoir donné un super stage de master et un voyage au Japon pour conclure (mais est-ce vraiment conclut ?).

Un gigantesque merci à Lydéric et François qui m'ont transmis la passion de la pétrologie et ses subtilités

Vous tous avez contribué à mon arrivée jusque là

Merci également à Manuel et Lucan, mes partenaires de bureau. Vous fûtes de forts agréables camarades ! Et le resterez.

Mais aussi tous les autres doctorants, qui formez un groupe soudé et joyeux ;

Merci à mes amis les plus proches : Alaïs, Lionel, et tous les gens à Strasbourg/Nancy (Juliette, Raph, Léa, Aurélie, Esteban, Olivier et les autres) ainsi que Simon et Nancy à Montpellier. Vous avez été mes points d'appuis sur lesquels je me reposais chaque fois que le besoin s'en faisait se ressentir. Je ne vous remercierai jamais assez d'avoir été là.

Merci à ma famille de m'avoir toujours poussé (parfois trop peut être…) à travailler comme un dingue pour atteindre mes objectifs. C'est clair que sans vous, je ne serai jamais allé aussi loin.

Enfin, merci à Florence. Tu as débarqué dans ma vie sans prévenir et tu l'as totalement changé. Le rideau de pluie grisâtre de mon monde s'est ouvert et tout est devenu brillant comme l'argent…Je n'ai pas de mots pour décrire le bonheur et le réconfort que tu m'apportes. Merci mille fois d'être là pour moi.

TABLE DES MATIERES

CHAPITRE I

INTRODUCTION

I. INTRODUCTION

1. LES FLUIDES

Un fluide se définit comme étant un milieu matériel qui se déforme de manière continue sous l'effet d'une contrainte cisaillante qui lui est appliquée. Ce terme regroupe en général les liquides et les gaz mais celui-ci est plus communément utilisé pour désigner des liquides, notamment en géologie. Dans cette discipline, le terme de « fluide » réfère le plus souvent à un milieu aqueux, c'est-à-dire essentiellement constitué d'eau mais dans lequel d'autres espèces volatiles comme le dioxyde de carbone ou le méthane peuvent être présentes en plus faible quantités (<35%). Les fluides en géologie interviennent dans de nombreux processus superficiels et profonds de la Terre et jouent un rôle important dans chacun d'eux. Cette étude étant focalisée sur les parties profondes de la terre, la liste des processus dans lesquelles les fluides interviennent sera portée sur les processus endogènes (processus « profonds ») et ne traitera pas des processus superficiels ni des processus affectant les fluides présents dans les météorites et les astéroïdes.

1.1. Intérêt des fluides en géologie

L'intérêt que les fluides suscitent est grand car ceux-ci sont impliqués dans de nombreux processus tels que le transfert de matière (Ague, 2013; Heinrich *et al.*, 1995) et de chaleur (Etheridge *et al.*, 1983; Ferry, 1980; Pruess, 2008), le dépôt de métaux d'intérêts économiques (Ding *et al.*, 2018; Fyfe, 1987; Morales *et al.*, 2016) ou l'extraction du gaz et du pétrole par fracturation hydraulique (Horton, 2012; Segall, 1989). Dans les zones de subduction, les fluides vont également être responsables de tremblements de terre potentiellement dangereux (Hacker, 2003; Peacock, 2001; Wada *et al.*, 2008), du transfert d'éléments de la plaque plongeante vers la plaque surjacente (Galvez *et al.*, 2015, 2016; Manning, 2004), de la serpentinisation du manteau surjacent (Bostock *et al.*, 2002; Hyndman and Peacock, 2003) et produire la fusion partielle de ce dernier, entraînant la formation de volcans d'arc (Defant and Drummond, 1993; Elliott *et al.*, 1997; Kelemen *et al.*, 2003) à éruptions explosives. Tous les processus évoqués ci-dessus sont provoqués par le déplacement de masse d'eau et d'autres espèces volatiles. Mieux comprendre les mécanismes de migration de ces fluides permettrait de mieux comprendre le déclenchement de ces processus, parmi lesquels plusieurs ont des enjeux sociétaux importants.

1.2. Origines des fluides

Les fluides en géologie peuvent avoir différentes origines. Comme dit précédemment, leur nature est avant tout aqueuse. Cette eau peut provenir de la pluie par infiltration superficielle dans les roches sédimentaires ou de la mer par le même processus (Hanor, 1994). À haute température (<400°C), l'eau de mer provoque l'altération hydrothermale des péridotites mantelliques affleurant au niveau du plancher océanique, produisant des serpentinites (Barnes and Sharp, 2006; Janecky and Seyfried, 1986; Lienert and Wasilewski, 1979; Malvoisin *et al.*, 2012; Mével, 2003; Moody, 1976).

La serpentine est une famille de quatre minéraux : la lizardite, le chrysotile, la serpentine polygonale et l'antigorite qui sont des formes hydroxylées (qui ont incorporé de l'hydrogène dans leur structure) de minéraux ultramafiques tels que l'olivine et le pyroxène. La lizardite et le chrysotile sont des variétés de la serpentine de basse température-basse pression tandis que l'antigorite est la forme de haute pression-haute température, la transition entre la lizardite/chrysotile et l'antigorite se faisant à 200-300°C environ (Evans, 2004; Mellini, 1986; Schwartz *et al.*, 2013). L'intérêt de l'antigorite est qu'elle peut incorporer jusqu'à 11-13 wt% d'eau dans sa structure dans les conditions P-T du manteau (Ulmer and Trommsdorff, 1995). Lors de la subduction de la lithosphère océanique, sa déstabilisation libère d'importants volumes d'eau et constitue donc une source importante de fluides dans le manteau (Scambelluri *et al.*, 2001, 2004; Schmidt and Poli, 2013 ; Ulmer and Trommsdorff, 1995 ; Reynard, 2013 ; Nagaya, 2014). Des volumes d'eau importants sont également relâchés lors de la déshydratation des serpentinites (Ferry, 1995 ; Mellini, 1987 ; Frost, 1978 ;Bakke and Korneliussen, 1986). En plus de libérer d'importants volumes d'eau, la déshydratation de l'antigorite produit également des minéraux secondaires. Des études expérimentales (Ulmer and Trommsdorff, 1999) et sur des roches naturelles (Frost, 1975; Garrido *et al.*, 2005; Nagaya *et al.*, 2014; Padrón-Navarta *et al.*, 2011; Trommsdorff and Evans, 1972) montrent qu'à basse pression (< 1 GPa) et haute température (>550°C), l'assemblage minéralogique produit correspond à de l'olivine et du talc. A plus haute pression et plus haute température, les minéraux produits par déshydratation sont de l'olivine et de l'enstatite (**Fig.** 1).

Les serpentinites à antigorite étant des roches riches en eau, c'est sur ce processus de déshydratation de l'antigorite que cette étude se focalisera afin de mieux comprendre les mécanismes de migration de fluides.

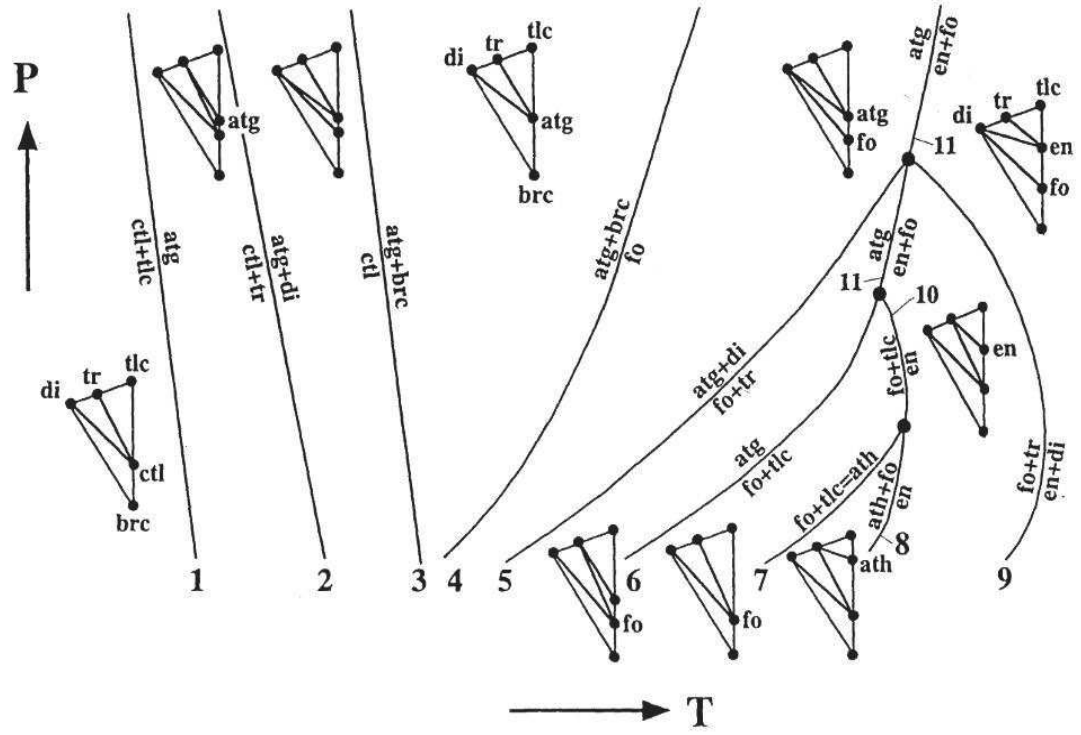

Figure 1 - Diagramme de phase du système CMSH et chemographie projetée depuis le pôle H_2O, d'après Ulmer and Trommsdorff (1999)

1.3. Fluides et propriétés mécaniques des serpentinites

Les propriétés mécaniques des serpentinites qui se déshydratent et la migration de fluides sont étroitement liées. En effet, de par leur simple différence de densité avec les roches, les fluides vont avoir tendance à remonter vers la surface dans une colonne de roche (Walther and Orville, 1982). Les serpentinites ont des propriétés rhéologiques importantes et largement étudiées telles que leurs propriétés élastiques responsables de la diminution de la vitesse des ondes sismiques dans les zones de subduction (Bezacier *et al.*, 2010; Mainprice and Ildefonse, 2009; Reynard, 2013) ou leur faible viscosité qui va permettre de concentrer la déformation et diminuer les contraintes empêchant la propagation de séismes dans les zones de subduction (Hilairet *et al.*, 2007). Cependant, les propriétés mécaniques des serpentinites qui se

déshydratent liées à la migration de fluides qui seront plus importantes pour cette étude sont la porosité, la perméabilité et la rhéologie.

1.3.1. Porosité et perméabilité

La porosité est le volume d'espace non solide disponible dans une roche et la perméabilité est la capacité d'une roche à laisser passer un fluide. Elle dépend donc du volume de pores connectés. Lors des réactions de déshydratation des serpentinites et la libération de fluides, ces propriétés changent. En effet, au cours de la déshydratation, des volumes de vide sont créés (=porosité). Ceci est dû au fait que les minéraux produits (olivine, talc ou enstatite, **Fig.** 1) occupent un volume plus petit et contribuent à augmenter la densité de la matrice solide de la serpentinite réagie (métapéridotite). Le volume de vide quant à lui, augmente progressivement et est rempli par les fluides produits par la déshydratation (Bedford *et al.*, 2017; Putnis, 2015) (**Fig.** 2, d'après le programme PerpleX).

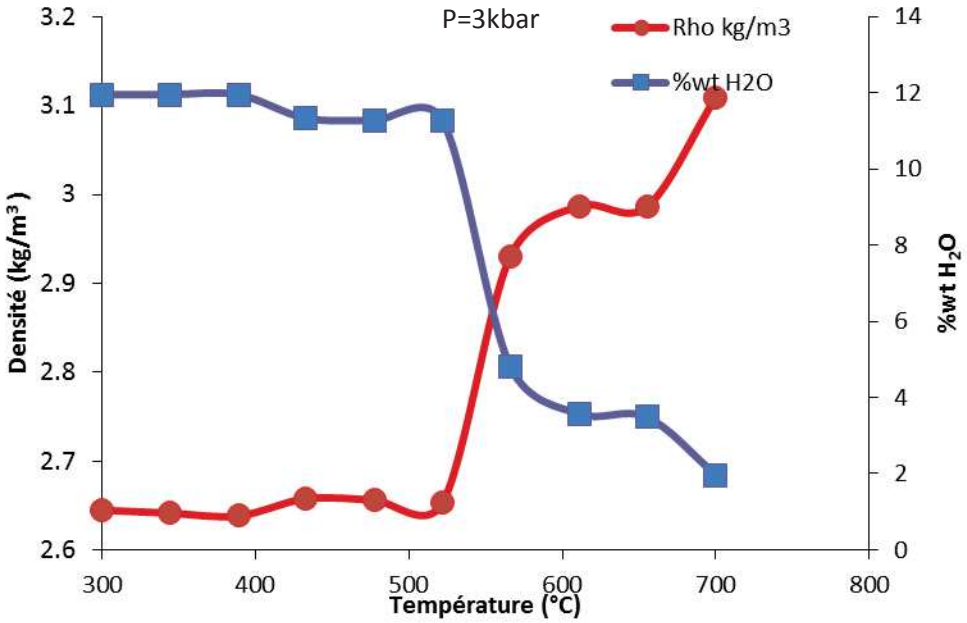

Figure 2 - Evolution de la densité et de la quantité d'eau présente dans une serpentinite au cours de la déshydratation

Les fluides ont également une compressibilité plus importante que la matrice solide. Leur densité est donc fonction de la pression de confinement qui elle-même dépend de la perméabilité (Connolly, 1997). La perméabilité est également la propriété qui va contraindre la capacité des fluides à se déplacer grâce au gradient hydraulique et qui est décrite grâce à la relation empirique de Darcy, liant la vitesse de circulation de fluides « v » au gradient de pression « *p* »:

$$\varphi \mathrm{v} = \frac{k}{\mu}\left(-\nabla p + f\right) \quad (1)$$

Où φ représente la porosité, *k* est la perméabilité, μ est la viscosité et f est la somme des forces extérieures (Jamtveit and Hammer, 2012). D'une manière générale, il existe deux types de circulation de fluides : « chenalisée » ou « pervasive ». La circulation « chenalisée » correspond à la circulation de fluides selon des conduits de très grande perméabilité (Ague, 2013). Elle se produit aussi lorsque la pression de fluides dans les pores excède la pression de confinement (=pression lithostatique) provoquant une fracturation de la matrice solide et un échappement rapide d'un gros volume de fluide selon un plan préférentiel (Jabaloy-Sánchez *et al.*, 2015; Nakashima, 1995; Padrón-Navarta *et al.*, 2010; Plümper *et al.*, 2017). Cela arrive lorsque le milieu de circulation est peu perméable ce qui conduit la pression de fluides à augmenter localement de plus en plus. La circulation « pervasive » en revanche se produit dans un milieu plus perméable et correspond à une circulation lente et progressive d'un plus petit volume de fluide le long des joints de grains, à l'échelle microscopique (Ague, 2013; Etschmann *et al.*, 2014; Ferry, 1994) (**Fig.** 3).

(a) Circulation chenalisée **(b) Circulation pervasive**

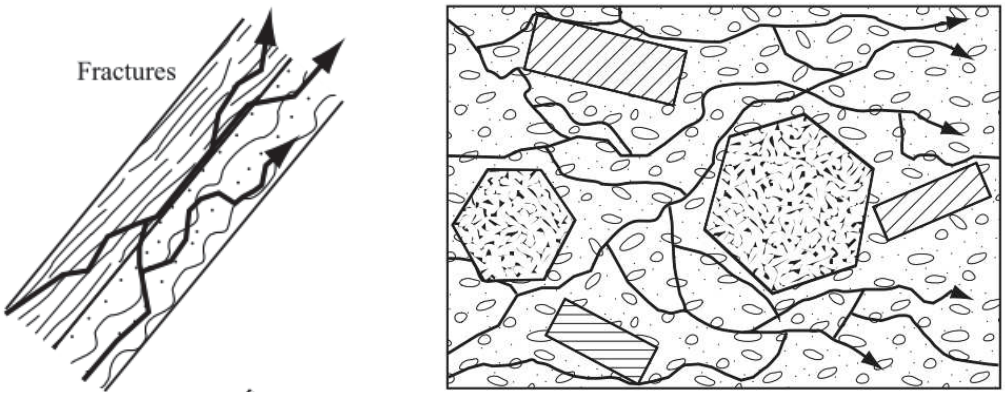

Figure 3 - Mode de circulation des fluides: chenalisée (a) et pervasive (b) (Ague, 2013)

Les serpentinites sont des roches généralement foliées (les minéraux sont orientés dans un plan). Cette foliation produit une anisotropie de perméabilité selon laquelle les fluides vont se déplacer préférentiellement (parallèle au plan de foliation) ou moins préférentiellement (perpendiculaire au plan de foliation). La porosité et la perméabilité des serpentinites sont encore mal contraintes à haute pression. Alors que la porosité des roches de la croûte inférieure serait estimée à 0.046% et la perméabilité à 10^{-23} m² d'après le modèle numérique de Connolly (1997), les

serpentinites auraient une porosité de 10^{-3} % à 10^{-4} % et une perméabilité de $6.3x10^{-24}$ m² parallèle à la foliation et $4.7x10^{-25}$ m² perpendiculaire à la foliation à 1GPa (Kawano *et al.*, 2011), les deux étant reliées par l'équation :

$$k = k_0 \left(\frac{\varphi}{\varphi_0}\right)^{\alpha} \quad (2)$$

Avec k la perméabilité, k_0 la perméabilité initiale, φ la porosité, φ_0 la porosité initiale et α est le facteur de sensibilité de la porosité. En plus de leur évolution pendant la réaction de déshydratation, ces propriétés vont également être modifiées si une serpentinite qui réagit subit une déformation. En effet, la perméabilité de la serpentinite diminue 10^{-18} à 10^{-20} m² sous l'effet d'une déformation compressive de 50 MPa (Kawano et al., 2011).

1.3.2. Rhéologie de la serpentinite

La rhéologie est la capacité d'une roche à se déformer sous l'effet d'une contrainte. La porosité et la perméabilité d'une serpentinite peuvent être modifiées sous l'effet d'une déformation. En effet, en fonction des conditions P-T et de l'intensité de la contrainte, une serpentinite peut se déformer : (1) soit de manière ductile (déformation plastique) par compaction/dilatation qui va réduire/augmenter la porosité, (2) soit de manière fragile (déformation cassante) et augmenter ainsi sa perméabilité au cours des réactions de déshydratation.

La rhéologie relie donc la contrainte (σ) et la déformation. Une contrainte est une force exercée sur une surface qui peut générer une déformation si celle-ci est appliquée suffisamment longtemps ou si elle est suffisamment forte (dépassant la limite d'élasticité). Si la différence entre la contrainte principale σ_1 et la contrainte minimale σ_3 (=contrainte différentielle) est nulle alors il n'y pas de variation de forme, mais potentiellement une densification du solide. Si la différence est non nulle, la déformation se produit. Une déformation impliquant un aplatissement d'un solide et son élongation perpendiculaire à l'aplatissement est appelée « cisaillement pur » tandis qu'une déformation impliquant la translation l'un par rapport à l'autre des plans d'un solide parallèle entre eux est appelée cisaillement simple (**Fig.** 4).

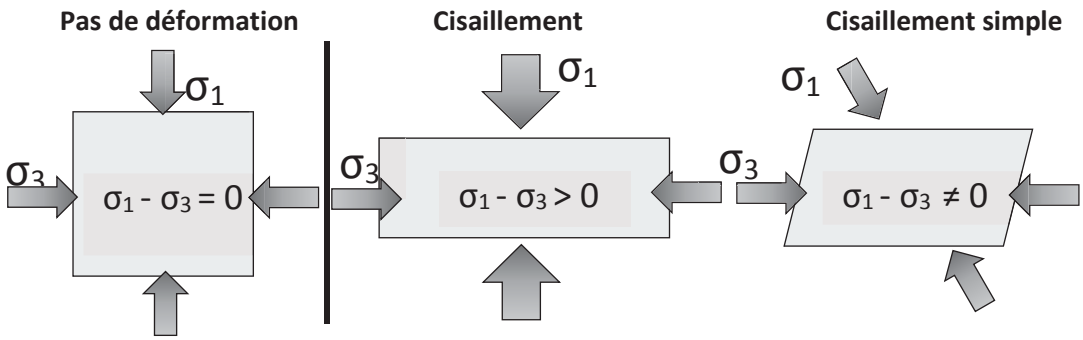

Figure 4 - Exemples de différents modes de déformation en fonction des contraintes appliquées

Il existe 3 régimes de déformation : le régime élastique dans lequel un solide va se déformer mais reprendre sa forme initiale si les contraintes ne sont plus appliquées, le régime visqueux dans lequel un solide se déforme de manière ductile et un régime fragile dans lequel le solide se fracture, ces deux déformations étant irréversibles. L'augmentation de la pression et de la température permet en général d'élargir le champ du régime ductile et d'empêcher qu'une roche se fracture sous l'effet d'une contrainte trop forte. Toutefois, dans le cas des serpentinites, l'élévation de température va entrainer leur déshydratation et un changement de son comportement rhéologique inhabituel, car les roches réagies vont devenir fragiles (Raleigh and Paterson, 1965). Ce phénomène a été décrit comme le « dehydration embrittlement » et fait l'objet d'un débat à l'heure actuelle (Gasc *et al.*, 2011) car dans les zones de subduction, la serpentinite se déforme de manière ductile au niveau de la partie peu profonde mais finit par se déshydrater avec l'augmentation de la température en profondeur et devenir fragile, provoquant potentiellement des tremblements de terre (Hacker, 2003; Jung *et al.*, 2004; Peacock, 2001) (**Fig.** 5).

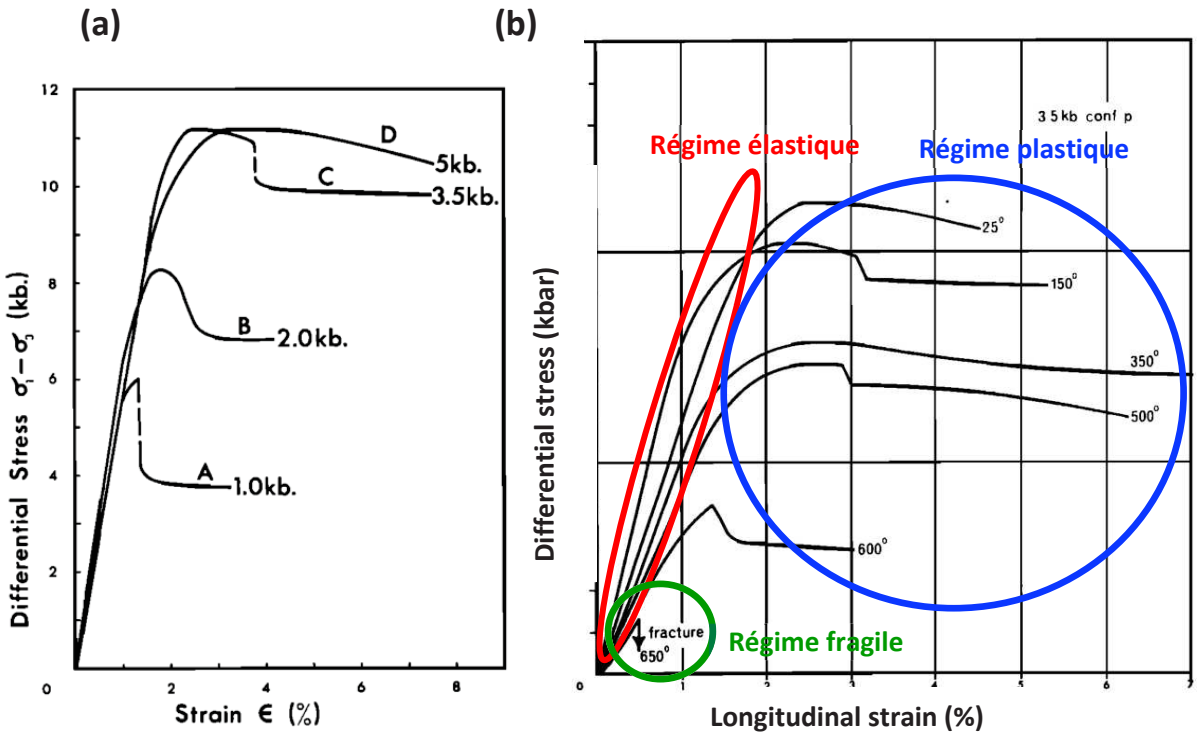

Figure 5 - Contrainte différentielle en fonction du taux de déformation pour (a) différentes pression de confinement (b) différentes températures. Modifié d'après Raleigh et Paterson (1965)

Des études expérimentales plus récentes et réalisées dans des conditions similaires à celles des zones de subduction ont cependant montré que la serpentinite pouvait adopter un comportement mixte ductile/fragile (Proctor and Hirth, 2015) voire un comportement complètement ductile (Amiguet *et al.*, 2014; Chernak and Hirth, 2010; Hilairet *et al.*, 2007) (**Fig.** 6).

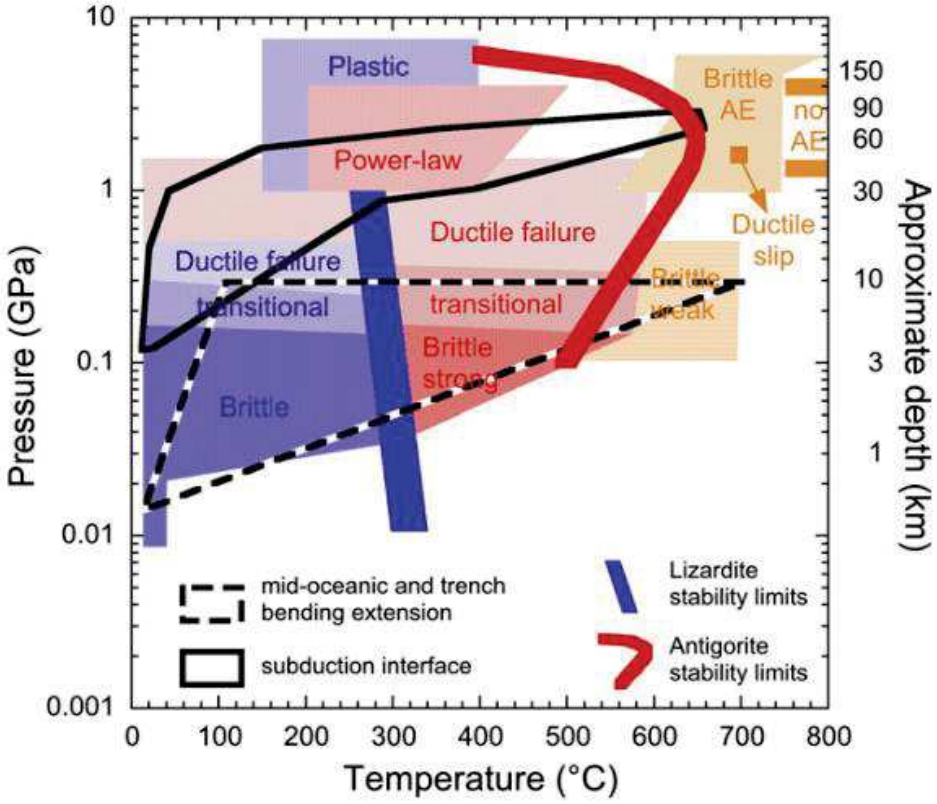

Figure 6 - Résumé des comportements rhéologiques de la serpentinite en fonction des conditions P-T (d'après Reynard, 2013)

Ainsi, connaître le comportement rhéologique de la serpentinite permet de comprendre dans une certaine mesure comment les fluides produits par sa déshydratation et stockés dans les pores vont s'en échapper.

1.3.3. Les modes de la migration de fluides

Différents modes de la migration des fluides existent. Un mode important de la migration de fluide repose sur le gradient de pression de fluide. Les fluides se déplacent vers le volume de pores connectés où la pression de fluide est moins importantes (Equation 1). Les fluides peuvent également être mis en mouvement par convection thermique (Etheridge *et al.*, 1983). Toutefois, les fluides issus des réactions de déshydratation ont un mode de circulation particulier qui a été décrit par Connolly (1997, 2010) : le « porosity wave ». Ce modèle décrit numériquement

comment les fluides des roches qui se déshydratent vont se propager. Comme dit dans les parties précédentes, la porosité créée au cours de la réaction de déshydratation se remplit de fluides. Si la pression de fluides dans les pores et supérieure à la pression de confinement (= la pression lithostatique), alors deux cas sont possibles : (1) la matrice solide de la serpentinite se dilate par des processus de déformation élastique ou ductile, permettant une circulation de fluide « pervasive » (2) la pression de fluide est localement trop élevée par rapport à la pression de confinement déclenchant une hydrofracturation et une circulation de fluide « chenalisée ». L'élévation de pression de fluide se déroule généralement au niveau d'une couche peu perméable de roche au contact de laquelle les fluides vont migrer selon l'un ou l'autre de ces processus. D'un autre côté, si la pression de fluide dans les pores est inférieure à la pression de confinement, alors la matrice solide va se compacter (par déformation élastique ou ductile), propulsant les fluides résiduels vers des zones de pores non compactées qui se situent généralement au front de réaction où les serpentinites se déshydratent et où la porosité se créée. Ces mécanismes de compaction/dilatation sont couplés et permettent aux fluides de migrer par cycles de compression/ dilatation de la matrice solide de la serpentinite au cours de la réaction (**Fig.** 7).

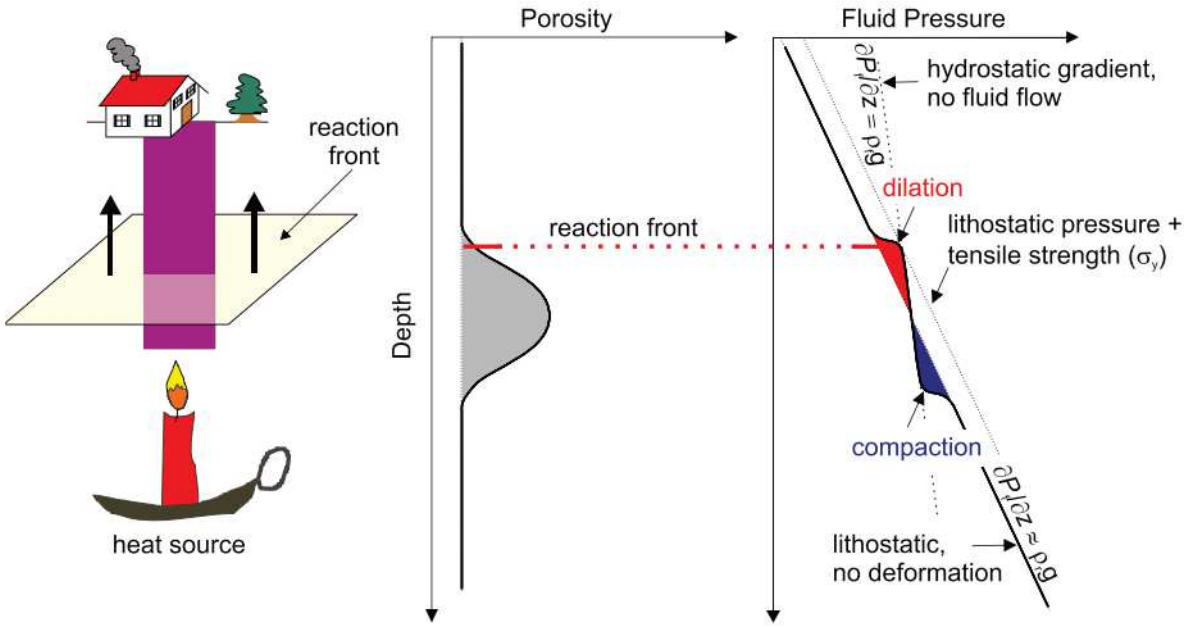

Figure 7 - Résumé du mécanisme du "porosity wave" décrivant les cycles de compression/dilatation de la matrice solide d'une roche qui se déshydrate (d'après Connolly, 1997; 2010)

1.4. Migration de fluides et taux de réaction

La partie précédente a montré que les propriétés mécaniques des serpentinites et la migration de fluide étaient liées : la porosité correspond à l'espace de stockage de fluides issus de déshydratation de la serpentinite, la perméabilité contrôle l'orientation du déplacement des fluides et la rhéologie de la serpentinite qui se transforme va déterminer si les fluides se déplacent de manière « pervasive » ou « chenalisée ». A cette relation, s'ajoute également le taux de réaction. En effet, des modèles numériques (Lasaga, 1989; Miller *et al.*, 2003; Wang and Wong, 2003) et des expériences en laboratoire (Llana-Funez *et al.*, 2007, 2012) ont montré que le taux de réaction était lié à la migration de fluides : lorsque les fluides migrent, la pression de fluide diminue tandis que la pression de confinement reste constante ce qui conduit à augmenter l'affinité de la réaction (= la différence d'énergie libre de Gibbs entre les réactifs et les produits) (Pattison *et al.*, 2011). Pour compenser cet excès d'énergie, le taux de réaction augmente et les minéraux produits lors de la déshydratation se forment. Naturellement, plus le volume de fluide qui s'échappe est grand, plus l'excès d'énergie qui doit être compensée est grand et donc plus le taux de réaction est rapide et important, et inversement (**Fig.** 8).

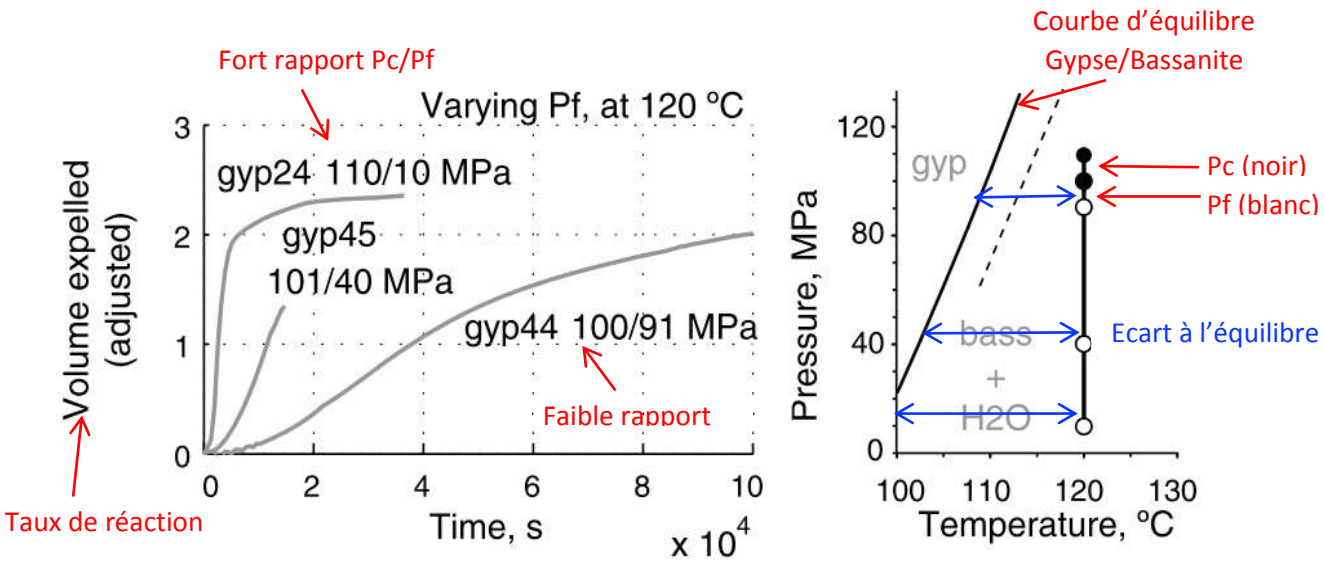

Figure 8 - Modifié d'après Llaña-Funez et al (2012): Taux de réaction de déshydratation du gypse (% de volume d'eau expulsé) en fonction du temps (s) pour 3 rapport de pression de confinement (Pc)/pression de fluides(Pf). Plus le rapport est grand, plus le taux de réaction est rapide et important. Le diagramme de phase à droite illustre ces différences par rapport à l'équilibre

Ainsi, en fonction de la différence entre la pression de confinement et la pression de fluide, le taux de réaction est soit faible et lent, soit important et rapide. Cela signifie que les minéraux produits par déshydratation de la serpentinite pourraient avoir des textures différentes en fonction de la pression de fluide, diminuant lentement dans le cas d'une circulation « pervasive » ou rapidement dans le cas d'une circulation « chenalisée ». C'est ce qu'ont suggéré Padrón-Navarta *et al.*, (2010, 2011, 2015) à partir de l'étude des serpentinites déshydratées du massif de Cerro del Almirez, en Espagne. Ces auteurs ont proposé que les textures de croissance rapide de type spinifex des olivines pouvaient être associées à des migrations rapide d'importants volumes de fluide (circulation « chenalisée » par hydrofracturation) tandis que les textures de croissance lente de type granoblastique pouvaient être associées à la migration lente de petits volumes de fluide (circulation « pervasive » par compaction de la porosité) (**Fig.** 9).

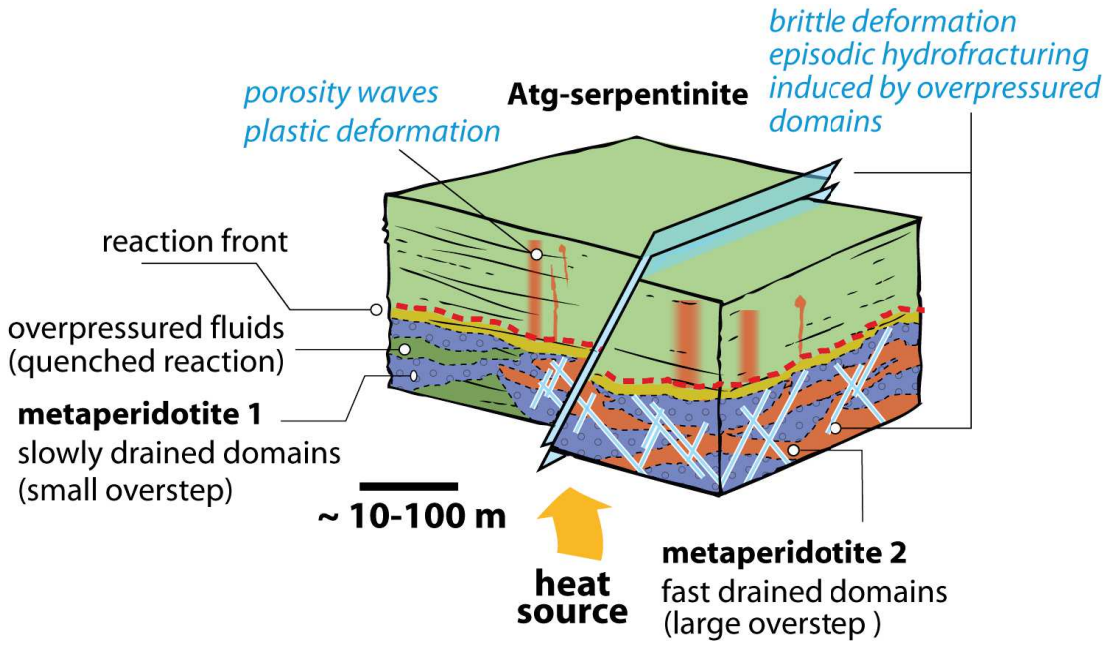

Figure 9 - Modèle d'échappement des fluides selon (Padrón-Navarta et al, 2011). Les textures de croissance rapides sont associées au déplacement de rapide et importants volume de fluides tandis que les texture de croissance lente sont associées à de la circulation lente et « pervasive ».

En plus de contrôler potentiellement la texture des minéraux produits par déshydratation de l'antigorite, la compaction de la porosité à l'origine de la circulation de fluide « pervasive » serait également responsable du renforcement de l'orientation des minéraux prograde, héritée de l'antigorite (Padrón-Navarta *et al.*, 2015). Cet héritage d'orientation cristallographique entre l'antigorite et les minéraux prograde repose en partie sur le processus de dissolution/reprécipitation largement décrit dans

la littérature (Jonas *et al.*, 2014; Nakamura and Watson, 2001; Pedrosa *et al.*, 2016; Putnis, 2002; Putnis and John, 2010; Putnis and Putnis, 2007; Ruiz-Agudo *et al.*, 2014; Xia *et al.*, 2009). Au cours de ces processus, un minéral en déséquilibre dans son environnement (comme l'antigorite qui se déshydate) commence à se dissoudre au niveau de ses bords et cristallise un minéral prograde (l'olivine, le talc où la chlorite, à basse pression) ayant la même orientation cristallographique que le minéral parent. En effet, la matière perdue par dissolution du minéral parent correspond à quelques couches atomiques et ne se solubilise pas dans le fluide en présence, qu'il soit issu de la déshydratation ou qu'il soit extérieur à la réaction. L'accumulation locale de matière dissoute produit une sursaturation locale du fluide. L'équilibre à l'interface entre le minéral et le fluide devenu localement sursaturé se rétablit avec la nucléation et la croissance topotactique d'un nouveau minéral plus stable à la surface du minéral parent. Toutefois, si la solubilité du minéral parent est plus grande que celle du minéral produit, ce dernier précipite moins que le minéral parent qui se dissout. Cela créée de la porosité dans le minéral produit permettant au fluide de continuer à interagir avec le minéral parent et à le dissoudre (Ruiz-Agudo *et al.*, 2014) (**Fig.** 10).

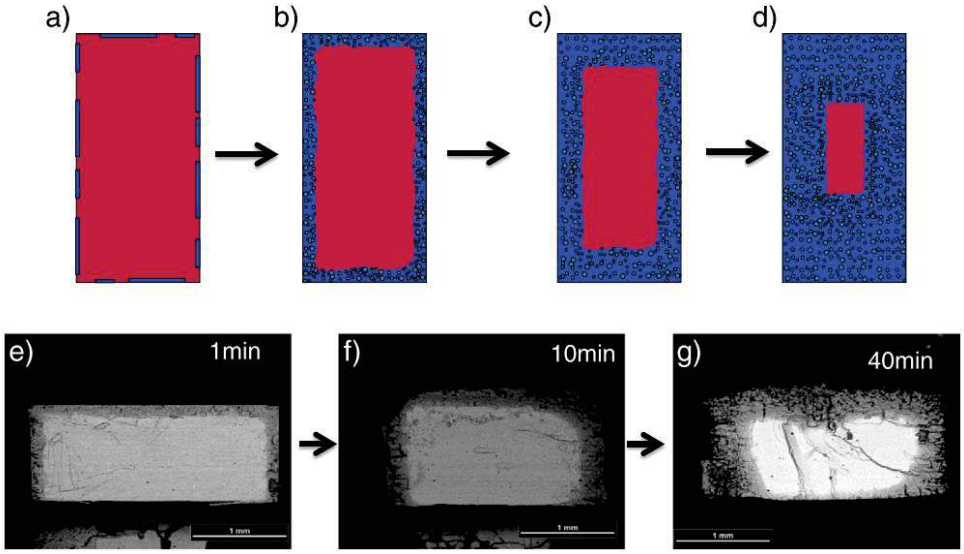

Figure 10 - Modifié d'après Ruiz-Agudo et al (2014). (a-d) Schéma d'un processus de dissolution-précipitation d'un solide. En rouge le minéral parent en déséquilibre avec un fluide, en bleu le minéral produit avec la porosité permettant au fluide de continuer à interagir avec le minéral parent. (e-f) Illustration du schéma avec un cas naturel de cristal de KBr remplacé par un cristal de KCl

Dans le cas d'une réaction de déshydratation de l'antigorite, cela signifie que les produits de réaction comme l'olivine sont susceptibles d'avoir leur orientation

contrôlée par celle de l'antigorite qui se déshydrate. En effet, cette relation a été observée dans des serpentinites déshydratées du massif de Cerro del Almirez (Espagne) entre l'axe [001] de l'antigorite et les axes [100] et [010] de l'olivine (Padrón-Navarta *et al.*, 2015) ainsi que dans des serpentinites de Valmalenco (Italie) entre l'axe [001] de l'antigorite et l'axe [100] de l'olivine (Morales *et al.*, 2018). Cet arrangement cristallographique entre l'antigorite et l'olivine produite peut être modifié si la serpentinite déshydratée subit postérieurement un épisode de déformation ductile, masquant ainsi l'information de l'héritage de la texture de la serpentinite par les produits de déshydratation.

2. PROBLEMATIQUE ET OBJECTIFS DE LA THESE

La problématique principale de cette thèse est de vérifier s'il est possible d'identifier le type de migration de fluide en fonction de la texture des produits de la déshydratation comme suggéré par Padrón-Navarta et al. (2011) mais à plus grande échelle (kilométrique) contrairement à l'étude de ces auteurs qui portait sur une lentille de quelques dizaines de mètres. Le but est d'essayer d'extrapoler ensuite l'interprétation des résultats aux zones de subduction, siège de nombreux processus d'importance sociétale cités précédemment, puisque l'essentiel des échantillons de cette étude sont issus d'une déshydratation à plus basse pression et sans déformation.

Ce chapitre a résumé les connaissances préexistantes sur les différents modes d'échappement des fluides, les propriétés mécaniques des serpentinites et les taux de réactions auxquels en fonction de la pression de fluides. Cependant, la relation entre la migration de fluide, les propriétés mécaniques des serpentinites, et le taux de réaction est encore mal contrainte. En effet, ces propriétés sont dynamiques et ont des effets qui peuvent être rétroactifs les unes sur les autres : pour que le taux de réaction soit maintenu et que les fluides soient produits, il faut que ceux-ci puissent être extraits du système. Cette migration dépend du volume de pores connectés mais leur présence dépend (1) de la pression de confinement, (2) de la rhéologie de la serpentinite qui se déshydrate et (3), du volume de fluide dans les pores et donc du taux de réaction (**Fig.** 11).

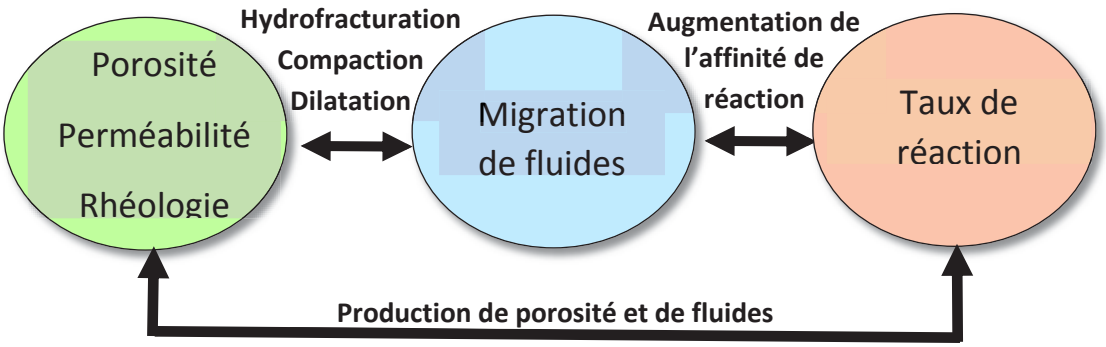

Figure 11 - Résumé des interactions possibles entre propriétés mécaniques des serpentinites, migration de fluide et taux de réaction

L'objectif de cette thèse est donc d'apporter de nouvelles contraintes sur les relations entre la migration de fluide (pervasive et focalisée), la texture des minéraux produits par leur déshydratation (granoblastique et texture hors-équilibre) et l'évolution des propriétés mécaniques (porosité/perméabilité) des serpentinites qui se déshydratent à travers une étude naturelle et une étude expérimentale des serpentinites déshydratées dans des contextes géodynamiques tels que les zones de subduction et le métamorphisme de contact.

Le deuxième chapitre de cette thèse présentera la démarche scientifique et la stratégie adoptée pour déterminer si la migration de fluide peut être identifiée via les textures des roches déshydratées naturellement et expérimentalement. Le troisième chapitre présentera l'étude des serpentinites de Val Malenco (Italie) déshydratées naturellement au contact de l'intrusion de la tonalite Bergell avec l'évolution des réactions de déshydratation et les textures associées à l'échelle du kilomètre. Le quatrième chapitre sera consacré à la présentation d'une série d'expériences de déshydratation de serpentinites dans la presse Paterson sans déformation appliquée et en conditions de drainage, le but étant de reproduire expérimentalement le métamorphisme de contact de Val Malenco. Le cinquième chapitre focalisera sur l'impact de la compaction métamorphique sur la texture des métapéridotites produites par la réaction de déshydratation et sur l'estimation des contraintes générées à l'échelle du grain à partir de l'étude de la transformation martensitique de l'orthoenstatite en clinoenstatite dans les métapéridotites du massif de Cerro del Almirez. Le dernier chapitre fera une synthèse des principales conclusions tirées de ces chapitres et proposera les perspectives d'études possibles à partir des processus décrits.

CHAPITRE II

DÉMARCHE SCIENTIFIQUE ET METHODOLOGIE

II. DÉMARCHE SCIENTIFIQUE ET MÉTHODOLOGIE

Afin de mieux contraindre les relations entre migrations de fluides et texture des minéraux produits par déshydratation de l'antigorite, une approche d'analyses à multi-échelle a été employée : des observations de terrains, des observations au microscope optique, et des observations au microscope électronique/EBSD. La réalisation d'expériences a été réalisée de manière à reproduire la déshydratation des serpentinites de Val Malenco et de comparer les résultats aux échantillons naturels.

La première partie abordée de ce chapitre concerne la méthode d'échantillonnage réalisée sur le terrain à Val Malenco (Italie) afin de déterminer l'orientation des serpentinites et des métapéridotites. La seconde porte sur l'utilisation de la presse Paterson qui a servi à réaliser les expériences de déshydratation de l'antigorite. Enfin, la troisième porte sur le principe de fonctionnement des méthodes analytiques utilisées et les techniques numériques employées pour traiter les données EBSD et modéliser les relations de phases ainsi que les propriétés thermodynamiques des serpentinites qui se déshydratent.

1. MESURES ET ECHANTILLONNAGE DE TERRAIN

1.1. Echantillonnage orienté

Une partie roches prélevées sur le terrain à Val Malenco ont été préalablement orientées (50 sur 122). L'objectif de cet échantillonnage orienté était de suivre en continu l'orientation des serpentinites et celle des métapéridotites afin de déterminer des variations entre les deux à l'échelle du kilomètre. Les structures mesurées sont la foliation et la linéation des serpentinites et métapéridotites. La mesure de la foliation d'une roche se réalise en reportant à la fois l'azimut du plan de foliation (= la différence entre la direction de l'horizontale du plan et la direction du Nord) ainsi que l'orientation et l'inclinaison du pendage du plan par rapport à l'horizontale. La linéation, qui correspond à l'allongement des minéraux dans le plan de foliation (ici, l'allongement de la magnétite dans la serpentinite et la métapéridotite) se mesure de manière similaire à la foliation en reportant son azimut, son inclinaison ainsi que la direction de son inclinaison (**Fig.** 12).

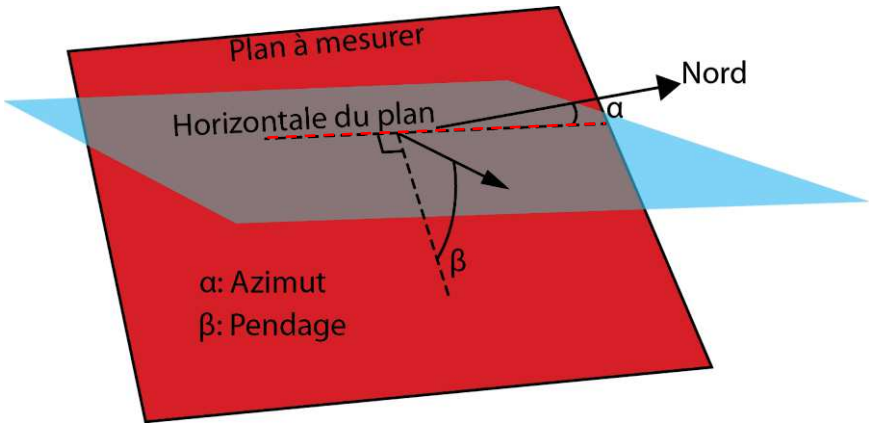

Figure 12 - Schéma des mesures de l'orientation et de l'inclinaison d'un plan

Les plans des veines ont également été orientés, les mesures ayant été réalisées de la même manière que pour les plans de foliation. Les mesures d'azimut de plan sont comprises entre 0° et 360° et celles du pendage entre 0° et 90°. Une fois les mesures de la foliation d'un échantillon effectuée, la mesure d'un plan de référence d'une surface de l'échantillon fut également mesurée, afin de pouvoir repositionner l'échantillon dans le laboratoire pour la réalisation de sa lame mince.

1.2. Préparation des lames minces

La réalisation des lames minces nécessita de repositionner les échantillons dans leur orientation géographique d'origine. Une fois les échantillons réorientés, la trace de la coupe correspondant au plan Est-Ouest fut dessinée sur eux. La découpe selon cette trace fut réalisée à l'aide s'une scie diamantée de telle sorte que le plan de la lame correspondait ainsi au plan Est-Ouest du terrain (**Fig.** 13).

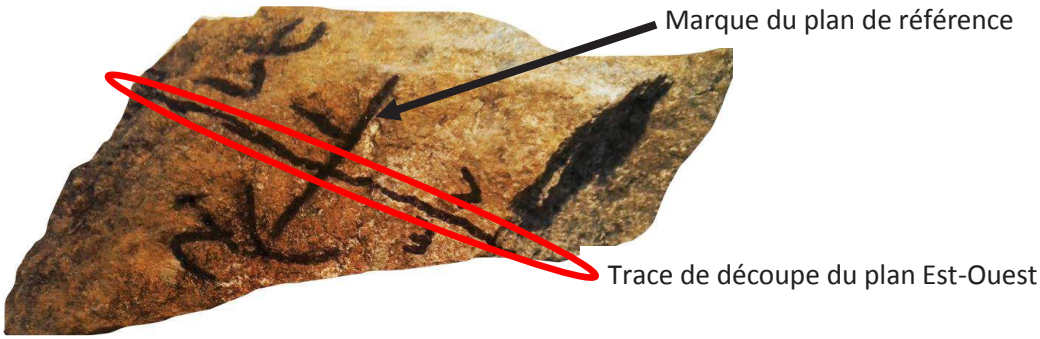

Figure 13 - Photo schématique de l'orientation et du plan de découpe des échantillons orientés

Une fois la découpe effectuée selon le plan Est-Ouest, un sucre d'environ 30 mm de large sur 45 mm de long fut découpé pour ensuite être imprégné sous vide pendant 24 h puis avec une résine diluée dans 1% d'acétone pendant encore 24 h. Le sucre fut ensuite chauffé à 50 °C pendant 12 h puis son épaisseur fut diminuée à --140 µm. Une nouvelle induration fut ensuite réalisée pendant 12 h puis la mise en épaisseur à 30 µm fut effectuée avec une rodeuse et de la poudre de carbure de silicium à 600 et 1200 µm. La dernière étape de préparation d'une partie des lames (Tableau en Annexe) fut le polissage pour les analyses par microscopie électronique, microsonde électronique et par diffraction des électrons rétrodiffusés. Celui-ci a été réalisé pendant 4 h avec de la pâte diamantée et une pression appliquée de 600 g à 240 g.

2. STRUCTURE ET FONCTIONNEMENT DE LA PRESSE PATERSON

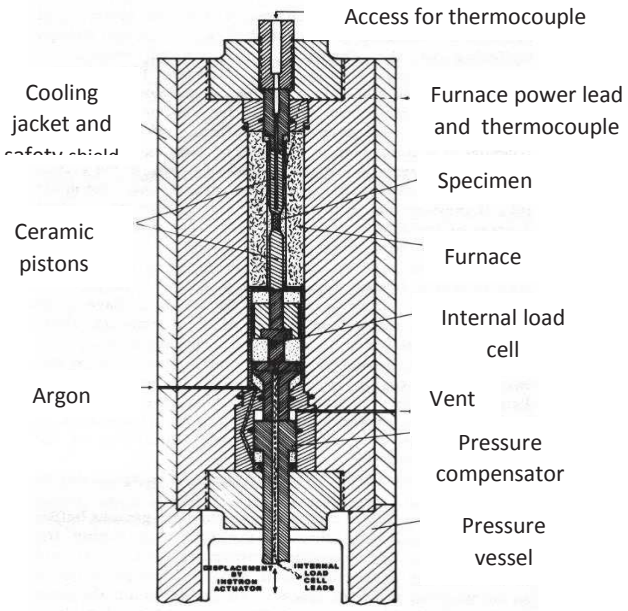

Figure 14 - Modifié d'après Paterson (1990). Schéma de la presse Paterson

La presse Paterson a été conçue par Paterson (1990). Il s'agit d'un autoclave à chauffage interne et sous pression d'argon qui peut atteindre des températures de 1300 °C et des pressions de confinement allant jusqu'à 400 MPa. Un module de déformation axial permet de déformer des échantillons à haute température et haute pression (**Figure** 14).

2.1. Utilisation de la presse Paterson

La presse Paterson peut être utilisée pour effectuer des expériences de déformation d'échantillons à haute température (Thieme *et al.*, 2018), des expériences de diffusion d'éléments chimiques en conditions anhydre (Demouchy, 2010) et hydratée (Demouchy *et al.*, 2007) ou encore des expériences pour mesurer des propriétés physiques comme la conductivité électriques des roches (Violay *et al.*,

2012). La presse Paterson permet également de réaliser des expériences de recristallisation en conditions dynamiques ou statiques (avec ou sans déformation appliquée, respectivement). Ce dernier type d'expérience est celui réalisé pour cette étude, le but étant de recréer des conditions de déshydratation de l'antigorite à haute température (730 °C), moyenne pression (300 MPa) et en drainant les fluides produits par déshydratation.

La presse Paterson est utilisée ici car elle permet de réaliser des expériences dans des conditions de pression identiques à celle de Val Malenco (300 MPa) plutôt qu'un piston-cylindre ou une presse Griggs qui sont plus adaptés pour des expériences de haute pression (>1GPa). De plus, la charge expérimentale permet d'incorporer un plus gros volume d'échantillon et donc plus de matière analysable avant et après les expériences.

2.2. Configuration expérimentale

Deux serpentinites provenant de Val Malenco (Italie) et du massif de Cerro del Almirez (Espagne) ont été choisies pour leurs microstructures, à savoir leur faible et forte foliation, respectivement. Pour évaluer l'impact de l'orientation de la foliation sur les microstructures produites par déshydratation de l'antigorite, des cylindres ont été forés avec trois directions différentes : aléatoirement dans le cas de la serpentinite de Val Malenco, parallèle et perpendiculaire au plan de foliation dans le cas de la serpentinite du massif de Cerro del Almirez. Des disques de référence ont également été coupés à partir de ces cylindres pour permettre la comparaison avec le matériel de départ.

Les cylindres de serpentinites utilisés mesurent 11 mm de long et ont un diamètre de 7.8 mm. Un trou de 1 mm a été foré au centre de ces cylindres pour y insérer un tube d'alumine poreuse (2% de porosité) servant à drainer les fluides produits lors de la déshydratation de l'antigorite et à diminuer la pression fluide du système. Ces assemblages ont été placés dans des capsules télescopiques en nickel longues de 17.76 mm avec un diamètre extérieur de 10 mm et une épaisseur de paroi de 0.35 mm. Deux disques d'alumine poreuse (8.5% de porosité) furent ajoutés à la base et au-dessus des cylindres pour servir de réservoirs aux fluides produits. Une poudre de serpentinite ayant une granulométrie de 100 µm et issue du broyage des serpentinites de départ a été également été ajoutée dans les capsules

pour remplir les vides entre les cylindres et les capsules. Des marques ont été appliquées sur les cylindres de serpentinites et les disques de référence, coupés précédemment, afin de retrouver l'orientation de la foliation de l'antigorite de départ à la fin des expériences. Les capsules en nickel ont ensuite été placées dans des tubes en acier avec des pistons d'alumine et de zircone et des bagues d'espacement de la même manière que dans Demouchy (2010) ou Mei & Kohlstedt (2000).

La température nécessaire à la déshydratation de l'antigorite a été produite par un four composé d'un tube d'alumine autour duquel sont enroulées trois bobines de molybdène composées chacune de 15 enroulements. Ces trois bobines étaient alimentées indépendamment les unes des autres par une interface externe. La température cible choisie dans ces expériences est de 730 °C, la température de déshydratation de l'antigorite à l'équilibre étant de 560 °C à 300 MPa, l'écart de température ΔT (l'écart par rapport à l'équilibre) est donc de 170 °C. Un large écart à l'équilibre permet d'augmenter la vitesse de réaction et d'éviter des réactions trop lentes typiques des conditions naturelles. Le four a été calibré pour des températures de 700 °C et 800 °C. Pour avoir le meilleur profil de température avec le plus petit gradient thermique possible, le thermocouple était déplacé tous les 5 mm pour déterminer la température le long des trois zones chaudes correspondant aux trois bobines de molybdène (**Fig.** 15a). Les assemblages expérimentaux ont ensuite été introduits dans la presse Paterson. A partir de la calibration du four, les échantillons de serpentinites ont pu être placés au niveau du gradient thermique le plus faible du profil de température préétabli (**Fig.** 15b).

L'assemblage a ensuite été pressurisé à température ambiante jusqu'à 110 MPa. Ensuite, la température a été augmentée de 8 °C/min jusqu'à 730 °C. Une fois cette température atteinte, la pression a rapidement été augmentée jusqu'à 300 MPa (**Figure** 16a). L'augmentation de température et de pression a été réalisée de manière à suivre l'isochore de l'eau de 30 cm^3/mol afin d'éviter de trop gros changements de volumes qui pourraient provoquer la rupture de la capsule. La température et la pression ont ensuite été maintenues constantes pendant 10 heures. Aucune déformation axiale ne fut appliquée pendant les expériences, de manière à déshydrater l'antigorite de façon statique. Les assemblages expérimentaux ont ensuite été trempés en diminuant la température de 80 °C/min et la pression de manière à ne pas dépasser l'isochore (**Figure** 16b).

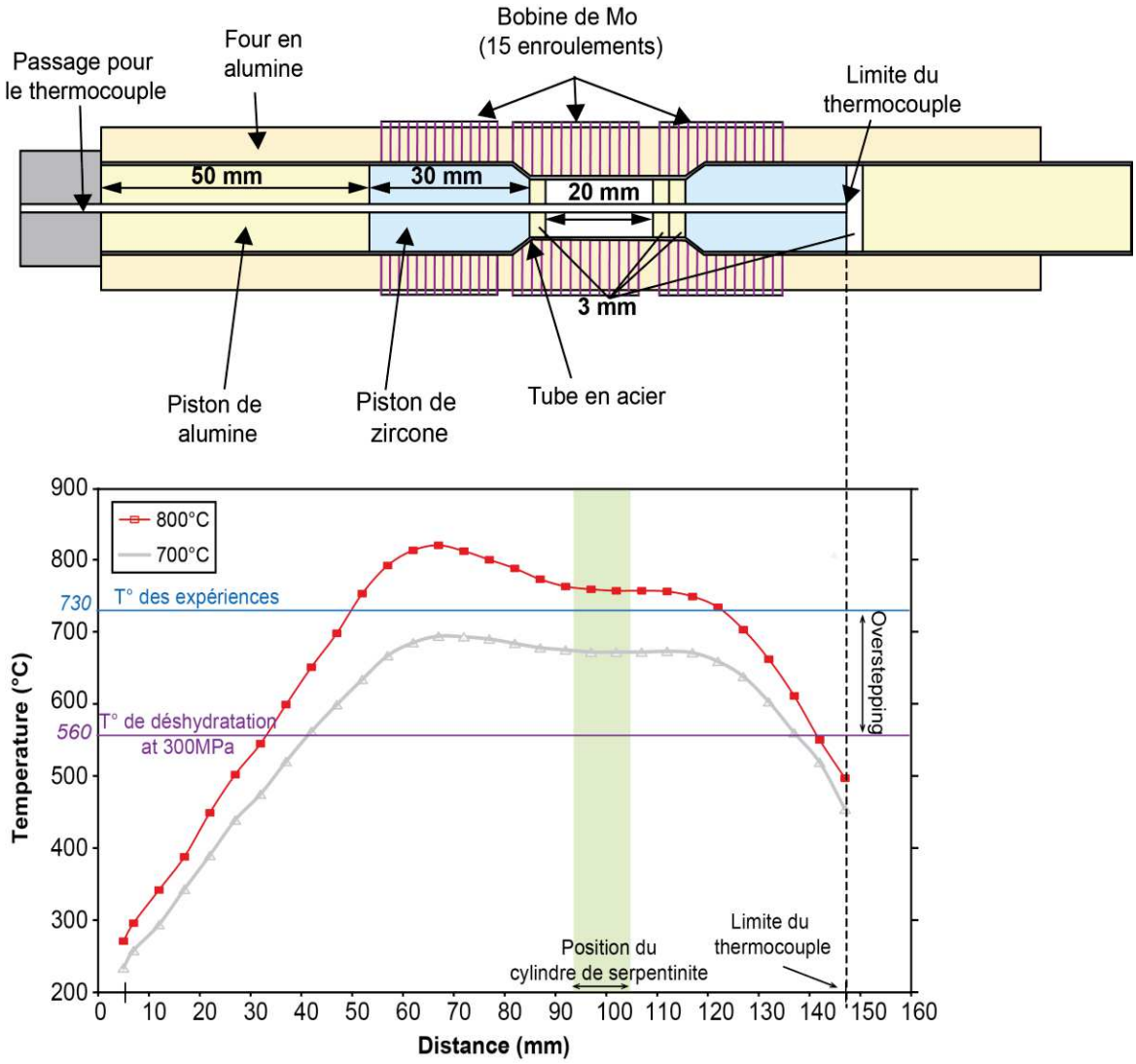

Figure 15 - (a) Schéma du four utilisé pour les expériences et (b) profil de température obtenu à 700°C et 800°C avec l'assemblage de calibration. La position des cylindres de serpentinite utilisés pour les expériences est indiquée en vert

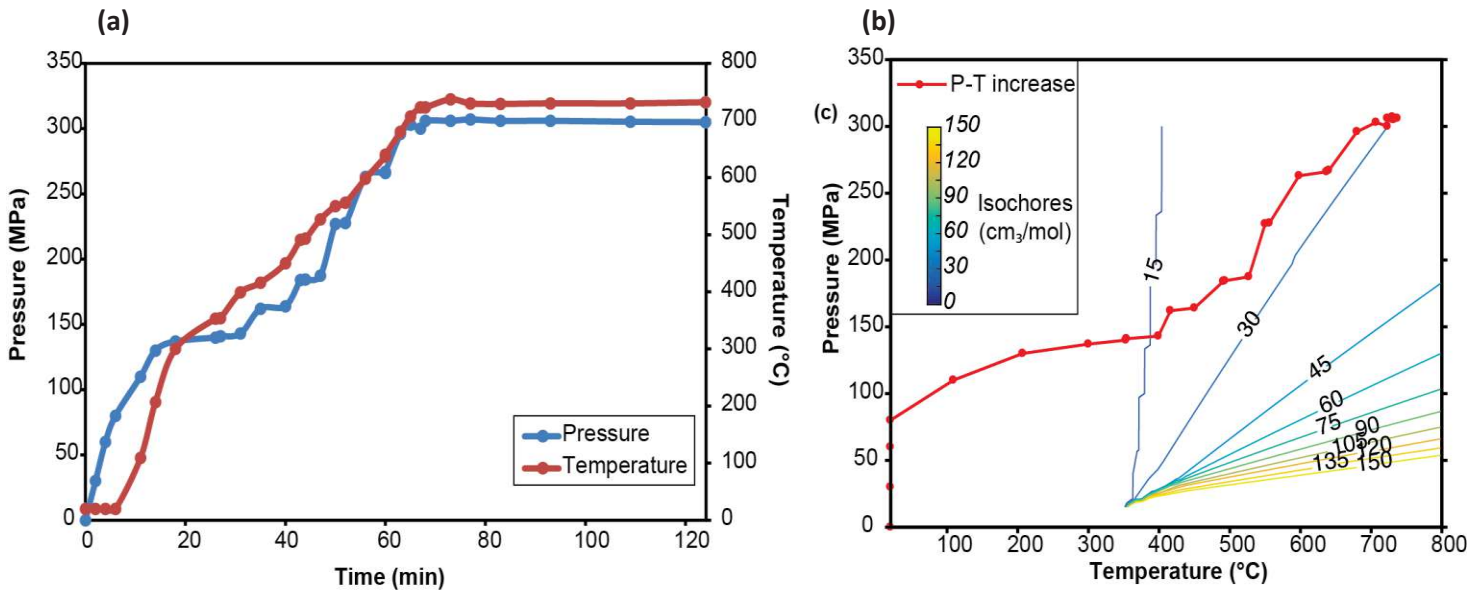

Figure 16 - (a) Chemin de l'augmentation de la pression et de la température (b) isochores de l'eau et chemin P-T suivi

3. TECHNIQUES ANALYTIQUES

3.1. Le microscope électronique à balayage

Le microscope électronique à balayage a essentiellement été utilisé pour étudier les échantillons issus des expériences réalisées avec la presse Paterson. Le principe de la microscopie électronique repose sur un canon à électron bombardant un échantillon avec des électrons issus de l'arrachement d'un fil de tungstène porté à haute température et accélérés le long d'une colonne grâce à une tension d'accélération. Ce bombardement de l'échantillon par des électrons primaires va entrainer l'expulsion de différents électrons de l'échantillon et plus particulièrement deux types : les électrons secondaires et les électrons rétrodiffusés. Le premier type est émis proche de la surface de l'échantillon et réceptionné par un détecteur et donne des informations sur la surface de l'échantillon. Le deuxième type correspond à des électrons émis jusqu'à 0.5 µm de la surface de l'échantillon et renseigne sur la chimie de l'échantillon : les composants chimiques « lourds » comme le fer riches en électrons en renvoient d'avantage que les éléments plus léger comme le sodium, produisant une image plus claire. L'analyse chimique semi-quantitative de l'échantillon par microscopie électronique est possible grâce à un détecteur EDS (Energy Dispersive X-ray Spectroscopy) qui compte le nombre de photons X émis pendant que l'échantillon est bombardé par le faisceau d'électrons durant un temps déterminé (**Fig.** 17).

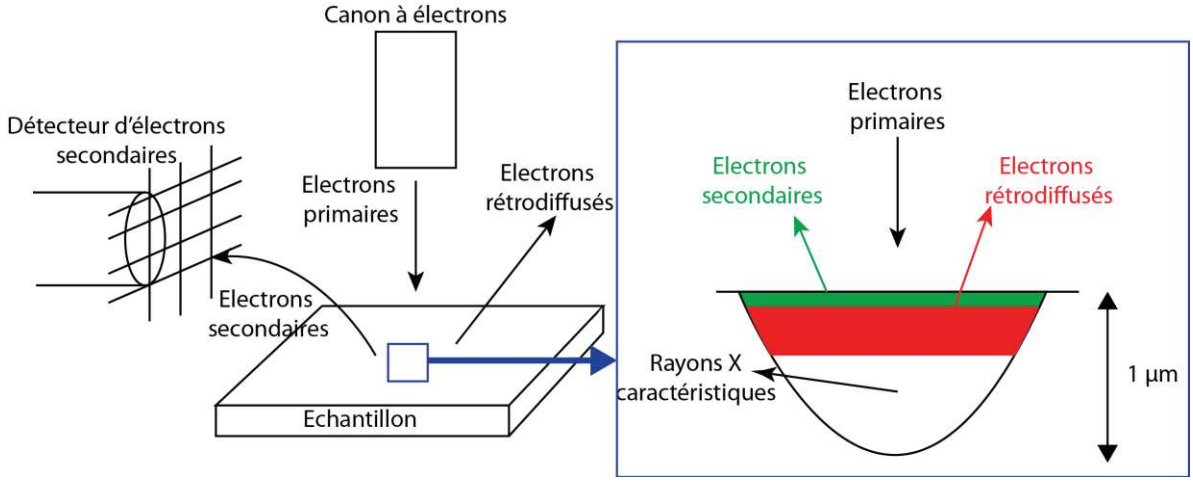

Figure 17 - Schéma du fonctionnement de la microscopie électronique et volume d'interaction des électrons avec l'échantillon

Le microscope à balayage utilisé ici est un microscope à canon à émission de champ (Field Emission GUN) FEI Quanta 200 équipé d'un système de microanalyse X à sélection d'énergie (EDS) avec un détecteur SDD (Oxford Instruments X-Max 50mm2). La tension d'accélération employée était de 10 kV et la résolution des images prises était de 5.5 µm.

3.2. La microsonde électronique

Les analyses par microsonde électronique ont été réalisées sur les minéraux des serpentinites naturelles prélevées à Val Malenco et au massif de Cerro del Almirez (pour la quantification chimique de l'antigorite servant comme matériel de départ aux expériences). Le principe de fonctionnement est sensiblement le même que pour la microscopie électronique, la différence étant que la détection des photons X issus du bombardement par les électrons de l'échantillon se fait grâce à cinq spectromètre à longueur d'onde (WDS, Wavelengh Dispersive Energy). Chaque détecteur comporte un cristal monochromateur de dimension connu et sur lequel les photons X vont être diffractés. L'intensité du signal est fonction de la déviation 2θ du faisceau, θ étant l'angle d'incidence des électrons avec les plans réticulaires. L'énergie fonction de la déviation du faisceau est donnée par la loi de Bragg :

$$2d \sin \theta = n\lambda \quad (3)$$

avec *d* la distance inter-réticulaire du plan cristallin, *λ* la longueur d'onde de la radiation et *n* l'ordre de diffraction qui est un nombre entier. L'énergie correspondante est donnée par la loi de Planck :

$$E = h.v = \frac{h\,c}{\lambda} \quad (4)$$

avec *h* la constante de Planck, *c* la célérité de la vitesse de la lumière et *v* la fréquence. L'analyse est ici quantitative au lieu d'être seulement semi-quantitative grâce à l'utilisation de standard de référence.

La microsonde utilisée pour les analyses des minéraux est une CAMECA SX100, la tension d'accélération employée était de 20 kV, la largeur du faisceau utilisée était de 10 nA et le temps de comptage était de 20-30 secondes. La méthode de quantification employée est celle décrite par (Merlet, 1994), les standards utilisés étant des minéraux et oxydes naturels.

3.3. La diffraction des électrons rétrodiffusés (EBSD)

Les analyses EBSD constituent l'essentiel des analyses effectuées au cours de cette étude. Les échantillons expérimentaux et la moitié des échantillons naturels (61 sur 122) ont été analysés par cette méthode qui permet de déterminer l'orientation des minéraux en trois dimensions à haute résolution et donc de suivre à très petite échelle (nm) l'évolution de la déshydratation de l'antigorite en minéraux prograde.

Cette technique repose sur l'exploitation des clichés de diffraction des électrons rétrodiffusés et permet de relier la structure cristalline aux microstructures des échantillons, contrairement à l'analyse par diffraction des rayons X. Le détecteur EBSD, placé dans un microscope électronique à balayage, est constitué d'un écran fluorescent sur lequel se forment les diagrammes de diffraction. Le faisceau d'électrons percute la surface de l'échantillon provoquant une diffusion inélastique d'une fraction des électrons formant une source divergente d'électrons dans l'échantillon. Une petite partie de ces électrons rétrodiffusés vont diffracter sur les plans cristallins selon un angle θ satisfaisant la loi de Bragg décrite précédemment. La diffraction des électrons sur un plan cristallin s'effectue suivant deux cônes très ouverts, formant ainsi deux lignes qui apparaissent quasiment droite sur l'écran phosphore. Ces deux lignes forment une bande dont la ligne centrale correspond à la projection du plan diffractant sur l'écran (bande de Kikuchi). Le même processus s'opère pour tous les plans, formant ainsi un cliché de diffraction. L'association du détecteur EBSD avec un microscope électronique à balayage permet alors de faire correspondre une image en électrons secondaires ou rétrodiffusés avec son cliché de diffraction (**Fig.** 18).

En déterminant la position de plusieurs bandes de Kikuchi par analyse d'image grâce à une transformée de Hough et en indexant les plans cristallins avec les indices de Miller, il est possible alors de connaître l'orientation d'un point mesuré. Le taux d'indexation des minéraux dépend grandement de la qualité du polissage des lames.

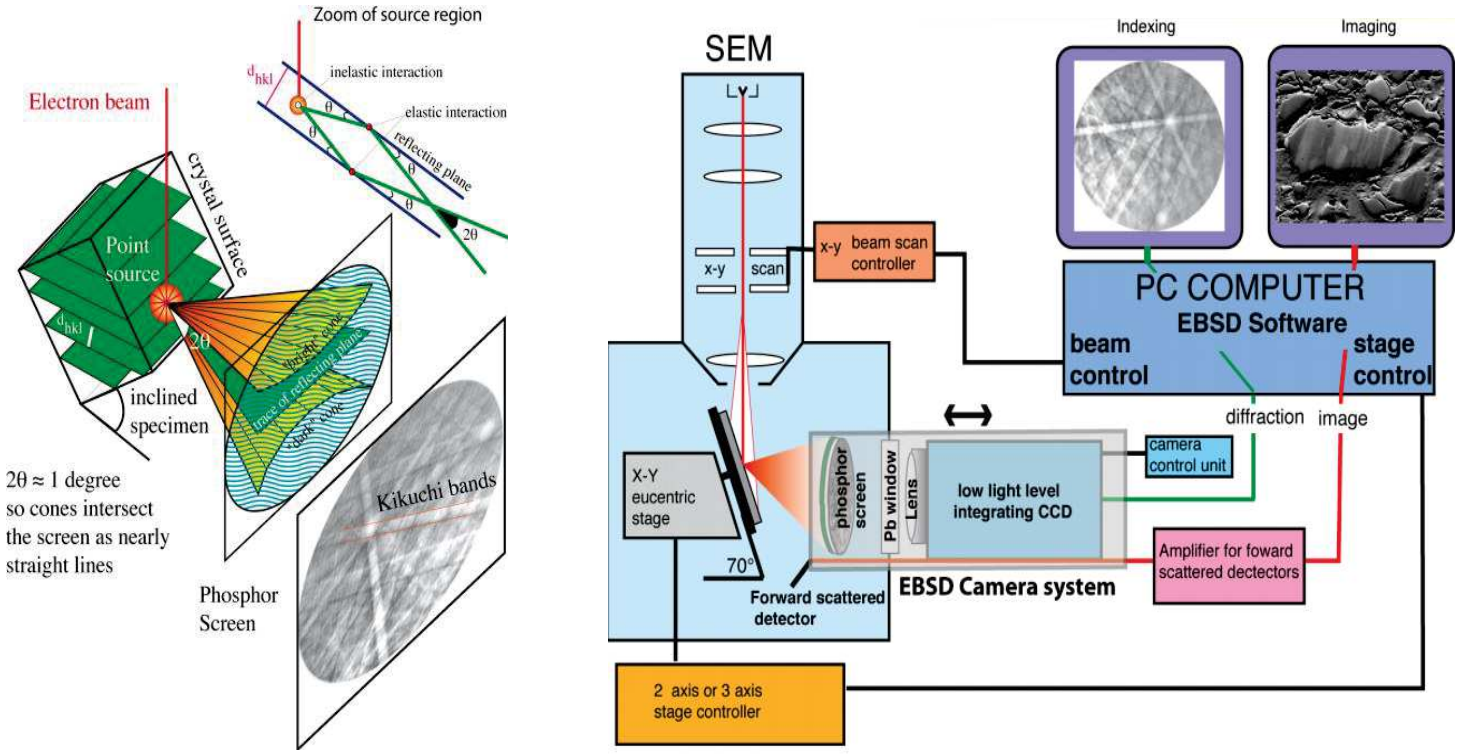

Figure 18 - Schéma du principe de l'analyse par diffraction des éléctrons rétrodiffusés et méthode d'acquisition des données (Mainprice 2012)

Les analyses ont été effectuées avec un microscope électronique à balayage JEOL 5600 équipé avec un détecteur NordlysNano EBSD pour réaliser des cartes d'orientations des minéraux des échantillons de Val Malenco à partir des lames minces avec une résolution de 16 à 27 µm. De plus, le MEB à canon à emission de champ Camscan Crystal Probe X500FE équipé avec un détecteur HKL NordlysNano EBSD a été utilisé pour mesurer l'orientation des minéraux des serpentinites et métapéridotites naturelles avec des cartes de plus hautes résolution (8 µm) et une tension d'accélération de 18 kV. Les échantillons expérimentaux ont également été mesurés avec le Crystal probe mais avec une très forte résolution de 300 nm et une tension d'accélération de 20 kV.

L'orientation des minéraux des serpentinites et métapéridotites est exprimée en angles d'Euler, qui correspondent à une série de trois rotations successives autour d'un axe et permettant de retrouver l'orientation d'un cristal de référence. La convention utilisée pour cette étude est l'utilisation des angles d'Euler définis par Bunge (1993) qui correspondent à une rotation autour de l'axe 0Z (angle φ1), une rotation autour de l'axe 0X' (angle Φ) et une rotation autour de l'axe 0Z' (angle φ2, **Fig.** 19). Le cristal de référence utilisé pendant les analyses EBSD est un cristal de

silicone. Celui-ci se trouve sur le porte échantillon, à côté des échantillons à analyser.

Les données EBSD exprimées en angles d'Euler de Bunge ont ensuite été traitées à l'aide de la boite à outil Matlab© MTEX (Hielscher and Schaeben, 2008; Mainprice *et al.*, 2014) qui permet de reconstruire l'orientation des minéraux à partir des angles d'Euler et d'exploiter ces données pour produire des cartes d'orientation, de désorientation, des figures de pôles, etc.

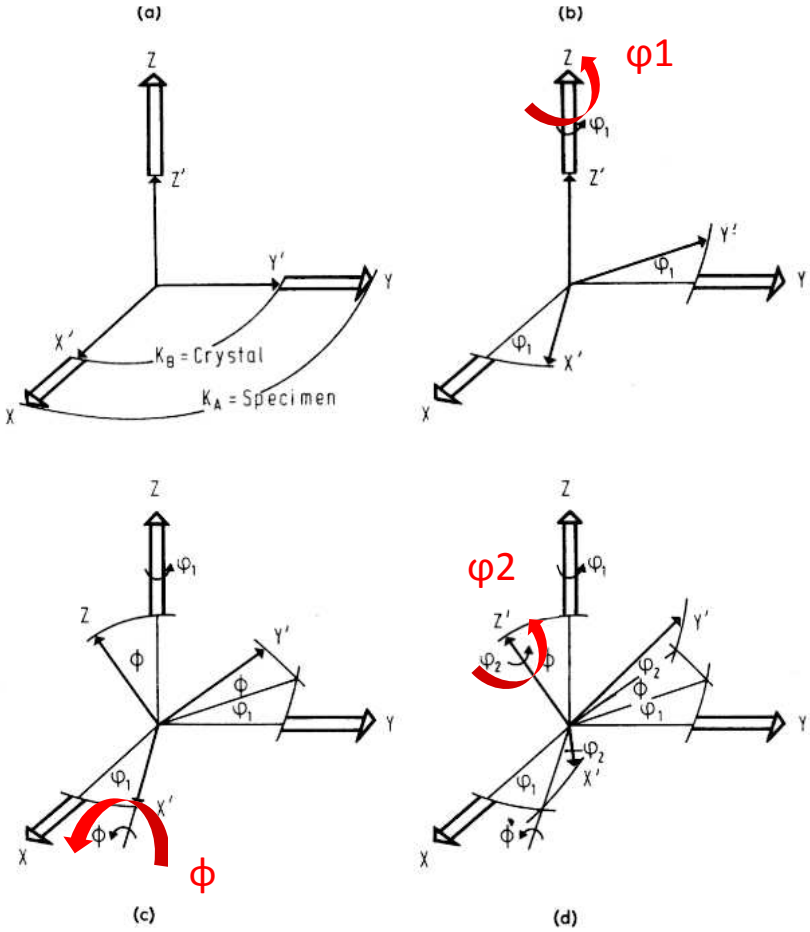

Figure 19 - Représentation schématique des séries de rotation effectuée selon les trois angles d'Euler de Bunge, modifié d'après Bunge (1993)

CHAPITRE III

MIGRATON DE FLUIDES DES SERPENTINITES DÉSHYDRATÉES NATURELLEMENT : EXEMPLE DE VAL MALENCO (ITALIE)

III. MIGRATION DE FLUIDES DES SERPENTINITES DÉSHYDRATÉES NATURELLEMENT : EXEMPLE DE VAL MALENCO (Italie)

1. INTRODUCTION

Dehydration reactions influence rock mechanics, chemical advection (mineralization) and spark the kinetics of mineral transformation both at crust and mantle conditions (Connolly, 2010). In subduction settings, a major dehydration reaction is the breakdown of antigorite due to its relatively large stability field (ca. 680 °C) and the significant amount of water stored in its structure (11-13 wt% of H_2O, Ulmer and Trommsdorff, 1995). The increase of temperature during slab subduction triggers the dehydration of antigorite over a short temperature interval (tens of degrees) in the partially serpentinized mantle. This process releases a large volume of water-rich fluids (Scambelluri *et al.*, 2001; Schmidt and Poli, 2013). These fluids migrate into the overlying mantle wedge, producing serpentinization in the coldest parts of the mantle wedge (Hyndman and Peacock, 2003), and eventually partial melting and arc volcanism (Kelemen *et al.*, 2003). The release of fluids from subducting oceanic lithosphere might also be responsible of the generation of earthquakes (Hacker, 2003; Peacock, 2001), although the details of such process is still a matter of debate (e.g. Chernak and Hirth, 2011; Hirth and Guillot, 2013; Gasc et al. 2011, 2017).

Dehydration reactions produce a net decrease of the total solid volume and consequently an important increase of the fluid-filled porosity. These fluids may flow either pervasively through an interconnected pore network (Etheridge *et al.*, 1983; Etschmann *et al.*, 2014; Putnis and John, 2010) or be focused in structures characterized by a higher permeability than the surrounding, such as fractures created by local fluid overpressure or tectonic processes (Ferry *et al.*, 1998; Flekkøy *et al.*, 2002; Kawano *et al.*, 2011; Nakashima, 1995; Padrón-Navarta *et al.*, 2010a). Even small variations in permeability, such as those associated with lithological contrasts or rock microstructure, may affect fluid flow. Experimental studies on the permeability of strongly foliated serpentinites showed that fluid flow velocity is an order of magnitude higher for flow parallel to the foliation than for flow perpendicular to it (Kawano *et al.*, 2011).

Mechanisms driving fluid flow during dehydration reactions are still poorly understood because of the complex interplay between porosity, permeability, rheology of the solid matrix and the rheology of the fluid-bearing rock that vary during the course of the reaction. Numerical studies from Connolly (1997, 2010) point to a major role of compaction on fluid migration. These models show that during dehydration reactions the rock compacts viscously if the difference between the pore fluid pressure and the lithostatic pressure is lower than the tensile strength of the rock. In case that this difference is higher, devolatilization reactions might induce hydrofracturing, increasing porosity and permeability (see also Okamoto et al. 2017). The coupling between these processes may generate “porosity waves” if the reaction-generated fluid flux is at least three times the flux that can percolate through the undeformed rock (Connolly 1997, 2010). Porosity waves allow for efficient fluid migration. Compaction driving fluid flow may be responsible for a non-hydrostatic stress field at the grain scale. This stress field will might induce deformation in the dehydrating rocks such as the inversion of orthoenstatite to clinoenstatite (Clément *et al.*, 2018; Padrón-Navarta *et al.*, 2015) or modify the crystallographic orientations of olivine inherited from antigorite by interface-coupled dissolution-precipitation processes (Putnis, 2002; Putnis and Putnis, 2007).

Fluid flow may also influence reaction kinetics. A decrease in pore fluid pressure at constant confining pressure leads to an increase in the kinetics of dehydration reactions (Lasaga, 1989; Llana-Fúnez *et al.*, 2012; Miller *et al.*, 2003a; Wang and Wong, 2003), because it increases the affinity of the reaction (Pattison *et al.*, 2011). Depending on the rate of fluid pressure reduction (pervasive flow or focused flow), dehydration reaction kinetics may increase slowly or rapidly. The above cited works used experiments or numerical modeling to evaluate the effects of fluid flow on dehydration reactions kinetics. In addition, Padrón-Navarta *et al.* (2011) proposed that microstructures observed in metaperidotites produced by the dehydration of antigorite at high pressure from Cerro del Almirez (SE Spain) record variations in reaction rates in response to different regimes of fluid extraction: slow fluid migration producing granular microstructures whereas fast draining results in disequilibrium textures (spinifex-like).

The purpose of this work is to investigate the mechanisms of fluid migration at crustal conditions by studying macro- and micro-scale structures in partially to totally dehydrated antigorite-schists from Val Malenco (N Italy) in order to bring constraints on fluid migration in subduction zones (Chapter I.2). Serpentinites from this locality have been dehydrated under quasi-static conditions in response to the intrusion of the Bergell tonalite. They offer therefore a unique opportunity to follow antigorite dehydration reactions and the evolution of the texture of dehydrated serpentinites at the km-scale because the whole structure has been little affected by later deformation.

2. GEOLOGICAL CONTEXT

The Malenco unit is located at the transition between the Austroalpine and Penninic units (**Fig.** 1, Müntener and Hermann, 1996). It comprises a fossil lower crust-upper mantle section mainly composed of gabbro, peridotite, serpentinite, ophicarbonate, as well as metapelite from the lower crust (Hermann *et al.*, 1997). The ultramafic rocks from the Malenco unit are interpreted as part of the Adriatic subcontinental lithosphere exhumed during Jurassic by rifting, when they were exposed at the seafloor of the Piemont Ligurian ocean (Müntener *et al.*, 1999). During exposition at the ocean floor, the ultramafic rocks were serpentinized and ophicarbonates were formed on top of mantle rocks within fractures and as sedimentary platform (Trommsdorff *et al.*, 2000).

The assemblage of ultramafic and mafic rocks and ophicarbonates was moderatly buried in late Cretaceous during regional Alpine metamorphism (peak temperature and pressure estimated at 450°C and 6 kbar; Hermann *et al.*, 1997; Mellini *et al.*, 1987; Trommsdorff and Evans, 1974). The subduction-related metamorphism lead to the transformation of the chrysotile-bearing serpentinized peridotites to antigorite-schists with a mineral assemblage of Atg + Ol + Di + Chl + Mag (abbreviations as in Whitney and Evans, 2010) with Ti-clinohumite, brucite and sulfides as accessory phases (Trommsdorff and Evans, 1974; Trommsdorff and Connolly, 1996; Worden, 1991). Olivine in this assemblage results from the reaction (in the simplified MgO-SiO_2-H_2O system):

$$Mg_{48}Si_{34}O_{85}(OH)_{62} + 20\ Mg(OH)_2 = 34\ Mg_2SiO_4 + 51\ H_2O$$

antigorite brucite forsterite water (1)

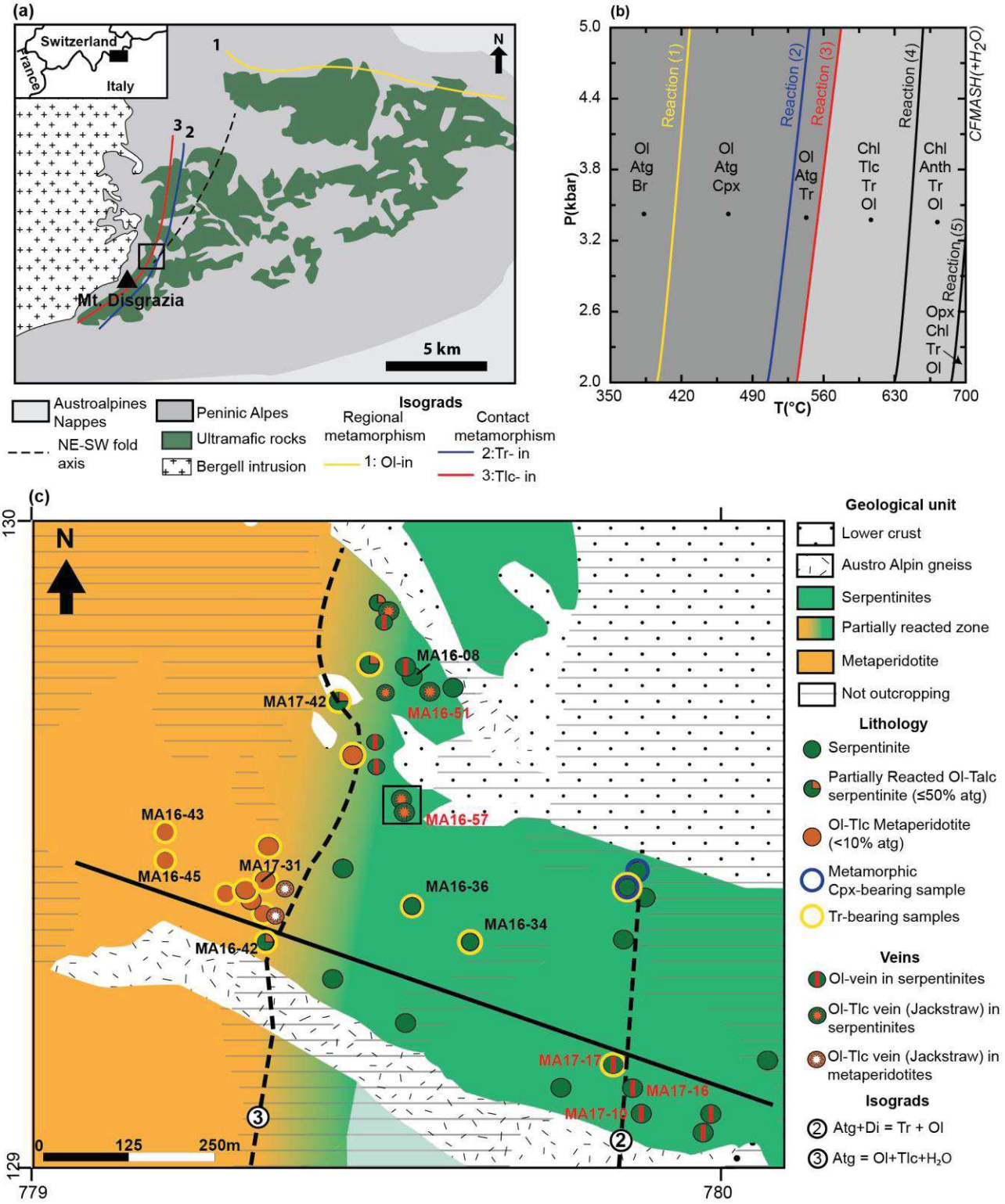

Figure 20 - (a) Geological setting of Val Malenco. Ultramafic rocks refer to either peridotites or serpentinites. Square is the studied area enlarged in Figure 1c. (b) Phase diagram in the CFMASH system in the P-T conditions of formation of rocks from Val Malenco. Yellow line is reaction 1, blue line is reaction 2 and red line is reaction 3 (see text for details). (c) Detailed map of the main lithologies and outcropping samples found in our study. Thick and black line is the profile along which orientations of samples are plotted in Figure 8. Text box in black are samples plotted in Figure 9 and text box in red are sample plotted in Figure 11.

The brucite-out reaction has been mapped in the northernmost part of the ultramafic unit (**Fig.** 20a; Mellini *et al.*, 1987; Trommsdorff, 1983). The entire Malenco unit was therefore in greenschists facies conditions, where olivine and antigorite coexist in equilibrium, before the Bergell intrusion (**Fig.** 20a).

A later stage of high-grade contact metamorphism triggered by the composite Bergell intrusion overprinted the regional metamorphism at 32 Ma (Von Blanckenburg *et al.*, 1992), producing a contact aureole onto the ultramafic rocks of Val Malenco. This intrusion occurred after the main episode of Alpine thrusting and folding (Trommsdorff and Evans, 1977; Reber, 1995). A km-scale NNE-SSW trending open fold can be mapped close tonalite intrusion (Trommsdorff *et al.*, 2005; Trommsdorff and Connolly, 1996) although its timing relative the dehydration reaction can not be unambiguously identified (see below). The southern part of Val Malenco, outside the studied area, is deformed by the Insubric Line (**Fig.** 20). Trommsdorff and Evans (1972) have mapped four isograds corresponding to the following reactions in the CMSH system associated the contact metamorphism (**Fig.** 20a):

$$Mg_{48}Si_{34}O_{85}(OH)_{62} + 2\,(Ca,Mg)Si_2O_6 = 2\,Ca_2Mg_5Si_8O_{22}(OH)_2 + 21\,Mg_2SiO_4 + 28\,H_2O \quad (2)$$

Antigorite Diopside Tremolite Olivine Water

$$5\,Mg_{48}Si_{34}O_{85}(OH)_{62} = 18\,Mg_2SiO_4 + 4\,Mg_3Si_4O_{10}(OH)_2 + 27\,H_2O \quad (3)$$

Antigorite Olivine Talc Water

$$2\,Mg_3Si_4O_{10}(OH)_2 + Mg_2SiO_4 = Mg_7Si_8O_{22}(OH)_2 + H_2O \quad (4)$$

Talc Olivine Anthophyllite Water

$$Mg_7Si_8O_{22}(OH)_2 + Mg_2SiO_4 = 9/2\,Mg_2SiO_6 + H_2O \quad (5)$$

Anthophyllite Olivine Enstatite Water

These authors have proposed that the contact between ultramafic and intrusive rocks is roughly vertical, with isograds parallel to the intrusion (**Fig.** 20a). Trommsdorff and Connolly (1990) estimated a pressure of 3.5 kbar in the Bergell contact aureole based on precise thermobarometric constrains based on ophicarbonates.

Samples with anthophyllite and enstatite from reactions (4) and (5) respectively were not investigated in the present study (**Fig.** 20c). In CaO-free systems, associated to refractory domains of the preexisting mantle, reaction (2) does not apply; these domains are therefore characterized by serpentinites with the assemblage of Atg + Ol + Chl + Mag (**Fig.** 20b). **Figure** 20b shows a phase diagram (pseudosection) with increasing temperature and pressure for the CFMASH system for a bulk composition representative of the ultramafic rocks in the contact aureole. Chlorite is also produced by the dehydration of Al-bearing antigorite (Tschermak's substitution $Mg_{-1}Si_{-1}Al_1Al_1$; Padrón-Navarta *et al.*, 2013).

3. ANALYTICAL METHODS

Detailed sampling and structural mapping of ca. 1 km x 1 km area was undertaken in the northeastern part of the contact aureole of the Bergell intrusion (Alpe Zocca) in order to investigate the progressive textural evolution of antigorite schists to olivine-talc (Ol-Tlc) rocks (here referred as metaperidotites)–through the reactions (2) and (3) that involve serpentinites with Atg + Ol + Di + Chl + Mag and Atg + Ol + Tr + Chl + Mag and metaperidotites with Ol + Tlc + Tr + Chl + Mag. Foliation planes (and when possible lineation) of serpentinites and metaperidotites were measured to follow a possible continuity of foliation between these two types of rocks. Orientations of veins were also measured.

Petrographic analyses were carried out by optical microscopy in order to carefully investigate microstructural relationships between antigorite and the products. For geographical oriented samples, thin sections were prepared from vertical sections with E-W orientation looking from the South (i.e. South direction out of thin section surface and long axis of the thin section parallel to the EW direction). This orientation was chosen because of the East dip direction of foliation that predominates in the area (cf. section *4.1.3).* Non-oriented samples were prepared normal to the foliation plane when visible and occasionally parallel to the foliation

plane. All thin sections were polished with diamond paste, followed by colloidal silica for 4 hours and a last stage of polishing with colloidal silica in a vibrometer for 4 hours. Crystal preferred orientations of antigorite, olivine, tremolite, as well as diopside and magnetite, when present, were measured by electron-backscattered diffraction (EBSD) at Géosciences Montpellier (France). A JEOL 5600 scanning electron microscope equipped with a NordlysNano EBSD detector was used to map the orientation of all major rock-forming phases with a resolution of 16-27 μm over the whole thin section. A Camscan Crystal Probe XF500 with a HKL NordlysNano EBSD detector was used to measure orientations of antigorite and olivine over smaller areas with a higher resolution (8 μm). Binning mode was set to 4x4 and accelerating voltage to 17 kV. To enhance antigorite indexation rates, we used two crystal models for indexation (polysome m=16 and m=17, Capitani and Mellini, 2006, 2004) and merged the two orientation datasets for data treatment. EBSD indexation of talc was unsuccessful due to its contrasting polishing properties when compare to the other silicates.

Orientation data were expressed as Bunge Euler angles and processed with the MATLAB toolbox MTEX (Bachmann *et al.*, 2010; Hielscher and Schaeben, 2008; Mainprice *et al.*, 2014). Grain detection was performed with a misorientation threshold of 10°. Grains composed by <3 pixels were removed from dataset. Orientation distribution functions for all phases were calculated using a “de la Vallée poussin” kernel with a constant halfwidth of 10°. Pole figures of antigorite and olivine were plotted in the lower hemisphere using the grain average orientation and a constant colorbar (0-4 multiples of a uniform distribution, m.u.d.) for easy comparison between different samples. The intensity of the crystal preferred orientation (CPO) is characterized by the J-index (Bunge, 1993). The symmetry of the olivine CPO is characterized in terms of symmetry of the orientation distribution of the [010] and [001] axes by the BC-index. This index is calculated similarly to BA-index (Mainprice *et al.*, 2014) according to the following formula:

$$\text{BC index} = \frac{1}{2}\left(2 - \left(\frac{P_{010}}{P_{010}+G_{010}}\right) - \left(\frac{G_{001}}{G_{001}+P_{001}}\right)\right) \qquad (6)$$

where P and G refers to Point and Girdle indexes of (Vollmer, 1990). If the [010] axes of olivine define a point concentration and [100] and [001] form girdles, the BC-

index value is 0. If the [001] axes of olivine defines a point concentration and the [100] and [010] axes form girdles, the BC-index value is 1. CPOs with orthorhombic symmetry are characterized by BC-index values of 0.5.

For chemical analyses, blocks of ~500 g were cut from representative samples avoiding all altered parts. The samples were then crushed into an agate mortar to a ~80 µm grain-size powder. Approximately 50 g were used for analyses. Whole-rock major and minor element analysis was performed at Bureau Veritas Mineral laboratory testing, Vancouver (Canada) using lithium borate fusion coupled to ICP-ES. Additional analyses were conducted on selected samples in order to quantify FeO content (and Fe_2O_3 by difference) by the titration technique. Major and minor element compositions of minerals of selected samples were quantified in carbon coated thin sections by EPMA on a CAMECA SX100 equipped with five wavelength-dispersive X-ray spectrometers (WDS) at Géosciences Montpellier (France). The analyses were performed with 20 kV accelerating voltage, a focused beam of 10 nA and counting times at peak position of 20-30 s. Concentrations are obtained from raw intensities using the ‘‘X-PHI’’ quantification procedure (Merlet, 1994). Natural minerals and synthetic oxides were used as standards.

4. RESULTS

4.1. Field observation

4.1.1. Serpentinites and metaperidotites

The studied area is located at the east contact of the Bergell intrusion, in the western flank of a large open trending NE-SW that affects the Malenco Unit. This area encompasses the contact metamorphism isograds of reaction (2) and (3), which outcrop at ca. 1230 m and at ca. 770 m from the intrusion, respectively. From east to west, serpentinites evolves to metaperidotites.

The serpentinite from the Malenco unit is a greenish schistose fine-grained rock composed of antigorite with variable amounts of olivine, diopside, tremolite, magnetite and chlorite (Trommsdorff and Evans 1972). Schistosity varies locally with more massive serpentinite where foliation is poorly defined. Locally magnetite forms elongated aggregates marking a lineation within in the foliation plane. Metamorphic olivine appear as red-orange (on altered surface) or black mm to cm scale crystals

with rounded or prismatic shapes. In addition to olivine, serpentinites may contain diopside or tremolite, indicating a more fertile (lherzolitic) protolith. Spatial distribution of Ca-poor and Ca-rich serpentinites does not show any regular arrangement. Serpentinites with relict mantle clinopyroxene, which occur as dark-green mm-scale crystals (referred as 'dusty' diallage or clinopyroxene in previous works, Trommsdorff and Evans, 1972), are restricted to the east flank of the fold, outside the study area (Lago Pirola area). In the study area, serpentinites may contain metamorphic diopside which typically occurs as white mm-scale crystals. At closer distances to the intrusion, tremolite replace the metamorphic diopside and occurs as white acicular mm-scale crystals (**Fig.** 21a).

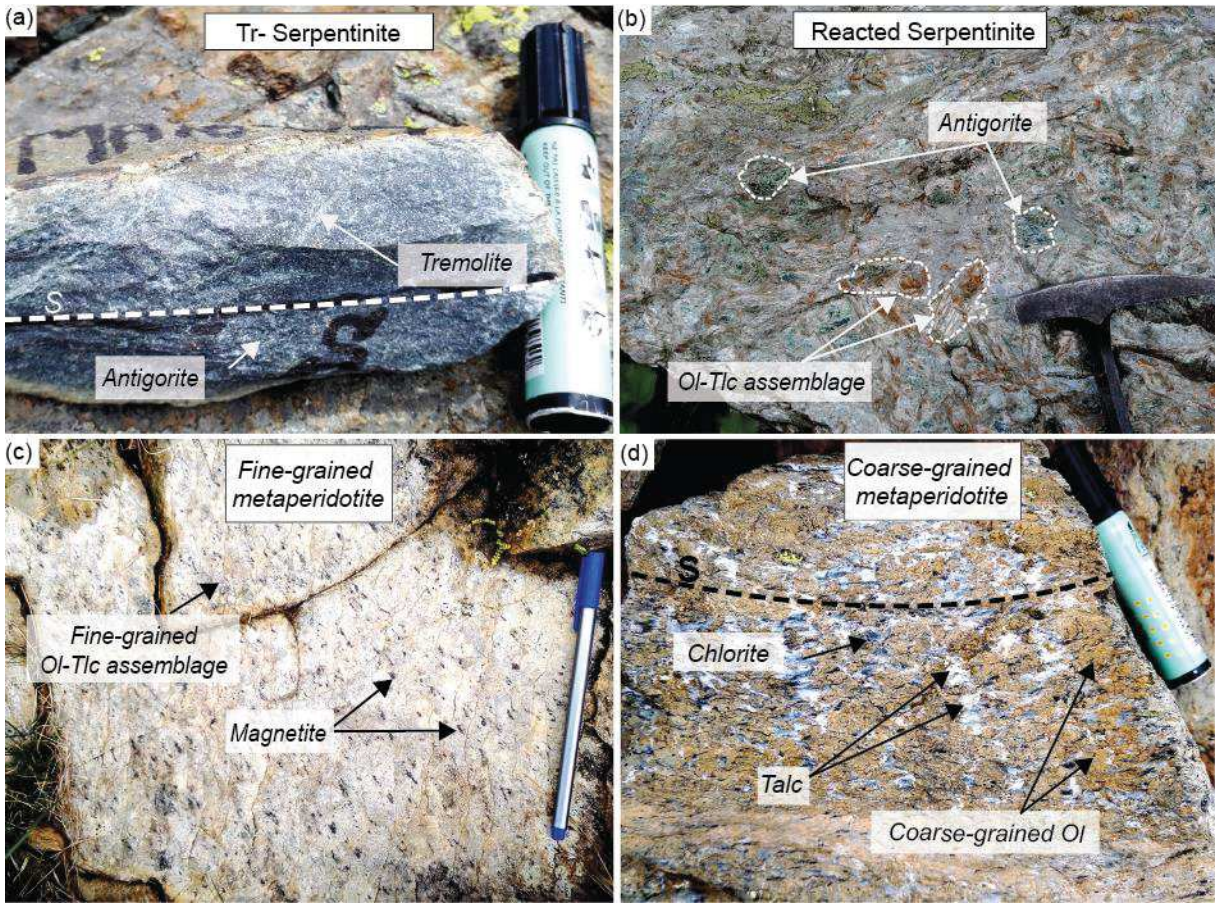

Figure 21 - Representative samples from Val Malenco. (a) Tr-bearing serpentinite with a marked foliation plane. (b) Partially reacted serpentinite with flakes of Ol-Tlc assemblage and antigorite patches. Proportion of each other is approximately 50%-50%. (c) Fine-grained Ol-Tlc metaperidotite with lineation of magnetites. (d) Coarse-grained Ol-Tlc metaperidotite with chlorite between olivine grains.

In the study area, serpentinites are restricted to a maximum distance of ca. 675 m from the intrusion, below which they are progressively transformed to Ol-Tlc(±Tr)

metaperidotite (Reaction (3); Figs. 1b,c). Ol-Tlc(±Tr) rocks are less schistose and more massive than antigorite schists, but a weak foliation can still be recognized in the field. The transition between serpentinites and metaperidotite is smooth. It covers a ~150 m wide area in the western part of the studied area, which is composed of partially dehydrated rocks containing talc-olivine patches or irregularly-shaped domains within an antigorite-rich matrix or vice-versa (**Fig.** 21b). The proportion of the Ol-Tlc assemblage is usually equal or greater than 50 vol% of the rock. Olivine occurs as red-orange (on altered surface) or black mm to cm scale crystals with prismatic or rounded shapes; talc appears as white flakes (**Fig.** 21b).

We define metaperidotite as a rock with more than 90% of products of dehydration reactions. Metaperidotite appears as dark-grey roughly foliated rocks in fresh surfaces, but they have reddish to whitish tones on altered surfaces (**Fig.** 21c,d). Fine-grained metaperidotites (with submillimetric olivine) predominate; these rocks may display a lineation marked by elongated magnetite aggregates (**Fig.** 21c). Locally, metaperidotites are coarse-grained with cm-scale olivine crystals associated with white talc flakes and chlorite that appears as dark-grey crystals (**Fig.** 21d). Coarse-grained metaperidotites are also foliated. No clear spatial arrangement between fine-grained and coarse-grained metaperidotite as a function of the distance from the Bergell intrusion was observed.

4.1.2. Metamorphic veins

A striking feature of the studied area (Alpe Zocca) is the occurrence of metamorphic veins with variable size and shape. Three types of veins have been identified: Ol-veins, Ol-Tr veins, and Ol-Tlc veins (Table 1). They were first reported by Trommsdorff and Connolly (1996).

The most distant veins from the intrusion are Ol-veins (**Fig.** 20c, 22a). These veins contain only olivine, most often as centimetric crystals though smaller mm size crystals also occur. These veins are tens of cm to a few meters long and cm-to-dm wide. At the outcrop scale, multiple subparallel or interconnected veins with a spacing of tens of cm are observed (**Fig.** 22a). Locally conjugate pairs of veins were observed. They have sharp limits at the outcrop scale and crosscut the foliation of the

serpentinites (**Fig.** 22a). Some veins display growth of tabular olivine crystals at their borders, into the serpentinite; these olivine crystals are oriented perpendicular to the vein trend (**Fig.** 22b). Ol-veins are mainly observed just below both the tremolite isograd (Reaction 2) and the talc isograd (Reaction 3) (**Fig.** 20c).

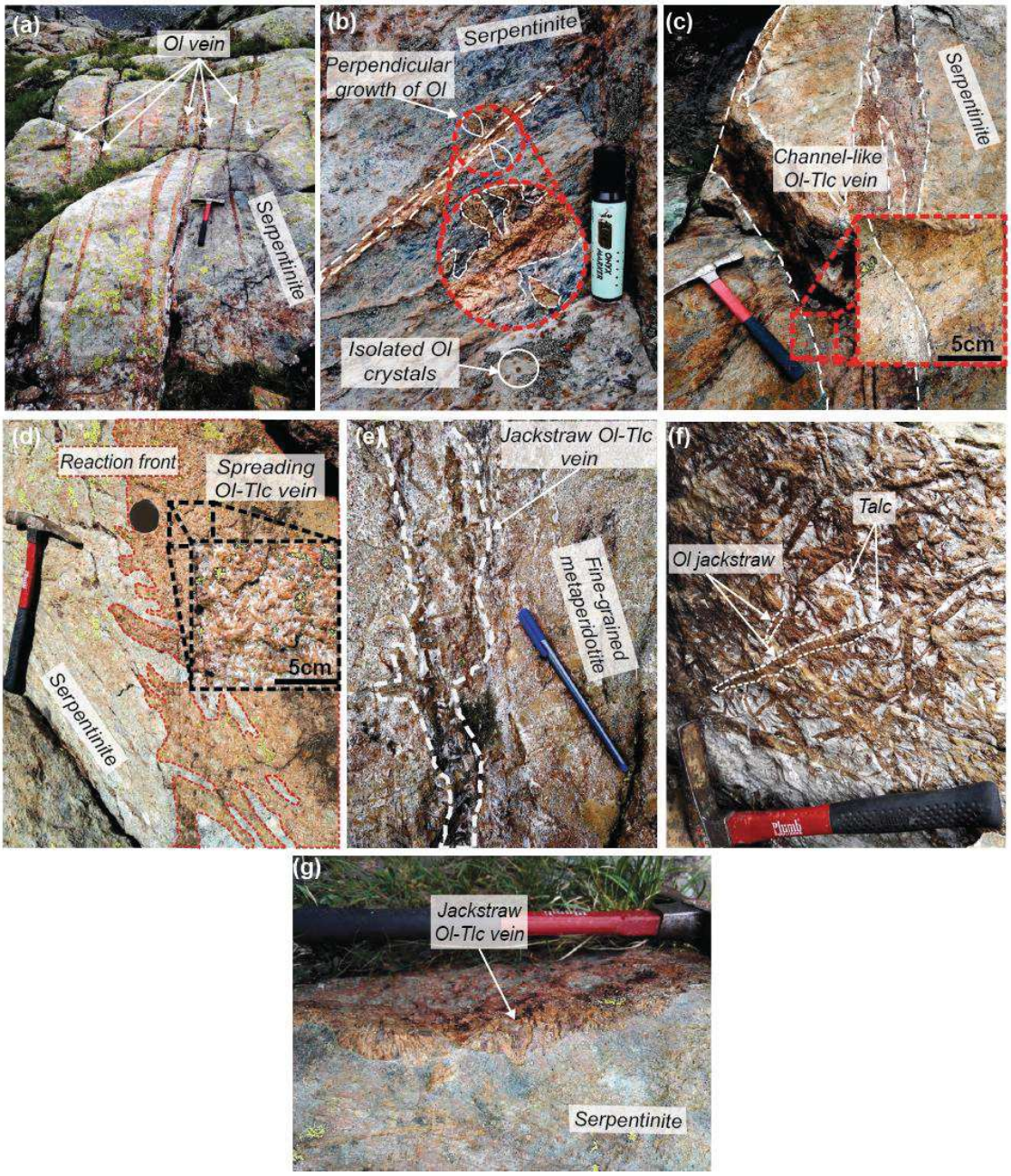

Figure 22 - Examples of representative veins crosscutting the foliation plane of serpentinites. (a) Sharp and thin (cm width) Ol-vein with variable size of olivine grains (µm-to-cm scale). (b) Ol-vein crosscutting foliation plane of serpentinite matrix with isolated Ol grains and with Ol growing perpendicular to the orientation of the vein. (c) Channel-like Ol-Tlc vein (dm width) with sharp contours (enlarged picture) and fine-grained Ol-Tlc assemblage. (d) Ol-Tlc veins with irregular reaction front and elongated and platy olivines (enlarged part). (e) Vein with Jackstraw Ol-Tlc texture in a fine-grained metaperidotite. (f) Jackstraw Ol-Tlc vein with dm-long olivines. (g) Jackstraw Ol-Tlc vein crosccuting serpentinite

Ol-Tr veins are rare. They are only observed in serpentinites close to the tremolite isograd (**Fig.** 20c). Crystals of tremolite in these veins appear as white flakes, but are poorly visible at the outcrop scale because of the large size (cm) of olivine crystals. These veins display the same characteristics than the Ol-veins.

Ol-Tlc veins occur in the partially reacted serpentinites (**Fig.** 20c). Ol-Tlc veins appear dominantly reddish because of the olivine crystals but also have white patches between olivine grains corresponding to talc flakes. Ol-Tlc veins are tens of cm wide and may be several meters long. They have a wide range of morphologies. They may either have irregular, channel-like branching shapes (**Fig.** 22c,e), form isolated, rather planar structures. Some Ol-Tlc veins show irregular finger-shape limits (**Fig.** 22d), or occur as multiple subparallel veins spaced by ~2 m over a distance of ~20 m. In most cases, the veins crosscut the foliation of the serpentinite although occasionally they are contained in the foliation plane. In the metaperidotites some structures might be interpreted as former veins based on the difference of olivine grain size and texture when compared to the host metaperidotite (**Fig.** 22e).

The morphology of olivine crystals changes from one vein to another. Most veins are composed by coarse (> cm) platy olivine crystals oriented parallel in the plane of the vein (**Fig.** 22d), but some contain small olivine crystals (**Fig.** 22c). Ol-Tlc veins often show a jackstraw olivine texture within the plane of the vein (**Fig.** 22d,e,f,g). This texture has already been described in previous studies on Ol-Tlc metaperidotites from Preston Peak area (California, Snoke and Calk, 1978) and in Norwegian Ol-Tlc metaperidotites (Bakke and Korneliussen, 1986). It is characterized by blade-like olivine arranged in crisscross, radial, or parallel patterns (**Fig.** 3f). The coarsest Ol grains in the study area (dm-long, **Fig.** 22f) were observed within jackstraw Ol-Tlc veins.

Figures 23 illustrates the variation in microstructures, olivine crystal preferred orientations, and chemical composition along a section normal to the trend of a channel-like Ol-Tlc vein displayed in **Fig.** 22c. This veins has a diffuse, fingered contact with the serpentinite. The core of the vein is composed by coarse grained Ol and Tlc, with no antigorite (i.e. with a jackstraw texture). The vein grades into a partially-reacted metaperidotite composed by olivine aggregated with tabular shape oriented parallel to the foliation plane defined by the antigorite, which is highly

oblique to the vein trend (**Fig.** 23a). The foliation plane rotates by ~20° from the edge to the center of the vein. The limit between the partially reacted serpentinite and the serpentinite shows a mm-scale fingering. EBSD analyses in the serpentinite, in the partially reacted metaperidotite, show strong crystal preferred orientation (CPO) of both antigorite and olivine, with a similar orientation of the [001] axes of antigorite and [010] axes of olivine normal to the foliation. The low number of olivine grains analyzed in the jackstraw domain does not allow identify a clear CPO. Olivines in the partially-reacted domain show undulose extinction. Rotation axes accommodating this intracrystalline misorientation are <u0w> crystal axes, with some predominance of [100] (**Fig.** 23b).

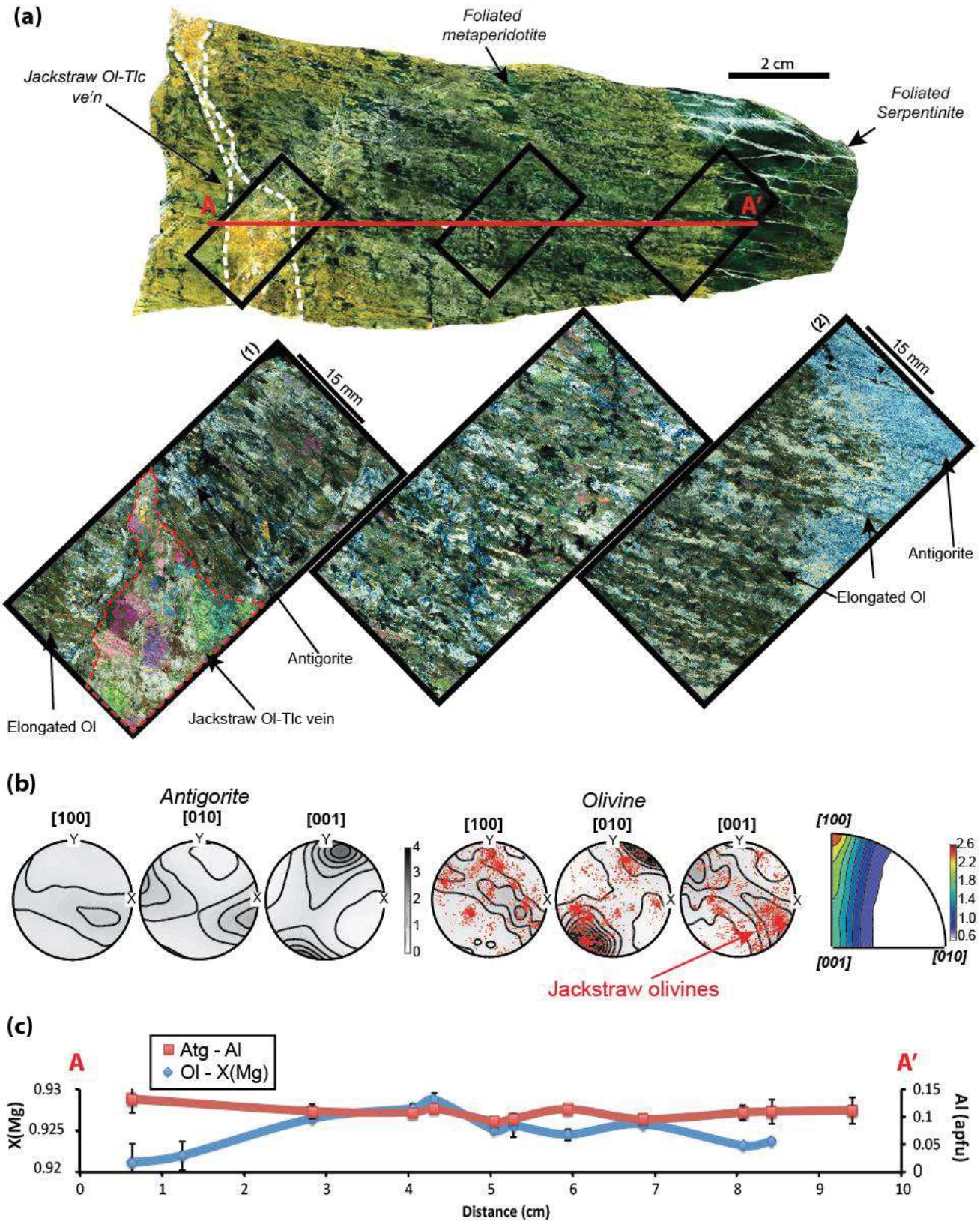

Figure 23 - (a) Part of a channel-like vein from the core to the edge. Reaction front is irregular at the edge and display olivines elongated in the foliation plane defined by antigorite. Jackstraw Ol-Tlc vein is present in the core of the channel-like vein and crosscut the foliation of olivine and antigorite, which appear to be deformed at the vicinity of the central vein. (b) EBSD pole figures showing strong crystal preferred orientation of the foliated antigorite and olivine and random orientations of Jackstraw olivine crystals. Inverse pole figure show that rotation axes are dominantly [100] axes in olivines. (c) Chemical profile of X_{Mg} in olivine and Al_{Atg} (apfu) from the Jackstraw Ol-Tlc vein to the serpentinite part. X_{Mg} of olivine is slightly lower in the Jacktraw crystals but Al content of antigorite in higher in reacted part of the vein.

4.1.3. Foliation, lineation and vein orientations

The strike of the serpentinite foliation close to the Ol-Tr isograd rotates from a NW orientation steeply dipping (~80°) towards the NE to a more NS orientation and less steep dipping towards the contact with the metaperidotites (**Fig.** 24). Locally, foliations with opposite dip directions are observed; they are associated with mesoscale open folds or crenulations. The orientation of the foliation plane in the serpentinites is similar to one of the two groups of orientations determined by Hermann and Muntener (1996), who studied a larger area comprising the two limbs of the late open fold that affects the Malenco serpentinites. The strike of the metaperidotites foliation is remarkably similar to the one of serpentinites close to the Ol-Tlc isograd. Lineations marked by magnetite aggregates elongation in serpentinites have roughly a NS orientation and variable plunge, similarly to those measured by Hermann and Müntener (1996). However in the metaperidotite, magnetite lineations have steeper plunges (**Fig.** 24). All veins are dominantly oriented N60-70° with a subvertical dip crosscutting the serpentinite foliation.

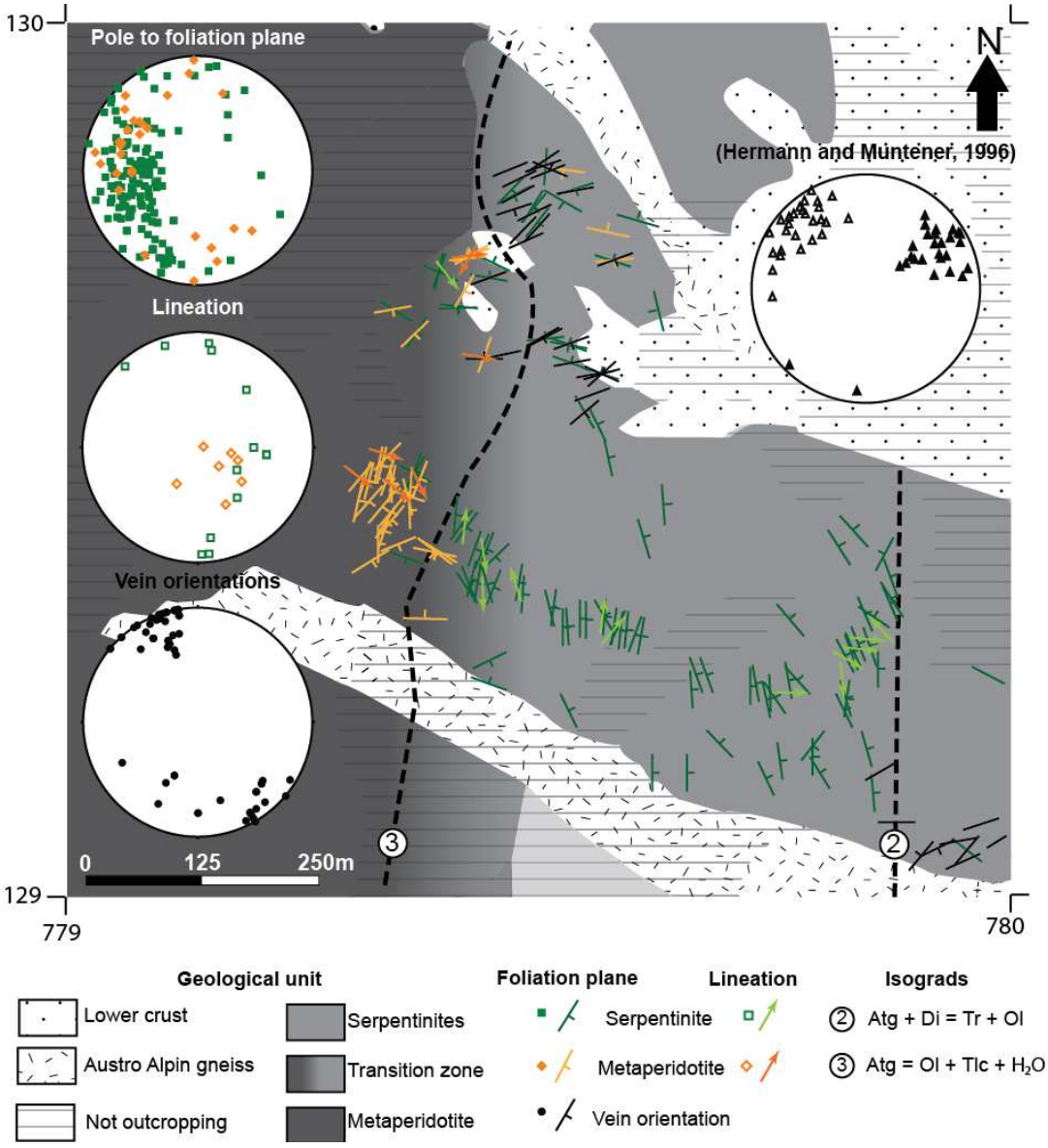

Figure 24 - Foliation plane and lineation orientations in the studied area. Foliation planes of serpentinites are oriented ~N330°/70-80°E close to isograd (2) and changes progressively to N30°/70-80°E closer to isograd (3) and the Bergell intrusion. Foliation plane orientations of metaperidotites are roughly oriented as nearby serpentinites with ~N0-30°/70-80°E. Veins are clustered at N70°/90, i.e. at high angle of the Bergell intrusion. Lineations measured in serpentinites are dispersed whereas lineations measured in metaperidotites are subvertical. Structural measurements of foliation and lineation of ultramafic rocks from (Hermann and Muntener, 1996) in the Eastern part of Val Malenco show opposite dip direction but roughly the same strike than in the Eastern part

4.2. Petrography

4.2.1. Serpentinites and metaperidotites

Ca-poor serpentinites are mainly composed by antigorite crystals with a few isolated olivine porphyroblast with irregular, but sometimes elongated, shapes (up to 2 cm long) in matrix mainly composed by fine-grained antigorite (Fig. 25a). The elongation of antigorite and locally the elongation of porphyroblastic olivines marks

the foliation. Two populations of antigorite crystals were observed with crystals of ~20 µm long and another with higher length of ~500 µm (**Fig.** 25b). Magnetite crystals are mm-size and may form elongated aggregates marking a lineation.

Ca-rich serpentinites are also foliated (cf. **Figure** 21a). At the microscopic scale the foliation is mainly marked by acicular crystals of tremolite, which are ~200 µm long and preferentially elongated parallel to the foliation plane. Antigorite has a variable crystals size (<20 µm to >200 µm). Small aggregate of few mm-size magnetite crystals are aligned in the foliation plane, defining lineation (**Fig.** 25c). Olivine in these serpentinites occurs as porphyroblastic crystals of either <10 µm size with granular shape forming elongated aggregate in the antigorite matrix or as larger porphyroblastic (> 200 µm long) crystals with irregular shapes (**Fig.** 25d). Locally, crystals of olivine in textural equilibrium with tremolite are observed (**Fig.** 25d), indicating that they result from reaction (2).

Partially reacted serpentinites are composed by variable amounts of antigorite and olivine + talc in diffuse patches. They are characterized by aggregates of coarse olivine crystals (~400 µm long), with both the individual crystals and the aggregates elongated on the foliation plane defined by the antigorite shape preferred orientation (**Fig.** 25e,f). In these samples, talc either occurs associated with olivine (**Fig.** 25f) or as diffuse layers parallel to the foliation in the antigorite matrix. Olivine crystals have not fully developed crystallographic faces, but elongated shapes with serrated overgrowths (**Fig.** 25f). Partially reacted Ol-Tlc-Tr serpentinite may also show assemblages of granular olivine of ~200 µm in size, tremolite with similar size but in a minor amount, and talc crystals, enclosing antigorite-rich lenses of variable sizes (from a few mm to a few cm long, **Fig.** 25g). The antigorite-rich lenses contain prismatic olivine crystals, flattened parallel to the antigorite foliation (**Fig.** 25h). These olivine crystals form an anastomozed network that follows the antigorite foliation (**Fig.** 25h). The antigorite-rich and Ol-Tlc-Tr-rich domains are interspersed and show smooth transitions (**Fig.** 25h)

Metaperidotites have highly variable textures: olivine crystals may have different shapes and sizes with a variable proportion of talc. Metaperidotites are composed by small polygonal to rounded olivine crystals (~20 µm) in a fine-grained assemblage with talc (**Fig.** 26a).

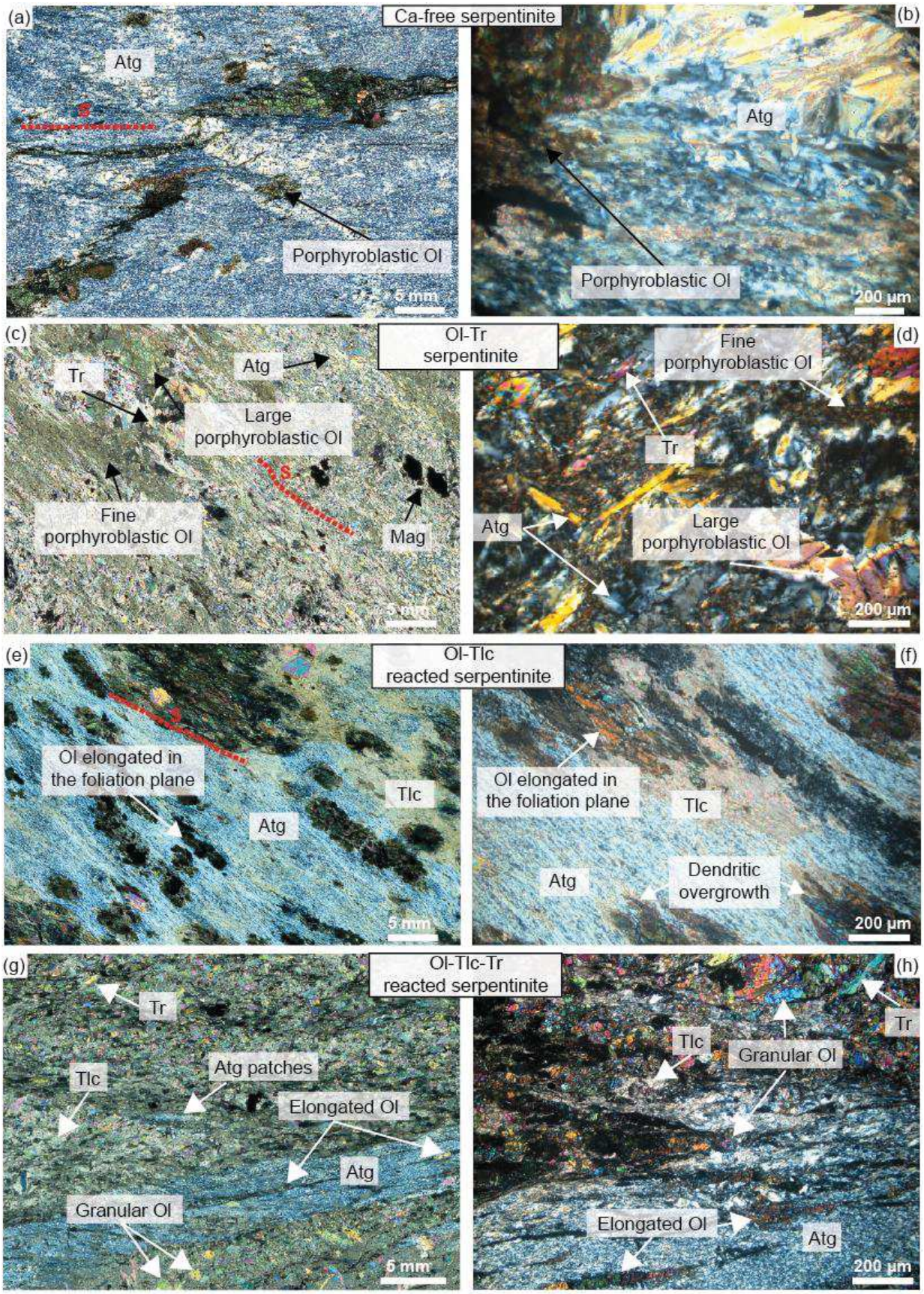

Figure 25 - Optical micrographs with cross-polarized light of representative textures of serpentinites from Val Malenco (a, c, e, g) and their corresponding enlarged area (b, d, f, h). (a) Ca-poor serpentinite that only contain olivine in addition of antigorite. (b) Antigorite crystals may be large (~500 µm) or small (~20 µm) and olivine may be porphyroblastic in the matrix or form Ol-vein. Grain sizes of olivine are both >200 µm (c) Ca-rich serpentinite with tremolite and olivine in equilibrium. (d) Olivine are either granular and < 20 µm size or and porphyroblastic and ~100 µm. (e) Partially reacted serpentinite with ~50% of antigorite and ~50% of Ol-Tlc. (f) Olivine are anhedral and elongated in the foliation plane with serrated overgrowth also elongated in the foliation plane (S). (g-h) Partially reacted Ol-Tlc-Tr serpentinite. Large domains with granular olivine, tremolite and talc have smooth transition to antigorite patches. Olivines connected with each other are elongated parallel to the antigorite band

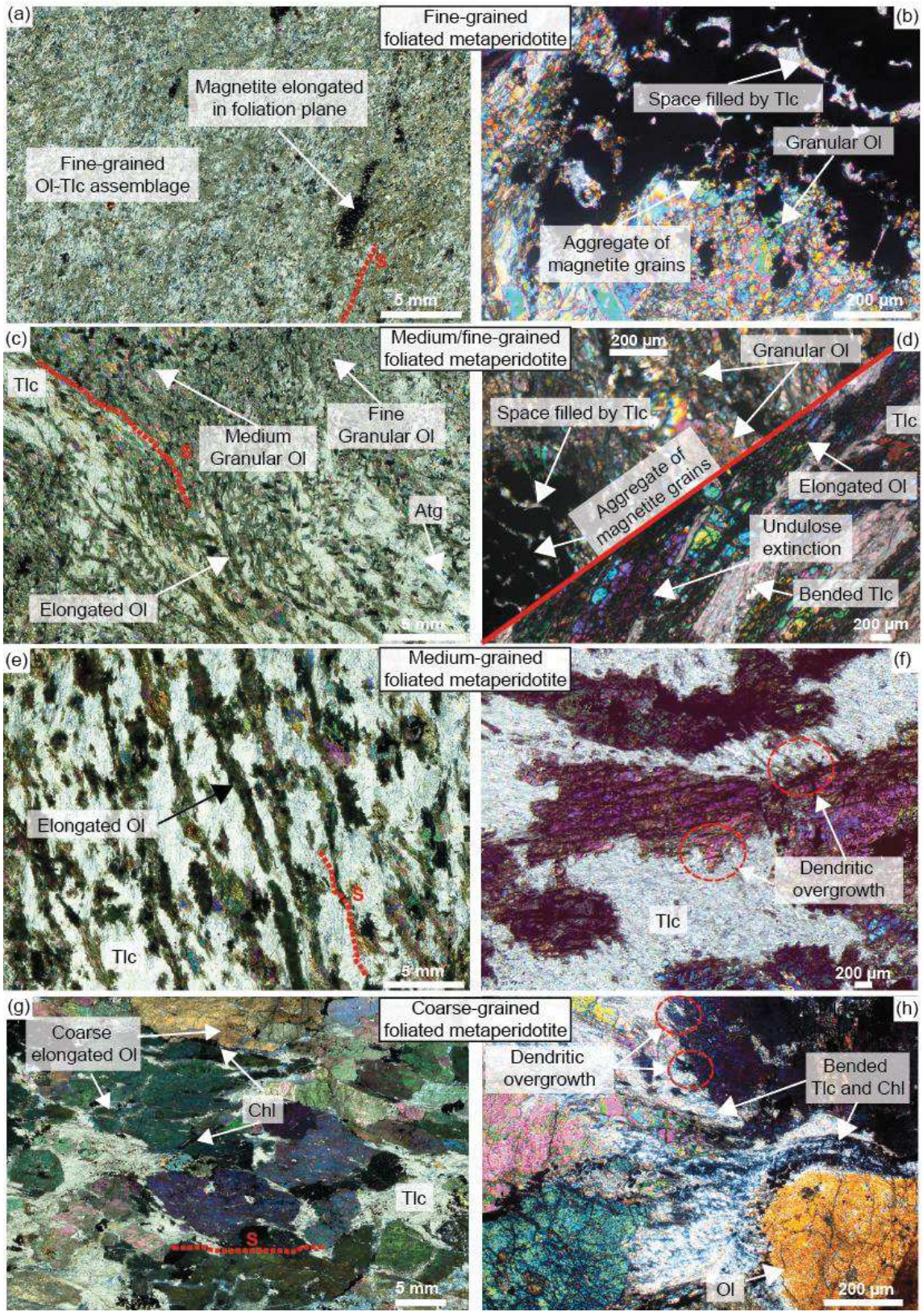

Figure 26 - Optical micrographs with cross-polarized light of representative textures of metaperidotites from Val Malenco (a, c, e, g) and their corresponding enlarged area (b, d, f, h). (a) Fine-grained Ol-Tlc metaperidotite with aggregates of magnetite crystals elongated in the foliation plane (S). (b) Average size of olivine crystals is ~20 µm and aggregates of magnetite have talc crystals in space between magnetite grains. (c) Medium-grained Ol-Tlc metaperidotite with irregular foliation plane and irregular distribution of olivine and talc with areas that have higher content of olivine or talc. Granular olivines may be medium-grained size (>200µm) or fine-grained size (<200µm). (d) Granular olivines with fine-grained size associated with aggregate of magnetite grains "filled" by talc crystals. Olivines elongated in foliation plane are medium-grained size and sometimes show undulose extinction. Talc crystals may also be bended between olivine grains. (e) Medium-grained size metaperidotite with olivine elongated in the foliation plane. Some olivine grains have undulose extinction and (f) most of them have skeletal shape with irregular overgrowths. (g) Coarse-grained Ol-Tlc metaperidotite. Olivine crystals are also elongated, mm-scale and may have undulose extinction. (h) serrated irregular overgrowth is also present at the edge of crystals. Chlorite and talc patches in this sample may be compressed between olivine grains.

extensional cracks (**Fig.** 26b). Fine-grained metaperidotites with olivines <20 µm grade into medium grained peridotites with olivines >100 µm that are either granular or roughly elongated marking a poorly defined foliation plane (**Fig.** 26c). Both granular and elongated olivine with fine-to-medium grain size may show undulose extinction and talc crystals are bent around olivine grains. Medium/fine-grained metaperidotites also contain aggregates of magnetite grain with elongated spaces "filled" with talc crystals in the granular domains (**Fig.** 26d). Metaperidotites with medium-grained olivine (mm-size crystals) are also foliated, with the foliation being marked by both the orientation of tabular olivine and of talc crystals (**Fig.** 26e). Serrated overgrowth is present at the edges of some olivine crystals, which often have undulose extinction (**Fig.** 26f). Coarse-grained metaperidotite are minor within the study area. They are composed by cm-long olivine crystals with skeletal shapes that are flattened in the foliation plane. These crystals show serrated overgrowths and sometimes display undulose extinction (**Fig.** 26g). Chlorite and talc are bended around the olivine grains (**Fig.** 26h).

4.2.2. Metamorphic veins

Ol- and Ol-Tr veins have sharp contact with antigorite matrix at macroscopic scale, but not at the microscopic scale. Ol-veins are mainly composed of coarse cm-scale olivine crystals (**Fig.** 27a, upper half). However, some veins are composed by small olivine crystals that have granular textures in the core of the vein, but tabular in the external domains of the vein. These tabular crystals appear oriented parallel to the foliation plane defined by antigorite in the surrounding peridotite, which often is oblique to the vein trend (**Fig.** 27a, lower half).

Jackstraw Ol-Tlc veins are defined by blade-like or prismatic olivine crystals arranged in a crisscross pattern (**Fig.** 27b) with no apparent preferred orientation of the olivine crystals and interstitial talc (**Fig.** 27c). Olivine crystals tend to be coarser (centimetric) in veins containing small crystals of interstitial carbonates (**Fig.** 27b), whereas in veins with no carbonate, they are usually milimetric (**Fig.** 27c). Most Ol-Tlc veins display a progressive transition to the surrounding serpentinite with olivine crystals and talc flakes that start to grow in the antigorite matrix (**Fig.** 27c,d). In the thinner veins (≤ cm-wide), these olivine crystal elongation is dominantly oriented parallel to the vein trend (**Fig.** 27d). Some veins display in their central part a continuous

domain where the olivine crystals have significantly lower inclusion densities (lower right corner of **Fig.** 27f). Wide Ol-Tlc veins usually show a more developed transition zone, characterized by olivines elongated in the foliation plane defined by antigorite and progressive apparition of talc. These elongated olivine are interspersed with antigorite patches also elongated parallel to the foliation plane (**Fig.** 23a).

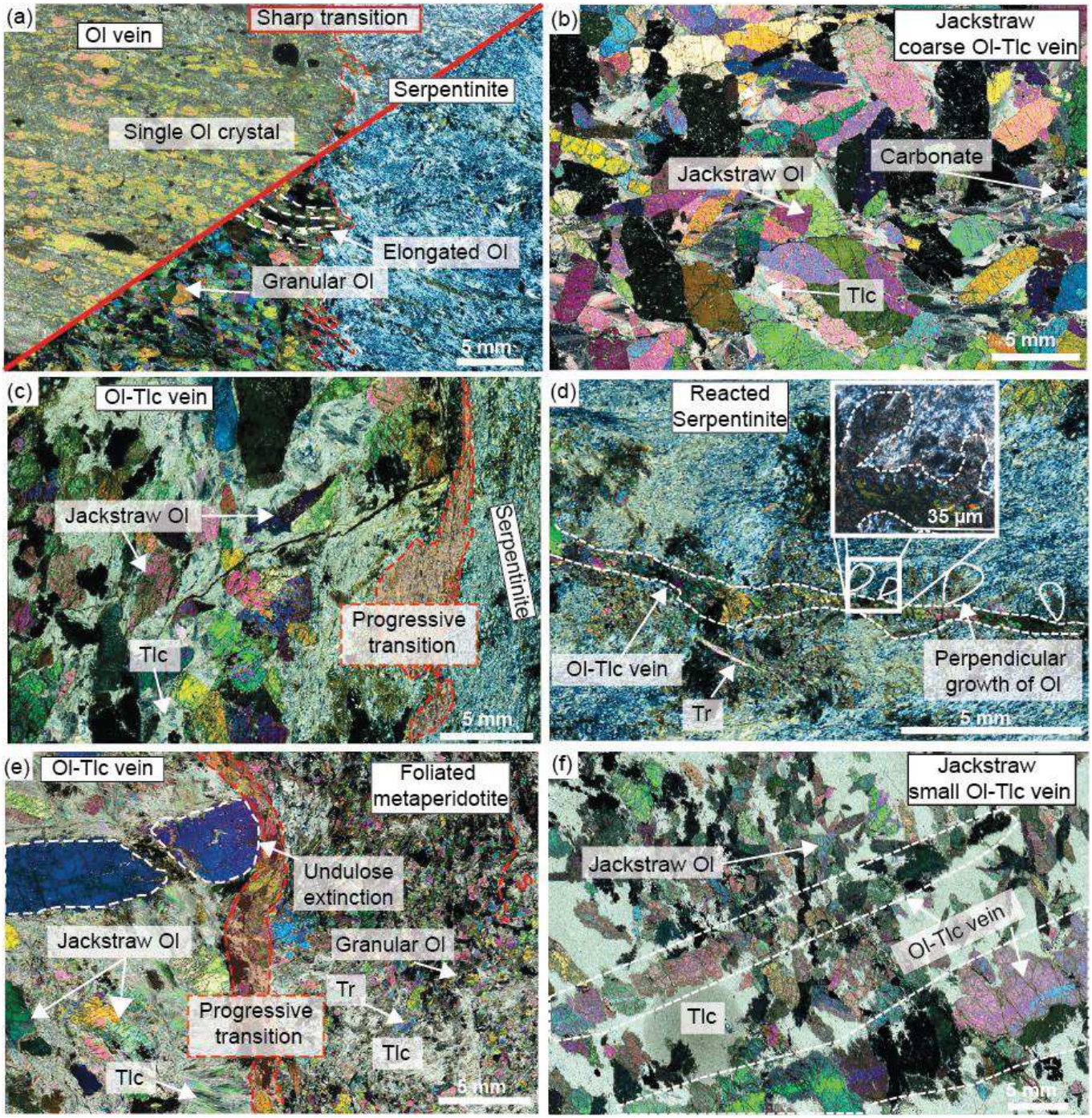

Figure 27 - Optical micrographs of representative veins from Val Malenco with crosspolarized light. (a) Ol-vein cutting sharply serpentinite matrix. The vein is composed of numerous small equant olivine grains and olivines elongated at the reaction front. (b) Typical Jackstraw olivine texture: olivine grains are blade-like elongated (mm-long) with crisscross pattern. Talc patches are in a minor amount between olivine grains and carbonate crystals were also observed. (c) Jackstraw Ol-Tlc vein crosscutting serpentinite matrix. Transition between the vein and the serpentinite is smooth and progressive. (d) Ol-Tlc vein in a reacted serpentinite with growth of olivine perpendicular to the orientation of the vein, as observed at the outcrop scale in Figure 3b. (e) Ol-Tlc vein crosscutting foliated metaperidotite. Olivines in the vein have jackstraw texture and the biggest olivine crystal has undulose extinction pointing to ductile deformation. Transition between the vein and the metaperidotite is progressive. (e) Small jackstraw Ol-Tlc vein with two olivines rods formed each other by several olivine crystals connected.

Jackstraw-like Ol-Tlc textures also occur in foliated metaperidotites (**Fig.** 20e). They can be recognized by differences of olivine texture and grain sizes. In some cases, olivines within the Jackstraw-like texture are coarser and have tabular or skeletal shapes, whereas in the surrounding metaperidotite olivines are finer grained and granular (**Fig.** 27e). In others, the vein is marked by a change in the orientation of the olivine crystals, which is parallel to the vein-like trend, crosscutting the olivine-talc foliation of the surrounding metaperidotite. Results of detailed microscopic investigations of serpentinites, metaperidotites and veins are summarized in Table 1.

4.3. Crystal preferred orientations

Petrographic investigations by optical microscopy have shown that in foliated serpentinites and metaperidotites, antigorite and olivine have a shape preferred orientation, which marks a foliation. When both phases are present, these orientations seem to be related. In contrast, in the veins, although olivine crystals has a clear SPO oriented with the long olivine dimension in the plane of the vein, the relationship with antigorite is unclear. We performed EBSD analyses to better constrain these orientation relationships.

4.3.1. Serpentinites and metaperidotites

Figure 28 illustrates the evolution of the relationship between antigorite and olivine CPOs along a profile normal to the contact with the Bergell intrusion, which is reported as a thick black line on **Figure** 20c. The samples used for this analysis are indicated in **Fig.** 20c. All pole **Figure**s were projected in the same geographical reference frame (EW parallel to horizontal axis and NS parallel to vertical axis, **Fig.** 28). The foliations measured in the field are indicated as full lines and those inferred from the CPO as dashed lines.

In most samples, both antigorite and olivine have a clear CPO. The intensity of the CPO of the two minerals is highly variable from sample to sample, but it is correlated. Within a sample, both minerals have either strong or weak CPO (**Fig.** 28). For antigorite, the strongest orientation is usually displayed by the [001] axis, which forms a maximum normal to the foliation plane (measured in the field or inferred from the CPO). This maximum is in most cases accompanied by dispersion in a girdle of [010], which is usually the second better-oriented axis (**Fig.** 28). The strongest orientation in olivine is mainly for [010] axes while [100] and [001] axes are

girdles, which correspond to low BC index value. A clear example is illustrated with the sample MA17-42. Some samples such as MA16-43 display more orthogonal fabrics corresponding to higher BC index values.

All samples display crystallographic orientation relationships between olivine and antigorite (**Fig.** 28). Commonly the distribution of olivine [010] axes is similar to the one of the [001] axes of antigorite in Ol-Tlc partially reacted serpentinite and metaperidotite. However, for Ol-Tr-rich serpentines (e.g. MA16-34; MA16-36), a weak relation between the [100] axes of olivine and the [001] axes of antigorite is observed.

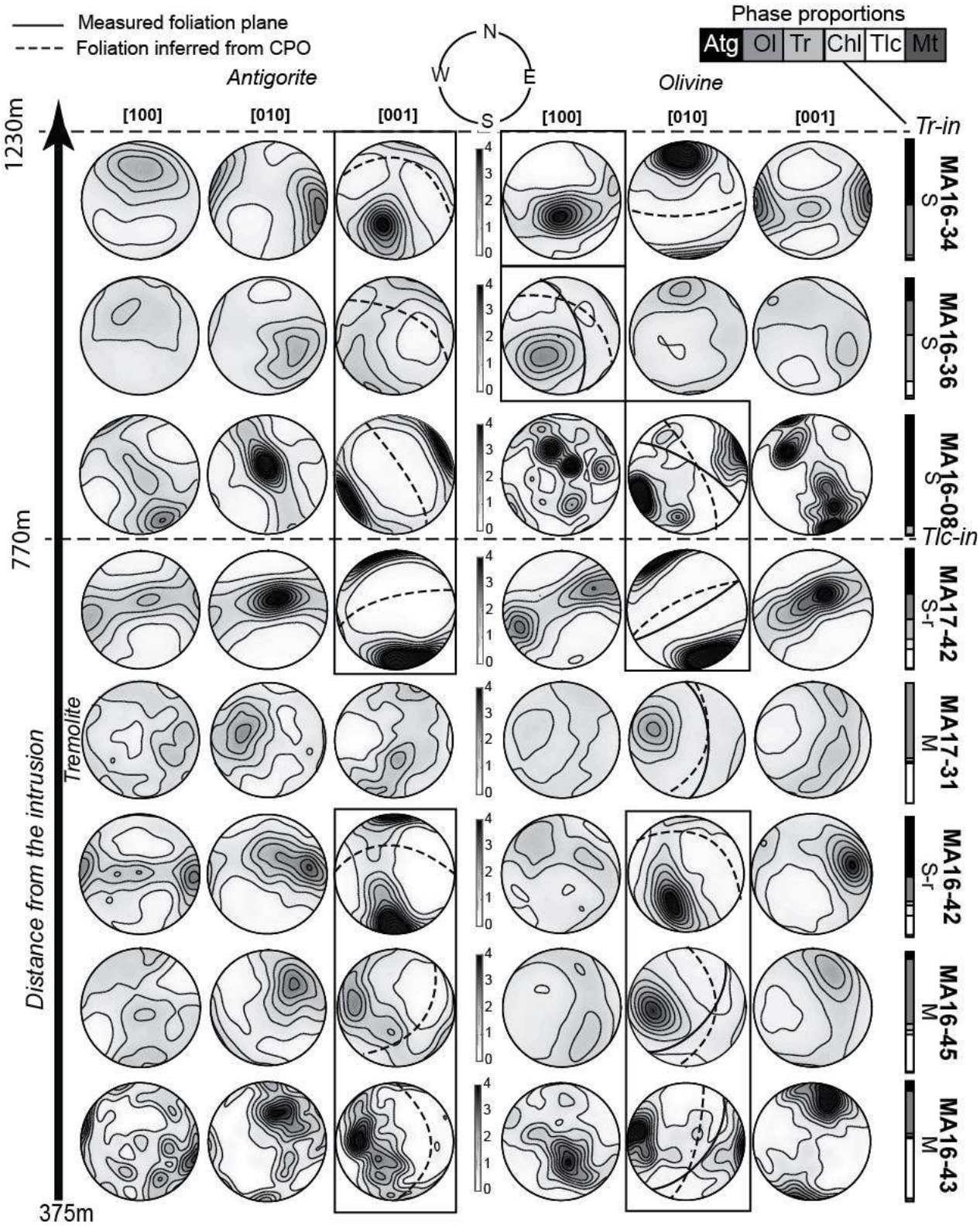

Figure 28 - Pole figures of antigorite and olivine from representative samples of Val Malenco plotted along the profile of Figure 1. Grey rectangle is for tremolite pole figure. Orientations were plotted in geographical frame, as in Figure 5. Lower hemisphere projection. The same colorbar was used for all pole figures to compare the intensity of the texture. Measured foliation plane (thick line) refers to measurements of foliation from outcrops whereas other foliation planes (dotted lines) are inferred from EBSD analyses, $[001]_{Atg}$ and $[010]_{Ol}$. S, S-r and M refer to serpentinite, partially reacted serpentinite and metaperidotite (Table 1). Phase proportions of each sample are also indicated. Strong CPO is observed for most samples and correlations between axes of antigorite and olivine are framed.

Table 1: Representative type of samples observed at Valmalenco and their mineral assemblages

Lithology	Mineral assemblage	Description
Serpentinite		
Serpentinite (S)	Atg +/- Ol(1) +/- Di +/- Tr +/- Ol(2) +/- Chl + Mag +/- Tichu	Dark green to greenish grey, foliated serpentinite with coarse Ol, Di and Tr have granular and acicular shape respectively.
Partially reacted serpentinite(S-r)	Atg +/- Tr +/- Ol(2) +/- Tlc +/- Ol(3) +/- Chl + Mag	Cluster of Atg turning to either Tlc or Tr + Ol in ~50-50% proportions
Metaperidotite		
Foliated metaperidotite (M)	Ol(3) +/- Tlc +/- Tr +/- Atg +/- Chl +/- Atg + Mag	Dark grey with fine-to-coarse grained and foliated Ol associated with Tlc and Tr
Jackstraw texture metaperidotite (Js)	Ol(3) +/- Tlc +/- Tr + Mag	Elongated Ol randomly oriented associated with Tlc and Tr
Veins		
Ol- vein	Ol	Thin to large (cm-dm width) vein with sharp contact with serpentinite matrix. Ol are equant and µm-to-mm scale
Ol-Tr vein	Ol + Tr	Same morphology than previous type of vein but Ol are associated to acicular Tr crystals
Ol-Tlc	Ol + Tlc	Thin to large (cm-dm width) veins with either sharp of irregular contact with serpentinite or metaperidotite host. Ol crystals have generally jackstraw texture

Carbonates crystals were present in minor cases
Text in bracket is abbreviation for lithologies
Numbers in brackets associated to Ol refers to reaction 1, 2 or 3

For metaperidotite MA17-31, in which antigorite is randomly oriented, we present the tremolite CPO which nicely marks the foliation. Tremolite shows a weak point maximum of the [010] axes, which is subparallel to the maximum concentration of the [010] axes of olivine, and a girdle distribution of [001] normal to this maximum.

There is not clear evolution in the intensity of antigorite and olivine CPO with distance from the contact with the Bergell intrusion (**Fig.** 28). For olivine this conclusion is corroborated by the analysis of a larger number of metaperidotites, which shows that neither the olivine CPO intensity (J-index), nor the symmetry (BC-index) displays any correlation with distance from contact. There is also no correlation of the olivine CPO intensity or symmetry with grain size (**Fig.** 29). Axial-[010] olivine CPO (BC-index <0.35) predominate while axial-[001] textures (BC-index>0.65) are rare. Except for one sample, fine-grained metaperidotites have weak olivine CPO (**Fig.** 29).

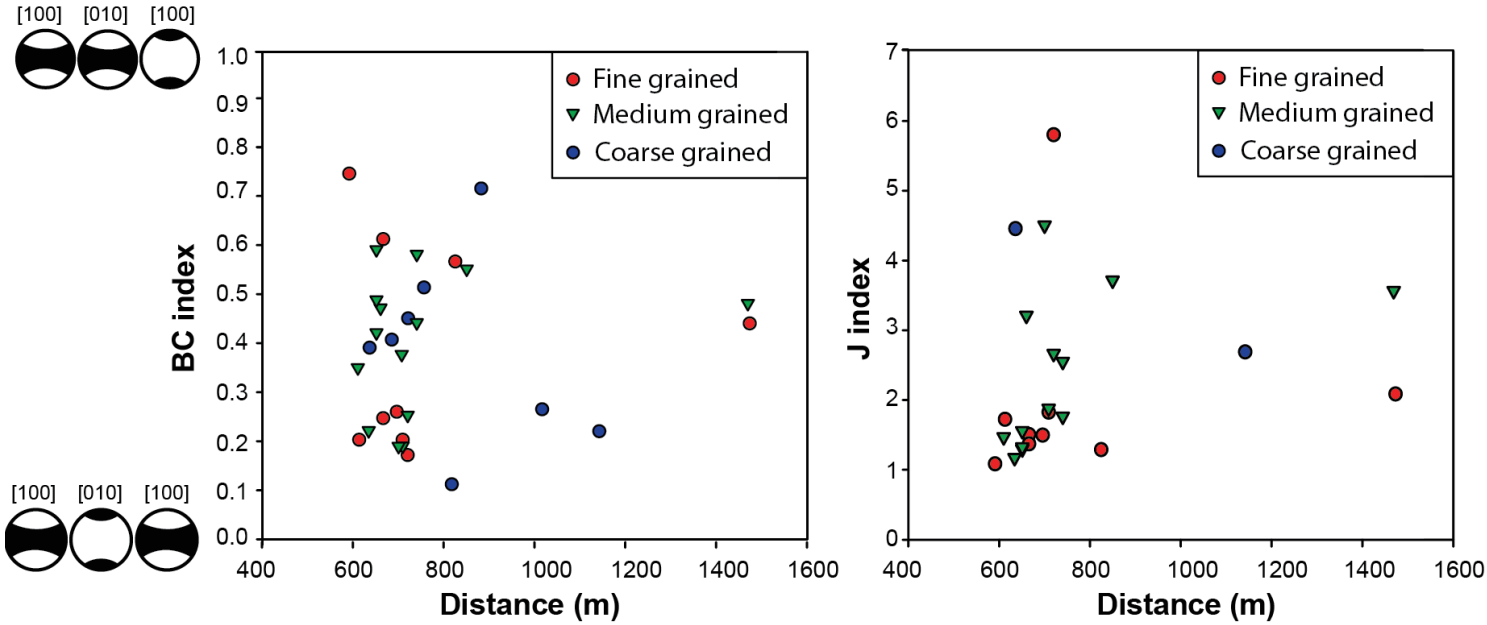

Figure 29 - Microstructure properties determined from EBSD analyses for 3 sizes of olivine grains: fine-grained (< 200 µm), medium-grained (>200 µm and <1 cm) and coarse-grained (>1 cm) (a) texture index (J index) versus BC index (see text for more details on these indexes). Veins were not included in the plot. No correlation is observed between these variables. Fine-grained and medium-grained metaperidotite dominantly have low texture index (< 4) and variable BC index (from 0.18 to 0.75).

4.3.2. Metamorphic veins

Figure 30 illustrates the CPO of olivine and, when present, tremolite in Ol- and Ol-Tr veins as well as the antigorite CPO in the antigorite-schist from the wall rock of the veins.

In Ol-veins and Ol-Tr veins, no clear correlation between orientation of antigorite from the serpentinite wall rock and olivine in the veins is observed. Antigorite is weakly oriented (**Fig.** 30, MA17-10, 16, 17) and olivine grains are either weakly oriented (MA17-16) or the number of grains is too low (MA17-10; MA17-17) to infer any clear CPO. However, a weak correlation is observed between [001] axes of antigorite and few olivine crystals in MA17-10. Tremolite in the vein also displays a weak CPO (**Fig.** 30 MA17-17), which is also not correlated with [001] axes of antigorite host. Nonetheless, correlation is observed between orientation of the veins and [010] axes of olivines, which seem to be normal to the plane of the vein (**Fig.** 30, MA17-10; MA17-17).

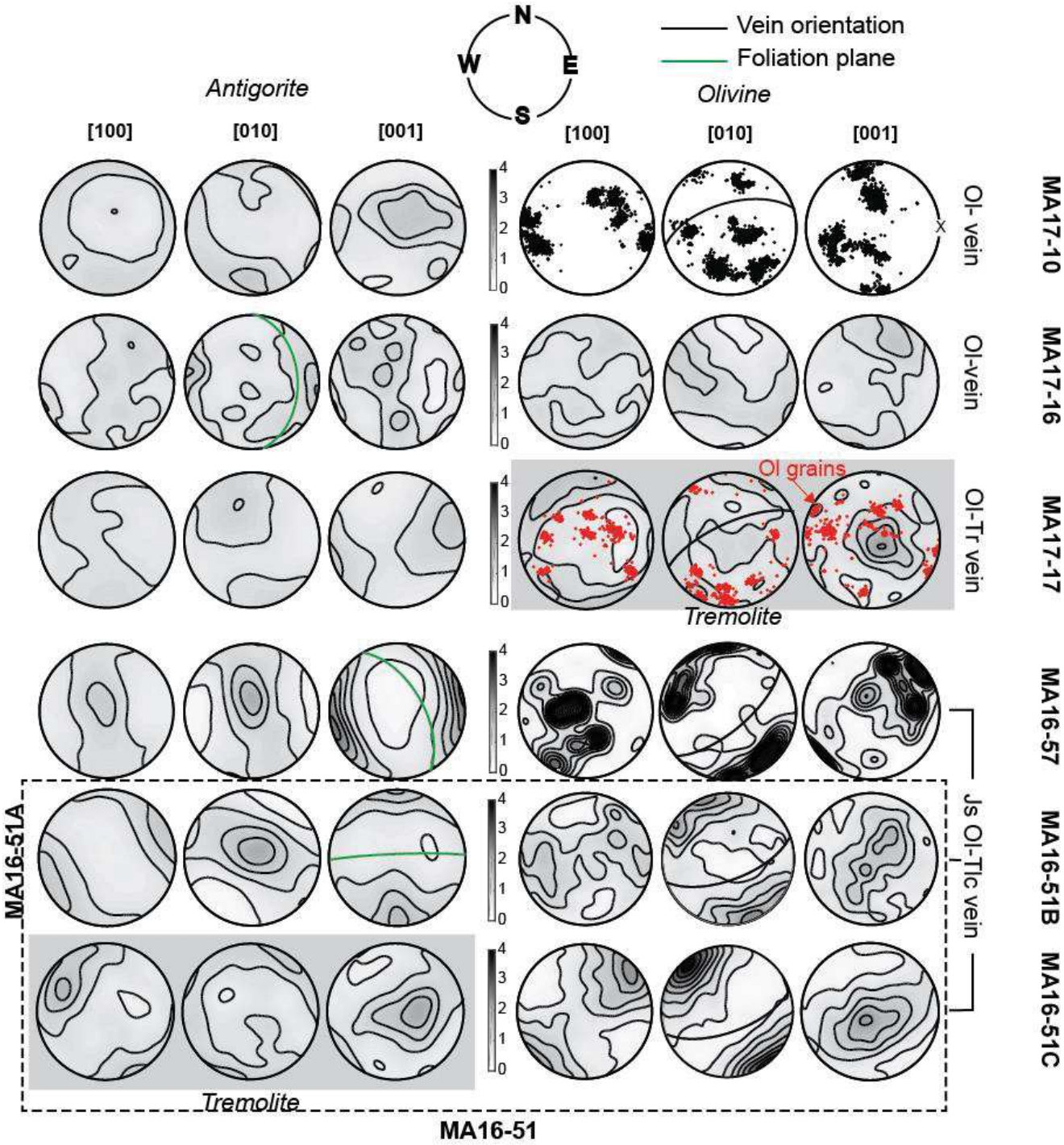

Figure 30 - Pole figures of olivine from representative vein and antigorite from wall rock serpentinite. Grey rectangle is for tremolite pole figure. The type of vein is indicated. The same colorbar was used for all pole figures to compare the intensity of the texture. Thick black line is vein orientation measured in the field and thick green line is foliation plane of antigorite from the wall rock outside the vein. Olivines are poorly oriented in Ol- and Ol-Tr vein but Jackstraw Ol-Tlc have a CPO despite there are no correlation with antigorite from the wall rock. Jackstraw olivines have their [010] axes normal to vein orientation

Olivines in Jackstraw Ol-Tlc veins have a CPO that is not correlated with antigorite of the serpentinite wall rock but with the vein orientation. For MA16-57 and for MA16-51, [010] axes are normal to the plane of the vein while [100] and [001]

axes form a girdle parallel to vein plane (**Fig.** 30). This CPO is consistent with the observation that jackstraw olivines are elongated on the plane of the vein. The pole of the vein planes is therefore correlated with [010] axes in olivine (**Fig.** 30).

4.3.3. Intracrystalline misorientation in olivine

To characterize the olivine deformation, the mean intragranular misorientation of olivine in metaperidotites with variable olivine grain sizes was plotted against the distance to the contact of the Bergell intrusion (**Fig.** 31a). Olivine grain sizes were classified as fine grained (<200 µm), medium grained (>200 µm and <1 cm) and coarse grained (> 1cm). The highest mean intragranular misorientations (>4°) are observed within 900 m from the contact with the Bergell intrusion. However, the lacking of high mean intragranular misorientations farther from the intrusion may be a bias from the less dense sampling in this domain. Otherwise the mean intragranular misorientation in olivine seems to be uncorrelated with distance from the intrusion. Coarse and medium grained olivines have variable misorientation (from 1° to 6°). Fine-grained olivine has a lower range of misorientation (from 1° to 4°), but these lower values may result from a less detailed sampling (lower number of orientation data per grain). Olivine crystals in veins have on average lower misorientation, from 1° to 3° (**Fig.** 31a).

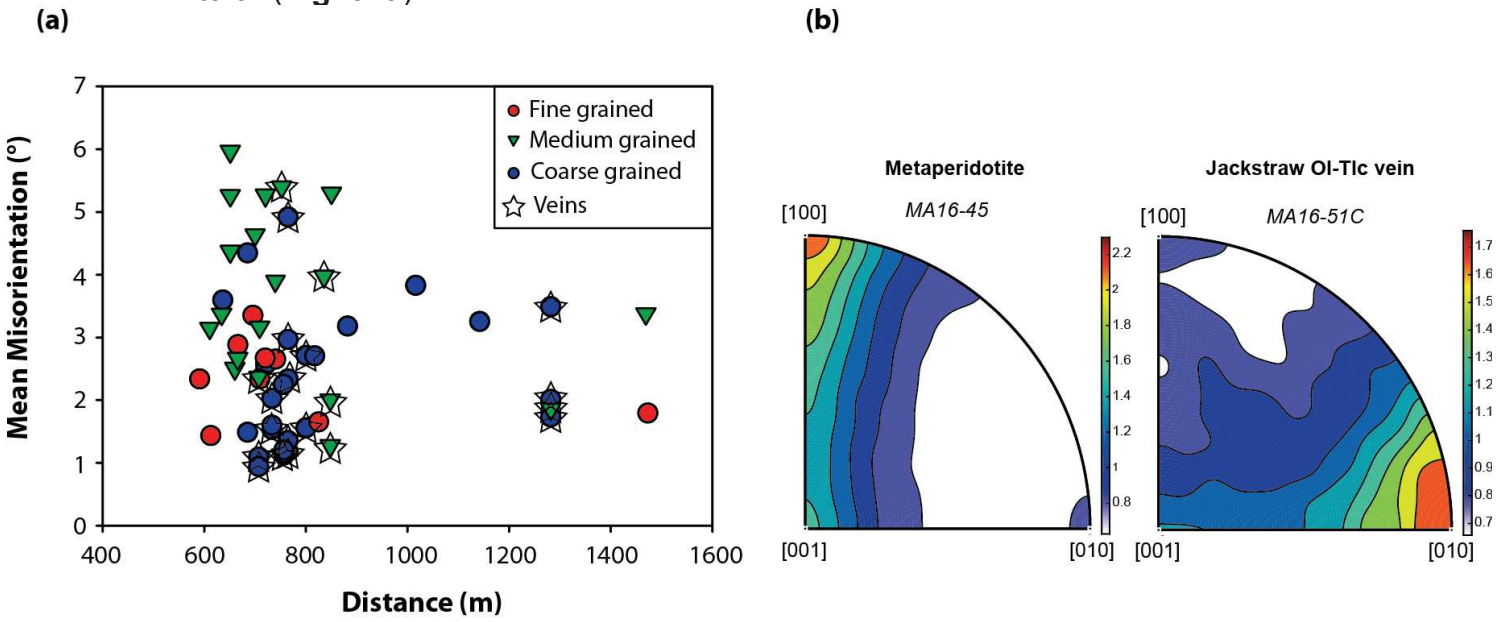

Figure 31 - Mean misorientation in olivine grains versus the distance from the intrusion. Veins were included in the plot and are mostly coarse-grained. Coarse- and medium-grained olivines have variable misorientation (1-6°) and fine-grained olivines have lower range of misorientation (1-4°). Olivines in veins have also low misorientation (1°-3°). No correlation is observed with the distance from the intrusion. (b) Inverse pole figures of intragranular misorientation of olivines from a representative metaperidotite and from jackstraw Ol-Tlc vein

Olivines in veins on the other side do not display undulose extinction consistent with low values of misorientation (**Fig.** 31a). Moreover, intragranular misorientation of olivines plotted with inverse pole figure show that in representative metaperidotite sample, rotation axes are mainly [100] and in jackstraw Ol-Tlc vein, rotation axes are mainly [010] axes. Intraganular misorientation of olivine elongated in the foliation plane of antigorite of the vein from **Figure** 23b also display that rotation axes are [100], similar to olivines from metaperidotites.

4.4. Chemical compositions

4.4.1. Bulk rock compositions

Bulk rock compositions are shown in Table 2 and plotted in a projected MSH ternary diagram (**Fig.** 32) using CSpace (Torres-Roldan *et al.*, 2000). Mineral and bulk-rock analyses were projected from tremolite, chlorite and magnetite and the exchange vector $Fe_{-1}Mg_{1}$, $Mn_{-1}Mg_{1}$ and $Ni_{-1}Mg_{1}$. In addition to measured bulk-composition, the projections also include calculated compositions based on phase abundances obtained by means of EBSD mapping and mean composition of each phase determined from EPMA analyses (Table 2-5).

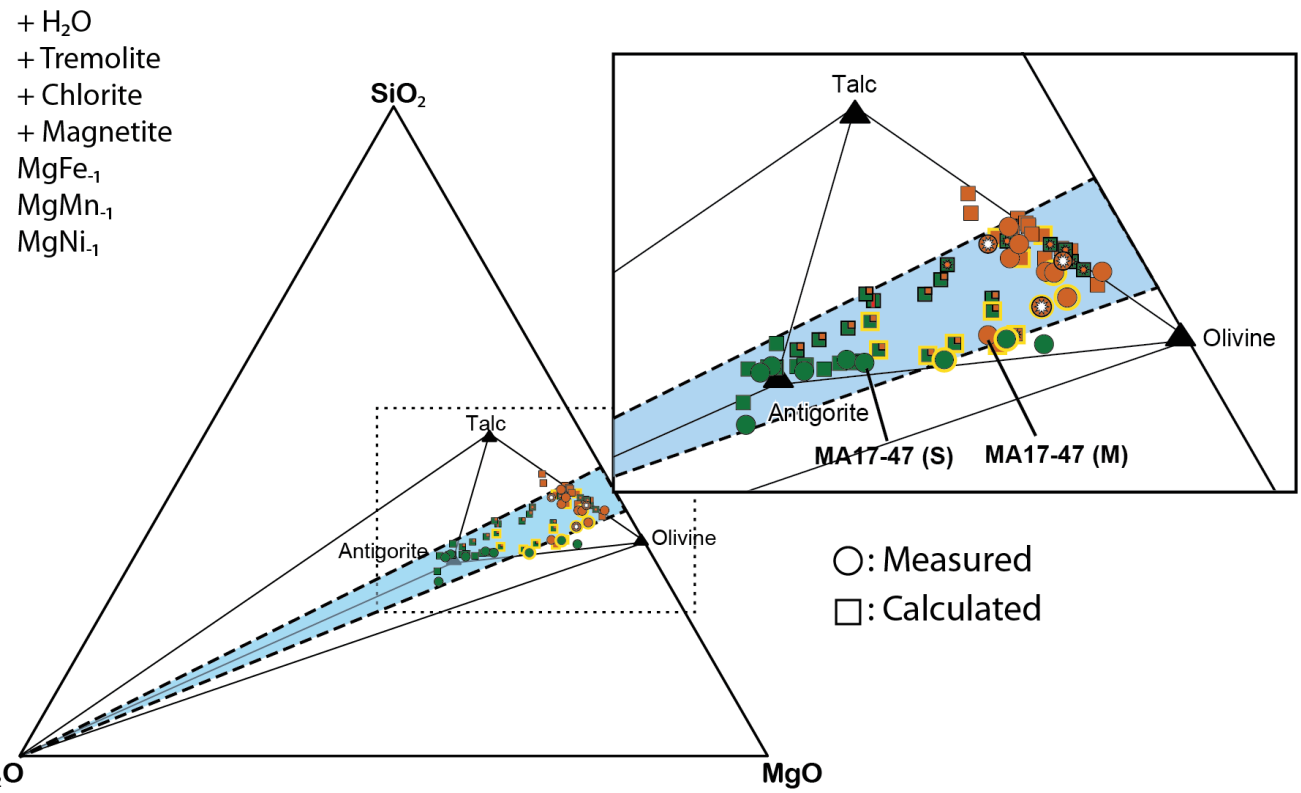

Figure 32 - Ternary diagram in the MgO-SiO_2-H_2O (MSH) system for measured and calculated bulk composition of all samples from Val Malenco. Projection was performed from tremolite, chlorite, magnetite and vectors $MgFe_{-1}$, $MgMn_{-1}$, $MgNi_{-1}$. Chlorite projection applies only to metaperidotites. Estimation of the bulk rock composition was performed using phase abundances from EBSD analyses and mean compositions of phases determined by EPMA. The blue field shows the possible range in product proportions expected from the composition of the observed serpentinite. Samples out of this stability field have to have undergone a change of their compositions. Symbols used are the same than Figure 1c.

Table 2: Bulk compositions of representative samples from Valmalenco

Sample	MA16-17	MA16-36	MA16-42	MA17-34	MA16-48	MA16-12A	MA17-47	
Type	S	Ca-rich S	S-r	M	M	Js	S	Js
SiO_2	42.02	45.97	45.94	46.24	42.36	43.59	40.29	41.72
TiO_2	0.01	0.01	0.01	0.01	0.01	0.01	0.01	0.00
Al_2O_3	0.99	1.02	2.20	1.15	1.39	0.79	1.17	0.93
Cr_2O_3	0.36	0.43	0.39	0.47	0.53	0.52	0.59	0.49
Fe_2O_3	2.53	4.16	0.87	3.08	4.97	2.16	6.95	3.35
FeO	4.46	2.54	4.20	3.90	5.25	7.12	3.48	4.08
NiO	0.20	0.27	0.21	0.29	0.31	0.26	0.28	0.33
MnO	0.09	0.10	0.09	0.09	0.14	0.23	0.08	0.14
MgO	37.55	34.76	37.54	39.79	41.57	41.31	37.17	42.07
CaO	0.01	5.12	0.50	0.24	0.08	0.61	0.87	0.47
Na_2O	0.01	0.02	0.02	<0.01	<0.01	<0.01	0.87	0.47
LOI	11.20	5.30	8.04	4.30	2.70	2.60	8.70	6.00
Total	99.42	99.70	99.79	99.55	99.31	99.19	100.18	99.71
Mode (vol. %)								
Antigorite	98.43	18.63	50.71	0.00	0.52	1.37	62.23	26.21
Olivine	0.00	28.61	20.27	46.67	68.42	70.34	31.53	50.87
Diopside	0.00	0.00	0.00	0.00	0.00	0.00	0.00	0.00
Tremolite	0.00	38.45	3.65	5.77	0.00	0.00	0.81	5.45
Chlorite	0.00	10.22	8.35	1.05	7.09	0.00	1.02	1.02
Talc	0.00	0.00	15.66	44.09	20.26	27.26	4.06	15.29
Magnetite	1.57	4.09	1.36	2.41	3.72	1.02	0.35	1.15

Ferric iron was calculated from the difference of the total iron measured and the measured ferrous iron

Measured and calculated compositions for serpentinites plot close to the antigorite pole, with a variable amount of olivine. Metaperidotites plot on the talc-olivine tie line with variable proportions of talc and olivine (**Fig.** 32). The observed range in talc and olivine proportions is within the predictions for dehydration of rocks with the composition of the serpentinites from Val Malenco in a close system (except for H_2O), which is indicated by blue field in **Figure** 32. Ol-Tlc veins also globally plot within the same field of metaperidotites. Calculated compositions of partially reacted serpentinites plot inside the Atg-Tl-Ol field. Samples out of the blue field have compositions either enriched in talc or in olivine not consistent with the predictions for a dehydrating serpentinite with a composition close to antigorite pole (**Fig.** 32).

Table 3: Composition of Olivine in representative samples from Valmalenco

Sample	S MA16-18	S-r MA16-34	S-r MA17-47(3)	S-r MA17-47(2)	Js MA17-47(1)	Js MA17-22	M MA17-34(2)	M MA16-48	M MA17-37A
n	5	4	5	12	10	8	9	12	10
SiO_2	41.36	41.31	41.31	41.33	41.40	40.51	41.25	41.32	40.97
FeO	6.85	6.28	7.30	7.15	7.57	11.08	7.73	7.55	9.98
NiO	0.32	0.35	0.47	0.47	0.29	0.27	0.35	0.36	0.31
MgO	50.47	50.38	50.54	50.47	50.22	47.21	49.52	49.82	48.36
MnO	0.38	0.29	0.23	0.24	0.25	0.30	0.17	0.20	0.20
Total	99.42	98.62	99.89	99.72	99.75	99.42	99.05	99.30	99.86
O	4.00	4.00	4.00	4.00	4.00	4.00	4.00	4.00	4.00
OH	0.00	0.00	0.00	0.00	0.00	0.00	0.00	0.00	0.00
Si	1.007	1.010	1.003	1.005	1.007	1.005	1.011	1.009	1.006
Fe	0.140	0.128	0.148	0.145	0.154	0.230	0.158	0.154	0.205
Ni	0.006	0.007	0.009	0.009	0.006	0.005	0.007	0.007	0.006
Mg	1.831	1.837	1.830	1.829	1.821	1.746	1.809	1.814	1.771
Mn	0.008	0.006	0.005	0.005	0.005	0.006	0.003	0.004	0.004
Sum cation	2.993	2.990	2.997	2.995	2.993	2.994	2.989	2.990	2.994
XMg	0.929	0.935	0.925	0.926	0.922	0.884	0.919	0.922	0.896

Abbreviations are listed in Table 1
Cations were calculated with O= 4

Table 4: Composition of Talc in representative samples from Valmalenco

Sample	S-r MA16-50	Js MA16-12	Js MA16-57	M MA17-34	M MA17-36	M MA16-48	M MA16-45	M MA16-43
n	4	12	7	9	9	38	5	14
SiO_2	62.29	61.30	62.26	60.53	61.45	61.51	61.99	62.07
Al_2O_3	0.21	0.47	0.17	0.36	0.41	0.37	0.16	0.18
Cr_2O_3	0.09	0.12	0.08	0.09	0.12	0.03	0.03	0.02
FeO	1.61	1.34	1.04	1.12	1.04	1.00	1.13	0.99
NiO	0.15	0.15	0.22	0.20	0.17	0.19	0.24	0.17
MgO	29.71	30.97	30.23	31.62	31.23	31.72	30.98	30.18
Na_2O	0.06	0.04	0.03	0.06	0.09	0.05	0.05	0.05
H_2O	4.66	4.66	4.66	4.64	4.67	4.69	4.68	4.65
Total	98.78	99.08	98.69	98.62	99.14	99.56	99.24	98.30
O	11.00	11.00	11.00	11.00	11.00	11.00	11.00	11.00
OH	2.00	2.00	2.00	2.00	2.00	2.00	2.00	2.00
Si	4.008	3.940	4.003	3.913	3.941	3.930	3.971	4.004
Al	0.016	0.036	0.013	0.028	0.032	0.029	0.012	0.014
Cr	0.004	0.006	0.004	0.005	0.006	0.002	0.001	0.001
Fe	0.087	0.072	0.056	0.061	0.056	0.054	0.061	0.053
Ni	0.008	0.008	0.011	0.010	0.009	0.010	0.013	0.009
Mg	2.850	2.970	2.897	3.047	2.988	3.025	2.959	2.903
Na	0.008	0.005	0.004	0.008	0.011	0.007	0.006	0.006
Sum cation	6.984	7.041	6.990	7.074	7.045	7.058	7.025	6.991
XMg	0.971	0.976	0.981	0.981	0.982	0.983	0.980	0.982

Abbreviations are listed in Table 1
Cations were calculated with O= 11

Table 5: Compositions of Tremolite in representative samples of Valmalenco

Sample	Ca-S MA16-23	S-r MA16-34	S-r MA17-47	Js MA16-51C	M MA16-45	M MA16-46
n	2	10	1	0	2	7
SiO_2	58.22	57.76	56.52	58.13	58.00	57.89
Al_2O_3	0.07	0.12	0.11	0.15	0.17	0.30
Cr_2O_3	0.03	0.03	0.08	0.06	0.08	0.04
FeO	1.18	1.08	4.49	1.41	1.22	1.48
NiO	0.08	0.07	0.14	0.06	0.12	0.10
MgO	23.38	24.75	24.50	23.28	24.76	24.62
MnO	0.09	0.05	0.06	0.08	0.17	0.05
CaO	13.55	13.53	12.99	13.24	13.08	13.29
Na_2O	0.04	0.02	0.09	0.06	0.13	0.22
H_2O	96.71	97.46	99.01	96.45	97.73	98.04
Total	2.18	2.19	2.19	2.18	2.20	2.20
O	98.82	99.61	101.08	98.61	99.80	100.01
OH	23.00	23.00	23.00	23.00	23.00	23.00
Si	4.794	5.045	5.008	4.784	5.032	4.997
Al	8.009	7.897	7.744	8.012	7.907	7.883
Cr	0.003	0.004	0.009	0.006	0.008	0.005
Fe	0.011	0.020	0.018	0.025	0.027	0.048
Fe^{3+}	0.136	0.123	0.524	0.163	0.139	0.169
Ni	0.009	0.008	0.016	0.006	0.014	0.011
Mg	0.012	0.006	0.024	0.016	0.035	0.058
Mn	0.010	0.006	0.007	0.009	0.020	0.006
Ca	1.996	1.981	1.906	1.954	1.910	1.939
Na	2.00	2.00	2.00	2.00	2.00	2.00
Sum cation	14.984	15.093	15.254	14.978	15.092	15.118
XMg	0.972	0.976	0.919	0.967	0.973	0.967

Abbreviations are listed in Table 1

Cations were calculated with O= 23

Table 6: Compositions of Antigorite in representative samples of Valmalenco

Sample	S MA16-18	S MA16-17	S-r MA16-34	Ca-S MA16-23(2)	S-r MA17-47(3)	S-r MA17-47(2)	Js MA17-47(1)	Js MA17-22	M MA17-34(2)
n	5	10	4	5	14	8	5	4	4
SiO_2	43.10	43.91	42.47	42.48	43.58	44.05	43.92	44.81	43.32
TiO_2	0.02	0.02	0.00	0.03	0.01	0.01	0.01	0.02	0.02
Al_2O_3	1.81	1.03	2.49	2.67	2.00	1.99	2.32	3.14	1.89
Cr_2O_3	0.27	0.19	0.33	0.26	0.39	0.52	0.75	0.53	0.34
FeO	2.80	2.94	3.01	3.33	3.03	2.81	2.89	3.76	3.05
NiO	0.14	0.12	0.16	0.16	0.20	0.19	0.18	0.11	0.13
MgO	37.68	37.66	37.41	36.90	37.28	37.35	37.00	34.98	37.65
MnO	0.04	0.09	0.04	0.07	0.04	0.03	0.05	0.05	0.03
H_2O	11.89	11.91	11.87	11.86	11.98	12.06	12.07	12.12	11.96
Total	97.76	97.89	97.79	97.80	98.52	99.01	99.19	99.52	98.39
O	6.82	6.82	6.82	6.82	6.82	6.82	6.82	6.82	6.82
OH	3.65	3.65	3.65	3.65	3.65	3.65	3.65	3.65	3.65
Si	1.982	2.015	1.956	1.958	1.989	1.998	1.990	2.019	1.981
Ti	0.001	0.001	0.000	0.001	0.000	0.000	0.001	0.001	0.001
Al	0.098	0.056	0.135	0.145	0.108	0.106	0.124	0.166	0.102
Cr	0.010	0.007	0.012	0.009	0.014	0.019	0.027	0.019	0.012
Fe	0.108	0.113	0.116	0.128	0.116	0.107	0.110	0.143	0.117
Fe^{3+}	0.000	0.000	0.000	0.000	0.000	0.000	0.000	0.000	0.000
Ni	0.005	0.004	0.006	0.006	0.007	0.007	0.007	0.004	0.005
Mg	2.583	2.577	2.568	2.536	2.537	2.525	2.499	2.358	2.567
Mn	0.002	0.003	0.001	0.003	0.002	0.001	0.002	0.002	0.001
Sum cation	4.788	4.777	4.795	4.788	4.774	4.764	4.759	4.713	4.786
XMg	0.960	0.958	0.957	0.952	0.956	0.960	0.958	0.944	0.956

Abbreviations are listed in Table 1
Cations were calculated with antigorite polysome m=17 and O= 6.824

4.4.2. Mineral compositions

Olivine has a X_{Mg} (Mg/(Mg+Fe) in atoms per formula unit) ranging from 0.86 to 0.96 (except some exceptional tremolite-chlorite rich rocks where olivine has a X_{Mg} of 0.77). The analysis of the Mn content versus X_{Mg} of olivine (**Fig.** 33) allows discriminating olivines produced by the different dehydration reactions (**Fig.** 20b). Olivine from serpentinites have 0.008 apfu of Mn and X_{Mg} of ~0.92. Olivines from Ca-

rich serpentinites, with diopside or tremolite have up to 0.010 apfu of Mn and X_{Mg} of 0.87 and 0.006 apfu of Mn and X_{Mg} of 0.94, respectively. Olivine from partially reacted serpentinites has 0.004 apfu of Mn and X_{Mg} of 0.87.

Olivine from metaperidotites has a wide range of Mn and X_{Mg}, from 0.002 to 0.006 apfu of Mn and X_{Mg} from 0.89 to 0.95. Jackstraw olivine have also wide range which overlap with those of the metaperidotite. Olivine composition in samples from Trommsdorff and Evans (1972) display similar variations in X_{Mg} and Mn content (**Fig.** 33).

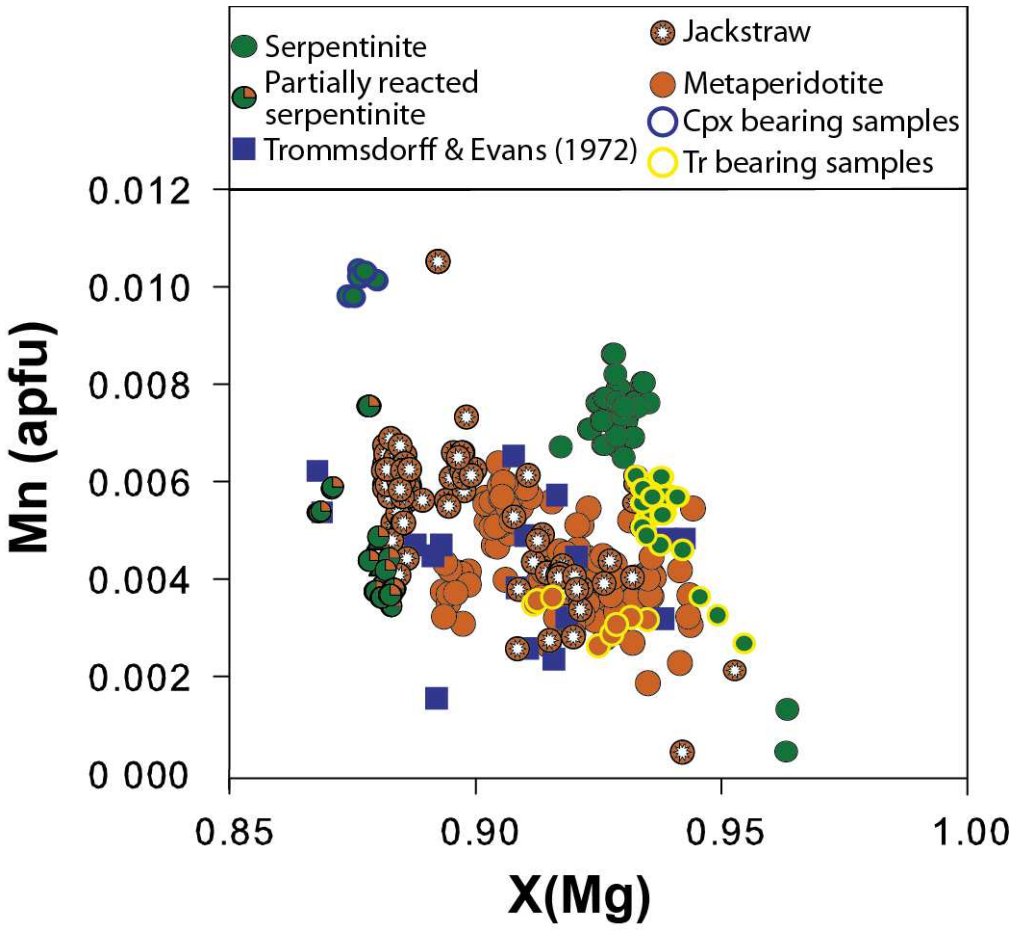

Figure 33 - X_{Mg} vs Mn diagram of olivine in each type of representative samples from the studied area in Val Malenco. Symbols used are the same than in Figure 1c and Figure 11.

Compositions of other prograde minerals are also roughly constant. Talc have a nearly constant X_{Mg} of 0.98 and nearly constant amount of Si (3.96 apfu) that do not seem to be affected by the distance from the intrusion (Table 4). The same is true for tremolite, with an almost constant X_{Mg} of 0.97, a Ca amount of 1.95 apfu and a Si

amount of roughly 4.95 that do no seem to be affected by the distance from the intrusion. (Table 5)

Antigorite has also a roughly constant composition in serpentinites with a X_{Mg} of ~0.96, indistinguishable from the reacted serpentinites or the small lenses in metaperidotites. The distance from the intrusion does not seems to affect the X_{Mg} of antigorite of each type of samples.

The EPMA chemical profile from **Figure** 23c shows a slight increase (from 0.921 to 0.927) and then a slight decrease (from 0.927 to 0.923 of X_{Mg} in olivine from A' to A and a slight increase of Al in antigorite (0.11 to 0.13).

5. DISCUSSION

5.1. Role of veins on fluid migration and reaction rate

Veins allow large volumes of fluid to migrate fast. Here, fluids are produced by dehydration reaction of antigorite and may not come from Bergell intrusion because no accessory phase typical of magmatic fluids was observed. Thus, unlike veins observed in many natural cases for quartz-gold vein deposits (Cole *et al.*, 2000) or calcite veins in serpentinite from Val Malenco (Trommsdorff and Evans, 1977), silicate veins from Val Malenco may be considered as pathways for draining fluids and not injecting fluids responsible of mineral precipitation. Furthermore, these veins allow dehydration reaction to occur at lower temperature as they were found in partially reacted area corresponding to lower grades of contact metamorphism.

Indeed, it is corroborated by previous work (Fyfe et al., 1958; Coombs et al., 1959; Coombs 1993) that show that veins resulting from dehydration in an open-system may form at lower temperature than temperatures for the same reaction in a closed-system where the fluid pressure equal the confining pressure. The chemical potential of H_2O is the main variable in such open system, which needs to be lower than the one corresponding to fluid saturation for the given confining pressure (Greenwood, 1961). The reduction of the H_2O chemical potential in the crack may have been triggered by either [1] infilling of the fracture by external fluids rich in other components such as CO_2 (e.g. Evans & Trommsdorff, 1974) or [2] release of H_2O-aqueous fluid by dehydration of antigorite aiming to homogenize the chemical potential gradient created across the crack. The first mechanism may have played a

role locally, as some veins have magnesite. However, most veins are isochemical (Fig. 32) and therefore they must have formed by the second mechanism, without any influx of external fluids.

5.1.1. Olivine texture and fluid flow in veins

Ol-Tlc veins (**Fig.** 22d-g) record reaction (3) occurring at lower temperatures than its equilibrium conditions (**Fig.** 20b). Olivine in these veins has a peculiar texture as they have blade-like shapes randomly elongated on the plane of the vein (**Fig.** 22f; **Fig.** 27c). They have variable sizes and a clear CPO with [010] axes normal to the plane of the vein (**Fig.** 30d). This type of texture seems similar to those briefly reported from Norwegian metaperidotites (Bakke and Korneliussen, 1986), metaperidotites from Klamaths Moutains (California, USA, Snoke and Calk, 1978). It bear also some resemblace to the metaperidotites from Cerro del Almirez (SE Spain) with the spinifex-like texture. Both have a remarkable similar SPO (Kahl *et al.*, 2017) although olivine from the spinifex-like texture show a much stronger orthogonal fabric (Padrón-Navarta *et al.*, 2011).

Changes in olivine grain shapes in dehydrating rocks may reflect different growth kinetics and possibly different mechanisms of fluid migration. Indeed, in magmatic systems, different olivines crystal shapes correspond to different growth mechanisms in unconstrained systems (free growth): experimental study from Donaldson (1976) have reported ten shapes of olivines depending of the rate of undercooling. They were classified in three types in a more recent work (Faure *et al.*, 2003) depending on the cooling rate and the degree of undercooling: olivines with tablet shape are progressively replaced to skeletal and then to dendritic shape with increased degree of undercooling. Moreover for low degree of undercooling crystals change from polyhedral to dendritic when increasing cooling rate. The undercooling, which is defined by Kirkpatrick *et al.* (1981) as the difference between the liquidus temperature and quench temperature, and the cooling rate are parameters relevant for magmatic rocks because of large variations of temperature that occur in nature but it is challenge to extrapolate to fluid-mediated solid state reactions.

An explanation for these textures of rapid growth during metamorphism would be the increasing of the affinity of the reaction by the decreasing the fluid pressure. Numerical studies (Connolly, 1997, 2010; Lasaga, 1989; Miller *et al.*, 2003b; Wang

and Wong, 2003) have shown that a decrease in fluid pressure have the same kinetics effect on the reaction than an increase in temperature. This conclusion is confirmed by an experimental study that shows that the dehydration reactions of gypsum is enhanced when pore fluid pressure decreases at constant confining pressure and temperature (Llana-Fúnez *et al.*, 2012) by increasing the affinity of the reaction, which is defined as the negative difference between the free energy of Gibbs of the products and the reactants and is used to quantify the overstepping of the reaction and its kinetic (Pattison *et al.*, 2011) in an equivalent way of the degree of undercooling defined in magmatic systems. The opposite effect has also been described: a positive difference between pore fluid pressure and confining pressure lead to a decrease in the reaction rate (Hildyard *et al.*, 2011).

Blade-like elongated texture and coarse size of olivine in veins (**Fig.** 22f, **Fig.** 27b, c, e, f) suggest high fluid rock ratios and may indicate rapid, probably focused, fluid flow. Olivines from the core of Jackstraw Ol-Tlc vein in **Figure** 23 that illustrate the change in microstructure from focused fluid flow parallel to the plane of the vein and focused fluid flow along the foliation plane induced by a pressure gradient from the interior of the vein and the reacting serpentinite from the wall rock. Fluid flow in the veins results in a preferential orientation of [010] axes normal to the plane of the vein trend but a random distribution of [100] and [001] axes in this plane (**Fig.** 23a, b). In the transition zone between the Ol-Tlc jackstraw and the serpentinite, prismatic olivine crystals are elongated in the foliation plane defined by antigorite, which is at high angle to the vein orientation (**Fig.** 24a). These olivine crystals have undulose extinction, while those in the vein not. This could be explained also by a focused fluid flow towards the interior of the vein due to the anisotropic permeability of serpentinites (Kawano *et al.*, 2011) leading preferential growth of olivine parallel to the foliation plane. The same CPO/SPO observed in the reacting serpentinite and in veins strongly suggest that in both cases the ultimate cause is due to focused fluid flow. Therefore, it seems that crystallographic relationships between antigorite and olivine may not be due exclusively to topotactic interface-coupled dissolution-precipitation processes (Putnis, 2002; Putnis and Putnis, 2007) but may also be controlled by fluid pressure gradient imposed by changes in permeability.

Because gradient of fluid pressure were presumably lower in the core of the vein (corresponding to jackstraw Ol-Tlc vein), dehydration of antigorite from the wall rock can occur by a decrease in water activity that displace the equilibrium reaction to lower temperatures. The reaction front propagates outwards concomitant to the drainage of fluids produced by the reaction. Therefore, both rapid focused fluid flow and pervasive (but still focussed) fluid flow are combined in this type of composite veins. While this type of outward migration is metasomatic in some cases (such as the one shown in Figure 23) where no talc is produced along the foliation plane of the reaction serpentinite), most reacting zones associated to veining worked as a close system (except for the H_2O component).

Ol (±Tr) veins occurring in the eastern part of the study area however cannot be the results of a reaction in a close system and necessary involve a significant role of oxide components dissolve in the aqueous fluids. These veins have mainly granular morphologies (**Fig.** 27a) and weak CPO (**Fig.** 30 MA17-17). Bucher (1998) has suggested a mechanism of silica solubility and transport in veins crosscutting dolomite marble of Val Malenco, forming olivine and tremolite in veins by diffusion kinetics and surface-reaction kinetics respectively, and the propagation of the reaction front. This process may explain olivine texture of veins and is consistent with rapid fluid flow typical of such vein.

5.1.2. Timing of vein opening and sealing

Dehydration reactions of antigorite at lower temperatures than the equilibrium ones, which are marked in the field by the talc isograd, requires that pathways for fluid migration predate the reaction. The non-compacting scenario described by Connolly (2010) show that fracture-generated porosity may develop above reaction front and could be consistent with our observations. Another explanation for the development of veins given by Bucher (1998) is related with the forces generated in response to the Bergell intrusion. This scenario seems more consistent with our observations as all measured veins were observed only at the vicinity of the intrusion (they were not observed in the eastern part) and have an orientation ~N°70 with nearly vertical dip (**Fig.** 24), which is at high angle to the intrusion contact in this area (**Fig.** 20a). This suggests tangential extensional stresses around the intrusion leading to opening of fractures. Associated radial compressive stresses parallel to vein

orientations and at high angle to the foliation in the serpentinite may have helped compaction during dehydration reactions, explaining the intragranular misorientations in olivine in the reacted rocks. The observation of Ol-veins with conjugate orientations corroborates formation by fracturing of the serpentinite in response to tectonic stresses. Branching veins are observed locally (**Fig.** 22c), but multiple connecting veins in clear tree-root arrangement, as the one described by Plümper *et al.*, (2017), was not observed in the field. These branching veins may have formed by initial connected fractures induced by tectonic and then may have grown with similar process of draining fluids from the wall through the core of the veins.

Once opened, veins may drain fluids from dehydrating serpentinite and allow the propagation of the reaction front. Field (**Fig.** 22e, **Fig.** 23a) and microscopic observation of compacted talc matrix on jackstraw Ol-Tlc vein (**Fig.** 27e) confirm that jackstraw Ol-Tlc veins may have formed before complete dehydration of the serpentinite. Indeed, recent study from Leclère *et al* (2018) has shown that compaction occur at the end of dehydration reactions. This compaction may have therefore deformed the pre-existing jackstraw Ol-Tlc vein leading to deformed talc matrix of metaperidotite and undulose extinction of the big olivine grain from Ol-Tlc vein (**Fig.** 27e).

Veins may also develop during dehydration reactions by hydrofracturing at the microscopic scale: olivine rods composed of connected crystals crosscutting the global orientation of jackstraw olivines with a core free of inclusions are growing normalto the elongation of these veins (**Fig.** 27f) and may be due to fluid drainage as already observed (**Fig.** 22b, **Fig.** 23a, **Fig.** 27a, d).

5.2. Formation of the metaperidotites

Previous section has shown that veins allow rapid extraction of large volume of fluids resulting in jackstraw Ol-Tlc assemblage at lower temperature than equilibrium temperature (**Fig.** 20b, c; **Fig.** 22f; **Fig.** 27b,c) and that both rapid focused fluid flow and slow pervasive fluid flow may occur simultaneously and be combined if the vein remained opened, allowing the propagating of a reaction front into the serpentinite host (**Fig.** 23a). However, only this process may not be responsible of the complete dehydration of antigorite at the km-scale as microstructures resulting from pervasive flow without being associated to veins are the most common observation (**Fig.** 26e,f).

Pervasive fluid flow may occur independently from focused flow depending on the time scale for compaction compare to the time scale of metamorphism (Connolly, 2010). Fluids released by the dehydration of antigorite in nearly static conditions due to the increase in temperature triggered by the Bergell intrusion may have flowed without being channelized if compaction is able to accommodate fluid flux produce by hydration. This would led to reaction kinetics close to equilibrium and the production of olivine + talc (+ tremolite) with a texture apparently controlled by interface-coupled dissolution-precipitation processes. This would be in agreement with the preservation of the former foliation plane in the metaperidotites (**Fig.** 24) and the common occurrences of granular olivines in fine-grained metaperidotite (**Fig.** 26a, b) that do not indicate preferential orientation of fluid flow.

However, elongated olivine in partially reacted serpentinite (**Fig.** 25e,f) and in metaperidotite (**Fig.** 26c-h) are not uncommon and suggest that preferential fluid flow along the former foliation planes could be responsible of the observed CPO. It seems however that metaperidotites records a more complex history reflecting the effect of compaction. The observation of some serrated grain boundaries and abundant inclusions in certain samples of metaperidotite might attest for rapid crystallization due to rapid fluid pulses generated by instabilities during the progression of dehydration reaction and concomitant compaction (**Fig.** 26f), similarly to dendritic overgrowth observed in magmatic olivines (Faure et al., 2003).

A plausible explanation for the association of granular olivines with elongated olivines (**Fig.** 26c, d) would be that elongated olivine with talc have formed rapidly, creating an impermeable layer surrounding remaining antigorite patches. This impermeable layer of prograde minerals may has trapped fluids released from the dehydration of antigorite leading to an local increase of fluid pressure and decrease in the reaction kinetics. Another possible explanation is that granular olivine domains result from grain size reduction of olivine in response to hydrofracturing of the metaperidotite and subsequent annealing, in a process similar to the one described by Padrón-Navarta *et al.* (2010b) in the metaperidotites from Cerro del Almirez.

A remarkable feature of metaperidotites is their relatively homogeneous CPO (with $[010]_{Ol}$ normal to the macroscopic foliation) over hectometric distance. As stated is not necessary explained only to interface-coupled dissolution process but may

have also be controlled by fluid pressure gradient. Indeed, for reactions that produce lower amount of H_2O than those corresponding to the complete antigorite dehydration such as reaction (1) and (2) the resulting CPO is different. Morales *et al* (2018) for instance describe topotactic relationships produced by reaction (1) in other areas of the Malenco unit (far from the Bergell intrusive) with granular porphyroblastic olivines that have $[100]_{Ol}$ roughly parallel to $[001]_{Atg}$. Olivine from samples recoding reaction (2) in the studied area also seems to be in line with the same topotactic relationship (MA16-34, 36, **Fig.** 28).

On the other hand, the anisotropic fluid flow developed during the complete antigorite dehydration (reaction 3) resulted in enhanced anisotropic growth of olivine,with $[010]_{Ol}$ normal to the foliation plane and $[100]_{Ol}$ and $[001]_{Ol}$ randomly oriented in foliation plane (MA16-42,45; MA7-45). A good correlation between $[010]_{Ol}$ and $[001]_{Atg}$ is dominant at the hm-scale of the studied area. The orientation of the maxima $[010]_{Ol}$ (and occasionally $[100]_{Ol}$) is in agreement with the poles of the foliation plane in serpentinites measured in the field outside the isograd (**Fig.** 34).

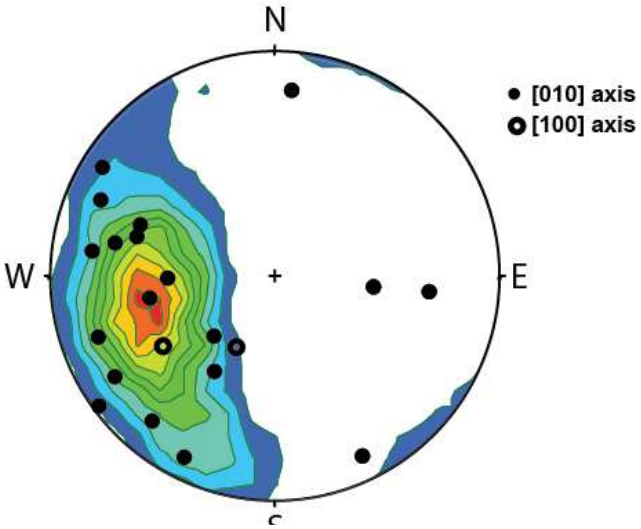

Figure 34 - Stereographic contour plot of pole to foliation planes in serpentinites. Overlying black filled circles are olivine [010] axes and empty dots [100] axes determined by EBSD analyses in the same geographical frame.

5.2.1. Evidence for compaction

Porosity waves have been proposed as an effective mechanism allowing for fast fluid flow through a porous medium (Connolly, 1997, 2010). Their existence is highly dependent on the ability of the solid matrix to deform in cycles of compaction/dilatation. Viscous compaction of the solid matrix during pervasive flow

should be accompanied by a non-hydrostatic stress field at the grain scale. It might be recorded by changes in the microstructure, such as the bent crystals or in rare cases by shear-sensitive (martensitic) mineral (Chapter five of the present manuscript; Padrón-Navarta *et al.*, 2015). In the present study, the metaperidotites display olivine crystals with undulose extinction (**Fig.** 26d), bent crystals of talc and/or chlorite (**Fig.** 26d, h) and high value of misorientation in olivines (**Fig.** 30b), which may indicate some deformation due to metamorphic compaction. However, finite strain was limited as fragile structure such as serrated overgrowths in olivine (**Fig.** 26f, h) are commonly preserved. In part this could explained by compaction mainly accommodated by the deformation of the talc, which is the rheologically softest phase in the assemblage (**Fig.** 26d, h; **Fig.** 27e).

6. CONCLUSION

Field structures, such as the Ol(±Tr±Tlc) veins in the serpentinites and the foliation of the metaperidotites, as well as microstructures and textures of the reacted rocks, record different aspects of the interactions between fluid flow and dehydration reactions in serpentinites from Val Malenco. Veins have allowed rapid focused flow of fluids, lowering the fluid pressure and allowing for dehydration reactions to occur at lower temperature. This process has also resulting in rapid crystallization of olivine texture followed by crystal growth under high fluid rock ratios, evidenced by their jackstraw textures. While open, some veins drained fluids produced by antigorite dehydration induced by the decrease of water activity caused by fluid pressure gradients between the interior of the vein and the wall rock. This leads the propagation of a reaction front outward of the vein. These reaction fronts are characterized by olivines elongated and flattened parallel to the plane of the vein. These olivines are unrelated to the foliation of the serpentinites from the wall rock but are related to the vein orientation, suggesting that their development was controlled by fluid pressure gradient. In the wider veins, which probably functioned for longer times, dissolution and transport of SiO_2 and CO_2 have also occurred during this process.

Pervasive flow may have occurred independently from veins producing foliated metaperidotites. The shape and crystal preferred orientation of olivine in the

metaperidotites could be inherited from the foliation of the serpentinite, via epitaxial growth, or due to enhanced flow parallel to the foliation of the former serpentinite. This would explain the same CPO observed in veins and in metaperidotites when compared the structural plane of maximum focused fluid flow. Moreover, metamorphic compaction driving fluid flow may have slightly deformed metaperidotites as evidenced by both misorientation of olivine, bended crystals of talc and chlorite and the preservation of fragile structure such as serrate grain boundaries. Both focused flow through the veins and pervasive flow in foliated metaperidotites may have occurred simultaneously and independently.

Figure 35 summarizes our interpretation of the history of Val Malenco, during which serpentinites were transformed to metaperidotites. Uplift of Bergell intrusion opened fractures normal to the intrusion. Then, the temperature increase led to the beginning of dehydration of antigorite, releasing fluids both through the fractures and parallel to foliation plane of antigorite. The transformation of antigorite to olivine, talc, and tremolite produced metamorphic veins when fluid are focused through fractures and foliated metaperidotites in the case of pervasive flow parallel to former foliation planes. When veins remained opened for a certain period of time a reaction front developed outward, until the central vein were sealed by the precipitation of minerals or by compaction. At the same time, pervasive flow occurred independently allowing transformation of foliated antigorite to foliated metaperidotite by propagating reaction front with metamorphic compaction. The enlargement of the aureole depend on the time during which temperature is high enough to allow dehydration reactions and fluid migration to occur, which is supposed to be approximately 0.6 Ma according to Trommsdorff & Connolly (1996). Fluids are supposed to finally migrate upward according to previous studies on the geometry of fluid flow in contact metamorphism (Ferry et al. 1998) and devolatilization reactions (Connolly, 2010).

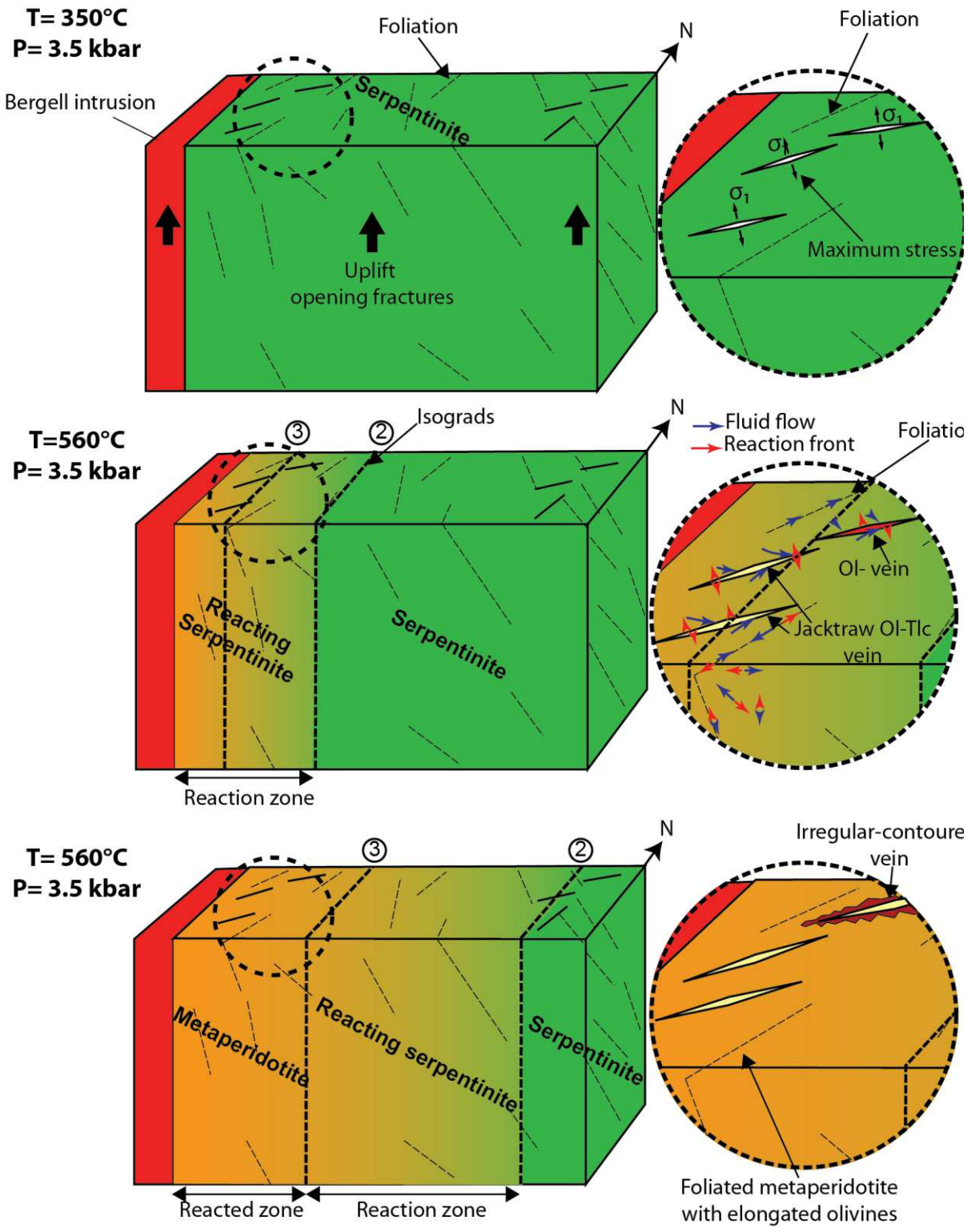

Figure 35 - Sketches summarizing the different step of dehydration reactions, fluid flow and propagation of reaction front consecutive to the Bergell intrusion in Val Malenco.

CHAPITRE IV

MIGRATION DE FLUIDES DES SERPENTINITES DÉSHYDRATÉES EXPÉRIMENTALEMENT

IV. MIGRATION DE FLUIDES DES SERPENTINITES DÉSHYDRATÉES EXPÉRIMENTALEMENT

1. INTRODUCTION

Antigorite is a variety of serpentine (layered silicate), which can contain up to 11-13 wt% H_2O (e.g., Ulmer and Trommsdorff 1995). During slab subduction and related increase of temperature and pressure, its destabilization releases large amount of aqueous fluids, generating porosity, and producing serpentinization and melting in the overlying mantle (e.g., (Hyndman and Peacock 2003; Kelemen *et al.*, 2003). Previous experimental studies on antigorite have mainly focused on the kinetics of the serpentinite destabilization reaction (Perrillat et al. 2005; Llana-Fuñez et al. 2007; Eggler and Ehmann 2010; Gualtieri et al. 2012; Llana-Fúnez et al. 2012; Trittschack et al. 2012; Trittschack and Grobéty 2013), the rheological behavior of serpentinites (Raleigh and Paterson 1965; Rutter and Brodie 1988; Llana-Fuñez et al. 2007; Arkwright et al. 2008; Rutter et al. 2009; Chernak and Hirth 2010; Amiguet et al. 2014; Auzende et al. 2015) and on the potential for triggering intermediate depth earthquakes by fluid release (Raleigh and Paterson 1965; Hilairet et al. 2007; Gasc et al. 2011; Proctor and Hirth 2015). However, there is to date, no experimental constrains on the mineral replacement mechanisms and how fluid flow during dehydration reactions might influence control the microstructure of product phases.

Dehydration reactions of serpentine create up to ~25 vol.% porosity (Rutter and Brodie 1995). The released fluids are expected to flow pervasively around the neo-formed minerals, but can also be focused along preferential planes such as fractures (Ague 2013). In a dense but porous media, fluid flow may also take the form of porosity waves, which result in an efficient drainage of the system (Connolly, 1997, 2010). Numerical simulations (Lasaga 1989; Miller et al. 2003; Wang and Wong 2003) have shown that decreasing pore fluid pressure may increase the kinetics of dehydration reaction by increasing the affinity of the reaction. Experiments from Wang and Wong (2003) show complete dehydration of gypsum within 120 min with confining pressure of 110 MPa and pore pressure of 10 MPa whereas under a confining pressure of 150 MPa and a pore pressure of 100 MPa, dehydration is not completed after more than 300 min. Similar results were also obtained by Llana-Fuñez et al. (2012) where the duration required for a complete dehydration of

gypsum at 120 °C is reduced from more than 26 h to 1.5 h if the buildup pressure (81 MPa) is released (Llana-Fúñez et al. 2012; Bedford et al. 2017; Leclère et al. 2018). At 3.2 GPa and 600 °C, dehydration of antigorite is completed within 4 h when the system is drained (Perrillat et al. 2005) whereas complete dehydration of antigorite requires more than a week under undrained conditions (Eggler and Ehmann 2010).

Since metamorphic textures depend on growth rates of neo-formed minerals and fluid-rock ratios (Padrón-Navarta et al. 2011), the textures of the products of dehydration reactions may record variations of the reaction rates and, by consequence, catch the mechanisms by which fluid migrate. As an example, Padrón-Navarta et al. (2011) have suggested that spinifex texture (characterized by highly elongated tabular olivine crystals with high aspect ratios >5) is indicative of sudden focused fluid migration due to hydrofracturing, whereas granular textures (granofels) results from pervasive fluid migration at metamorphic compaction rates.

The aim of this study is to identify the potential correlation between aqueous fluid flow mechanisms and the initial reacting rock texture by performing drained dehydration experiments at high temperature (730 °C) and moderate pressure (0.3 GPa), followed by careful microstructural and chemical characterization of the products of the antigorite dehydration.

2. MATERIALS AND METHODS

2.1. Starting material

We used two serpentinite samples, one from Val Malenco in Italy (MA16-17 used for the experiment MCS5) and one from Cerro del Almirez massif in Spain (Al16-17# used for both experiments MCS6 and MCS7). The serpentinite samples were selected for their specific natural microstructures. The serpentinites from Val Malenco are known for their well-developed deformed texture, but here, we have selected a weakly-foliated aggregate. To the contrary, the selected serpentinite sample from Cerro del Almirez massif is strongly foliated. Consequently, serpentinite cylinders were drilled in three different orientations: (i) a random orientation in the weakly-foliated Val Malenco serpentinite (MCS5) (ii) normal to the foliation plane (MCS6), and (iii) parallel to the foliation plane (MCS7) for the from Cerro del Almirez

serpentinite. Discs were cut at the end of each serpentinite cylinder as reference material for chemical and microstructural characterization.

The serpentinites from Val Malenco were originally described by Trommsdorff and Evans (1972, 1974), Jung (2004), Morales et al. (2018), and Clément et al. (this thesis, chapter III). Serpentinites from Cerro del Almirez were described by Trommsdorff et al. (1998) and Padrón-Navarta et al. (2008, 2011, 2012). We provide here a brief summary of the main petrological and microstructural features of the serpentinite samples.

2.1.1. Weakly foliated serpentinite from Val Malenco (MA16-17)

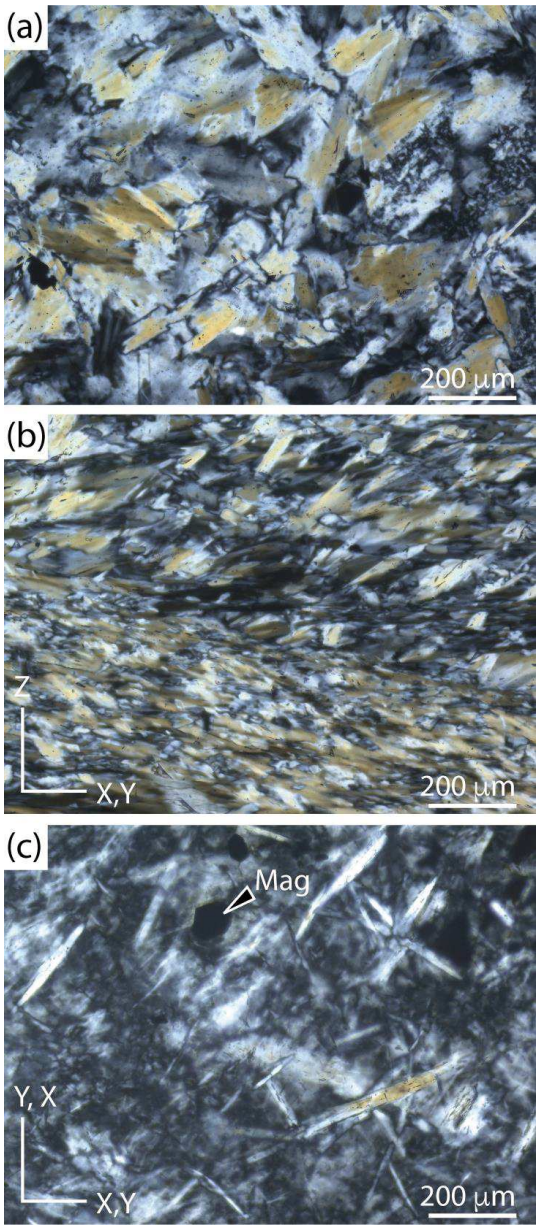

This sample is mostly composed of antigorite (93 %), with minor magnetite (6 %) and rare isolated porphyroblastic olivines (<1%), the later resulting from the destabilization of former brucite (e.g., Atg + Br = Ol + H_2O). The antigorite texture is dominantly lepidoblastic, but granoblastic grains also occur (30 %). Elongated antigorite grains have lengths ranging from ~10 to > 100 µm and widths between <10 µm and 25 µm, but they do not display a marked shape preferred orientation as displayed in **Figure** 36.

Electron backscatter diffraction (EBSD) analyses of antigorite from this sample confirm that it is poorly oriented with the J-index lower than 2.0 (Clément et al., chapter III, this thesis; NB: J-index of 1 denotes a random orientation, Bunge, 1993). Antigorite crystals have nevertheless a weak crystallographic preferred orientation (CPO) characterized by a weak point maximum of [001], and a wide girdle distribution for [100] and [010] axes (**Fig.** 38). The serpentines cylinder for dehydration experiment has been cored at ca. 40° of the maximum concentration of [001] axes.

Figure 36 - Microsctructure of the starting material used for the experiments (natural serpentinite). (a) Weakly foliated antigorite serpentinite from Val Malenco (MA16-17) cut in a non-structural orientation (b) and (c) are strongly foliated antigorite serpentinite with minor magnetite from Cerro del Almirez (Al16-07#) cut perpendicular (XZ section) and parallel (XY section) to the foliation plane respectively.

Since alumina content affect the temperature of antigorite destabilization (Bromiley and Pawley, 2003; Padrón-Navarta et al. 2013), we give here the bulk rock composition (0.99 wt.% Al_2O_3) and the content from punctual analyses (1.03 wt.% Al_2O_3) based on EDS analyses; the values are reported in Table 1.

2.1.2. Strongly foliated serpentinite from Cerro del Almirez, (Al16-17#)

The selected Cerro del Almirez serpentinite is also composed dominantly of antigorite (94%), discontinuous strings of granular mm-size magnetite (3%) are randomly dispersed on the foliation plane. Olivine and tremolite are also present (<2%). The sample is essentially composed of antigorite blades with elongations ranging from < 20 µm to ~200 µm and widths from ~10 µm to 50 µm, in a interpenetration texture (Wicks and Whittaker, 1977). The antigorite blades mark well the foliation with shape preferred orientation (SPO). EBSD maps (acquired during this study) show that antigorite has a well-developed SPO and CPO. The antigorite [001] axes are concentrated normal to the foliation plane (XZ structural plane in **Figure** 36, while [100] and [010] axes define girdles in the foliation plane (XY plane **Fig.** 36). Note that because there is no a clear maximum in the foliation plane, nor a macroscopic lineation there is no difference between the X and Y structural direction. CPO intensities are high, with J-indexes ranging from 3.46 to 2.81 for this sample.

The bulk rock composition of the selected Cerro del Almirez serpentinite has aluminum content (2.46 wt.% Al_2O_3) higher than other serpentinites (e.g., from Elba Island, 1.41 wt.% Al_2O_3, Viti and Mellini 1998) or the selected sample from Val Malenco. Average composition from mineral analyses yields a slightly higher value of 2.66 wt.% Al_2O_3, which was attributed to Al-Tschermak's substitution (Padrón-Navarta et al. 2013) (Table 1).

Table 1: Antigorite composition from de two types of rock used as starting metiral and the composition of run products post dehydration

Locality	Val Malenco	Cerro del Almirez	Experimental samples								
Samples	MA16-17	Al16-07	MCS5			MCS6			MCS7		
Mineral	Atg	Atg	Ol	Tlc	Chl	Ol	Tlc	Chl	Ol	Tlc	Chl
Wt.% SiO_2	43.91 (0.36)	42.14 (0.51)	42.87 (2.35)	58.23 (3.31)	-	43.13 (0.53)	57.30 (0.57)	15.23 (0.92)	44.84 (0.59)	56.80 (0.93)	--
Al_2O_3	1.03 (0.17)	2.66 (0.26)	3.17 (2.77)	4.23 (3.09)	-	2.36 (0.16)	6.03 (0.45)	42.71 (2.15)	3.05 (0.45)	5.79 (0.55)	-
FeO_T	2.94 (0.20)	3.86 (0.46)	4.12 (0.37)	2.65 (1.57)	-	6.63 (0.38)	3.44 (0.23)	4.65 (0.27)	4.61 (0.28)	2.63 (0.43)	-
MgO	37.66 (0.50)	38.68 (0.34)	49.12 (2.18)	33.91 (2.86)	-	47.86 (0.69)	33.22 (0.33)	37.41 (0.99)	47.51 (0.74)	34.79 (1.30)	-
Fo%			0.97		-	0.93			0.95		
XMg	0.93	0.91	92	0.93	-	88	0.91	0.89	91	0.93	-

2.2. High pressure assembly and dehydration experiments

The serpentinite cylinders have a length of 11 mm and a diameter of 7.8 mm. A vertical central hole of 1 mm of diameter is drilled, in which a porous alumina cylinder (Sintox^{TM} , high purity 99.7% Al_2O_3, with 20 vol. % of interconnected porosity) was inserted as shown in **Fig.** 37.

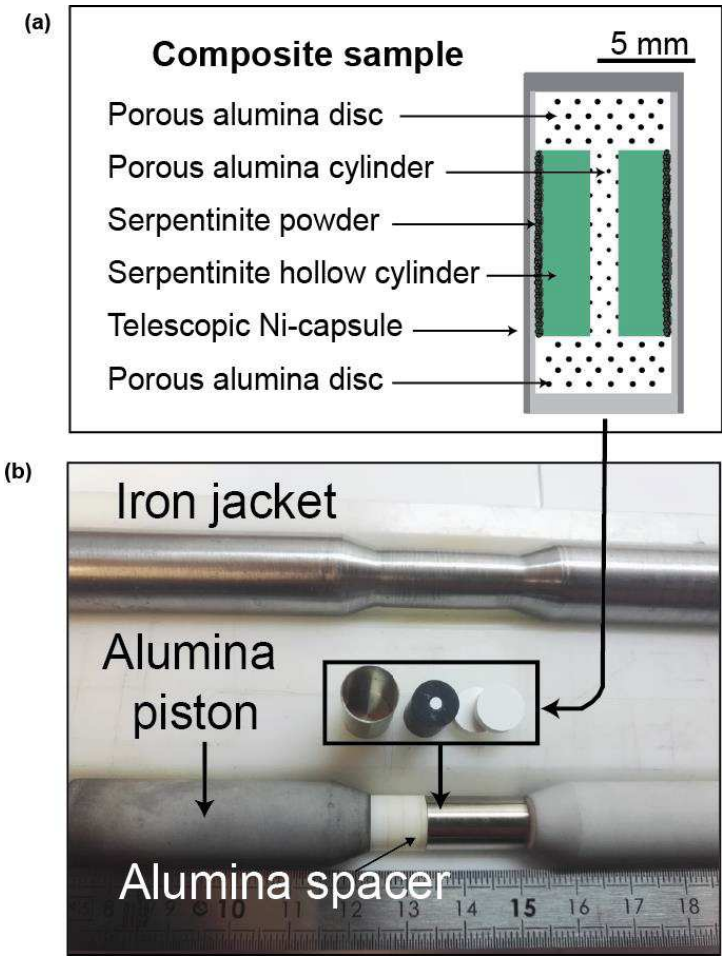

Figure 37 - experimental set up (a) composite sample with the cylinder of serpentinite associated to porous alumina disc and cylinder, all encapsulated in telescopic nickel capsule; (b) high pressure assembly

The central porous alumina cylinder should act as a drain during dehydration of antigorite and therefore should reduce the fluid pressure in the system. It has moreover a high strength (flexural strength of 150 MPa), and does not collapse at run conditions. We added at the top and bottom of the serpentinites cylinder, a 2-mm spacer made of the same porous alumina (20 vol. % of porosity) as reservoirs for the released fluids (**Fig.** 37). The composite sample (serpentinite and porous alumina) is then inserted in a telescopic nickel capsule (as in Chen et al., 2006). The nickel capsules have a length of 17.76 mm, with an outer diameter of 10 mm and wall thickness of 0.35 mm. The used of nickel was chosen in an attempt to impose a fixed oxygen fugacity (at upper mantle level, McCammon, 2005) during dehydration, even if at 730 °C and for centimetric-scale sample, the oxygen fugacity is not homogeneous (Faul et al. 2018). Powder from hand-crushed serpentinites was used to fill up potential empty spaces between the capsule wall and serpentinite cylinder (**Fig.** 37). Marks were made on both the reference material disc and the cylinder to retrieve the initial orientation of the sample (**Fig.** 37). Subsequently, the telescopic nickel capsules were encapsulated in iron-

jackets along with zirconia pistons, alumina pistons, and alumina spacers (Fig 1a) as in Demouchy (2010) or Mei & Kohlstedt (2000).

The dehydration experiments are performed using a gas-medium high pressure high temperature vessel (Paterson 1990) in static condition. Argon is used as a pressure medium, generating an initial isostatic system. The vessel is internally heated with a house-made furnace, calibrated prior the dehydration experiments (see Chapter II), to characterize and minimize the thermal gradient along the centimetric serpentinites sample. The annealing temperature is 730°C, 170°C above the equilibrium temperature of antigorite breakdown at 300 MPa (Padrón-Navarta et al. 2012; 2015). Such high overstep in temperature was chosen to enhance dehydration rate and to keep annealing duration within a 1-day experiment frame.

The high pressure assemblage was then pressurized at ambient temperature up to 110 MPa. Then, the temperature was increased with a rate of ~8 °C/min to 730 °C. Once this temperature was reached, pressure was rapidly increased up to 300 MPa. The increase of temperature and pressure roughly followed the water isochore of 30 cm^3/mol to avoid important volume changes and rupture of the capsule during temperature increase. Temperature and pressure were kept stable for 10 hours. No axial compression was applied during the experiment. Then, the sample were quenched by decreasing temperature at a rate of ~80 °C/min and the pressure was released following approximately the water isochore of 15 cm^3/mol.

2.3. Scanning electron microscopy and electron backscattered diffraction

Thin sections were cut parallel and normal to the elongation of the recovered composite sample. They were polished with diamond paste and a finishing stage of polishing using colloidal silica (0.04 µm particles) in a vibrometer for 4 hours. The microstructures were imaged by a field emission scanning electron microscopy (SEM FEI Quanta 200 FEG) with an accelerating voltage of 10 kV. Quantitative estimation of the porosity of the starting material and run products was performed with imageJ software on the acquired SEM images. CPO of antigorite and olivine were measured by EBSD using a Camscan Crystal Probe XF500 equipped with an EBSD HKL NordlysNano detector at Géosciences Montpellier (France). We acquired EBSD maps with a resolution of up to 300 nm over areas of 240 x 200 µm. Binning mode was set to 4 x 4, time exposure to 24 ms, and accelerating voltage to 20 kV. Mineral

phase orientation based on Kikuchi patterns was successful for olivine and antigorite, but talc crystallographic orientations could not be measured due to poor polishing of this phase. Nevertheless, the Si-rich phase was occasionally indexed as talc. EBSD data were treated with MTEX, a MATLAB toolbox for texture analysis (Hielscher and Schaeben 2008; Bachmann et al. 2010; Mainprice et al. 2014). Grain detection was performed with a threshold misorientation angle of 10°. Grains ≤ 2 pixels were removed from data set. Oriented distribution functions were calculated using a "de la Vallée poussin" kernel with a constant halfwidth of 10°. Average crystallographic orientations of the olivine and antigorite grains are presented as pole figures.

2.4. Chemical analyses

The chemical composition was determined semi-quantitatively by energy dispersive spectroscopy (EDS) using a SEM FEI Quanta 200 FEG, with an accelerating voltage of 10 kV, at Université de Montpellier (France). Run products were further identified with conventional X-ray powder diffraction.

3. RESULTS

After only 10 h at 730°C and 300 MPa, under drained conditions, the dehydration of the randomly oriented and foliated serpentinites has successfully occurred. The run products are large enough to be identified even at the optical microscope and they are identical for the three experiments: olivine + talc + minor chlorite, and thus water. However, the resulting microstructures differ depending on the initial fabrics and the observed structural plane (i.e. normal or perpendicular to the former antigorite foliation). We present the experiment one by one below.

3.1. Serpentinite with weak CPO (run MCS5)

Run products resulting from serpentinite dehydration are olivine and talc. Typical microstructures are shown on **Figure** 38a. Olivine is mostly elongated, with acicular to tabular shapes (<5 µm to ~20 µm in length) and in minor amount occurs in rounded shapes (< 10 µm size). They are randomly distributed. Talc is randomly associated to olivine and randomly oriented as well. Apparent porosity has dramatically increases (30 %) compare to the starting material (1.5 %, Fig 3a). EBSD maps show that neo-formed olivine have a weak CPO (with a J-index of only 1.23), where $[010]_{Ol}$ axes are roughly parallel to $[001]_{Atg}$ axes from the starting material (**Fig.**

39a). We have further characterized the microstructures at the vicinity of the end of the central porous alumina. Here the texture is characterized by randomly elongated acicular olivine of less than 5 µm and up to 20 µm in length. Moreover, at few µm from the porous alumina, spherical nano-scale olivines (~ 200-400 nm) are visible (**Fig.** 40a).

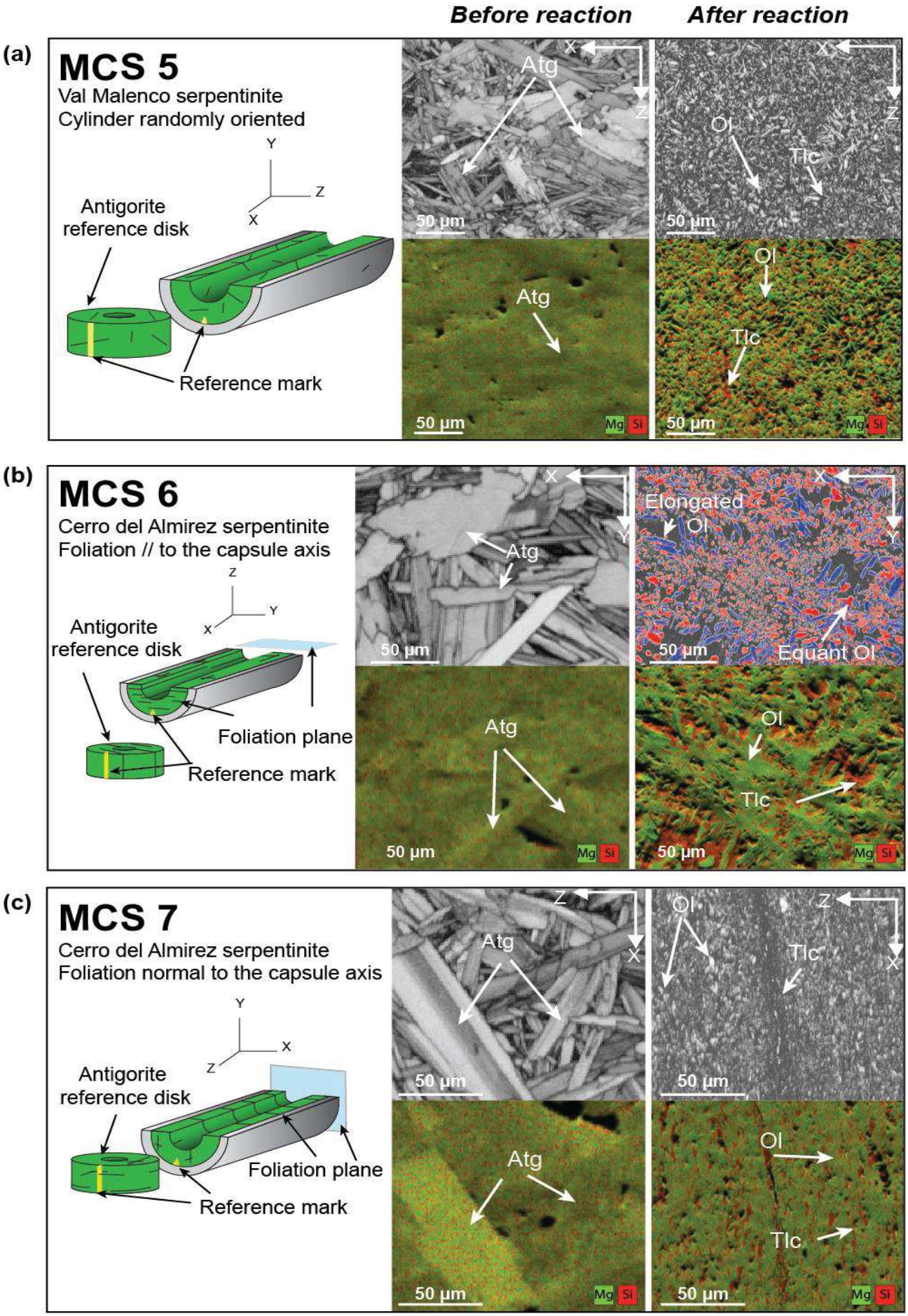

Figure 38 - Back-scattered electron microphotographs and chemical maps of the starting material and run products. (a) MCS5 sample, randomly oriented relative to the elongation of the capsule (b) MCS6 sample, foliation plane parallel to elongation of the capsule. (c) MCS7 sample, foliation plane normal to the elongation of the capsule. Sketches showing orientation of antigorite relative to the elongation of the capsule are added for clarity

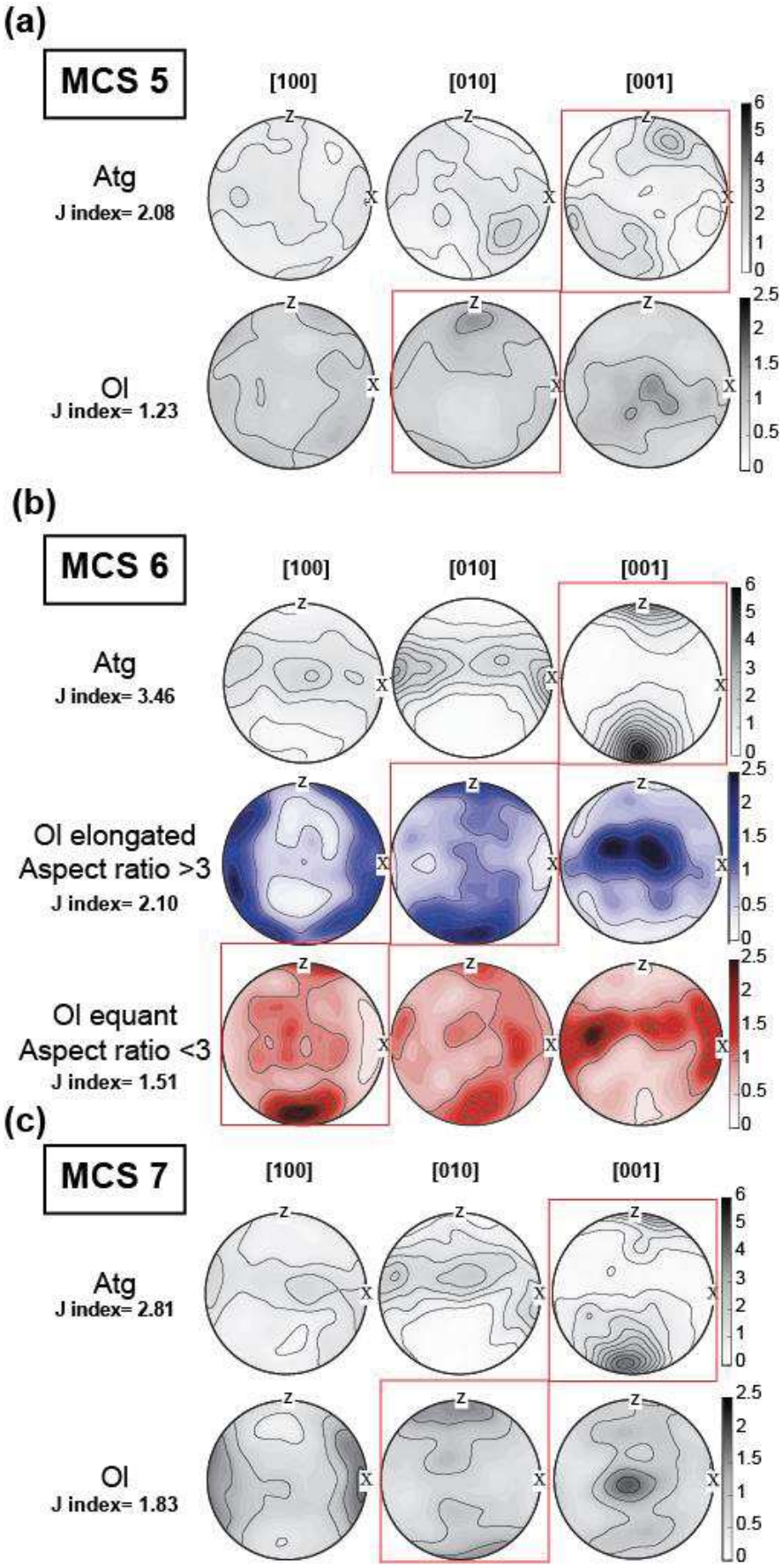

Figure 39 - Crystal preferred orientation of starting material and run products. (a) Pole figures of antigorite and olivines from MCS 5 sample, randomly oriented relative to the elongation of the capsule (b) Pole figures of antigorite and olivines from MCS 6 sample, with foliation plane parallel to elongation of the capsule. (c) Pole figures of antigorite and olivines from MCS 7 sample, with foliation plane normal to elongation of the capsule.

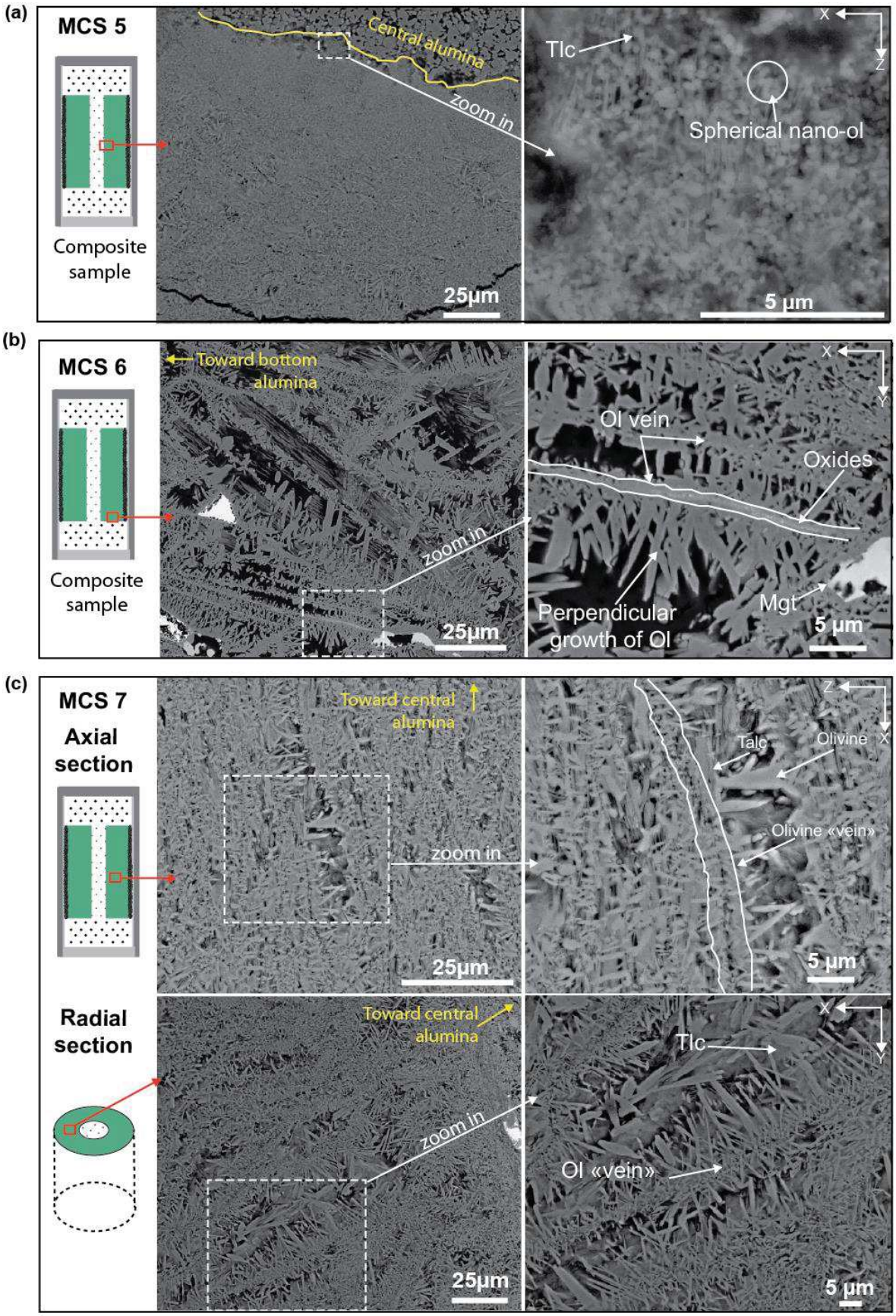

Figure 40 - Back-scattered electron microphotograph of the microstructures of the run products. (a) MCS5 sample, randomly oriented relative to the elongation of the capsule. Some olivines seem to have dendritic texture. At the contact of the drained end, spherical nano-scale olivines are observed. (b) MCS6 sample, foliation plane parallel to elongation of the capsule, showing olivine veins orientated normal to the drained end (central porous alumina). Elongated olivines are growing normal to the elongation of the vein. (c) MCS7 sample, foliation plane normal to the elongation of the capsule, image show a transverse section (parallel to foliation plane) and the position of the drained end. Olivines veins are less visible but still seem oriented normal to the drained end and have elongated texture. The transverse section shows highly similar pattern than in MCS6.

Chemical analyses of the neo-formed minerals confirm that the assemblage produced is olivine and talc. However, composition of olivine is very forsteritic (Fo_{97}), and show a large dispersion in the analyses (1σ=2.18% for MgO and 2.35% for SiO_2) and a high Al content for olivine due to nanoinclusions (3.17 wt.%, Table 1). Talc compositions are unusual with high compositional dispersion of the analyses (1σ= 2.86% for MgO and 3.31% for SiO_2, Table 1) and is likely due to a mix with traces of chlorite (**Fig.** 41).

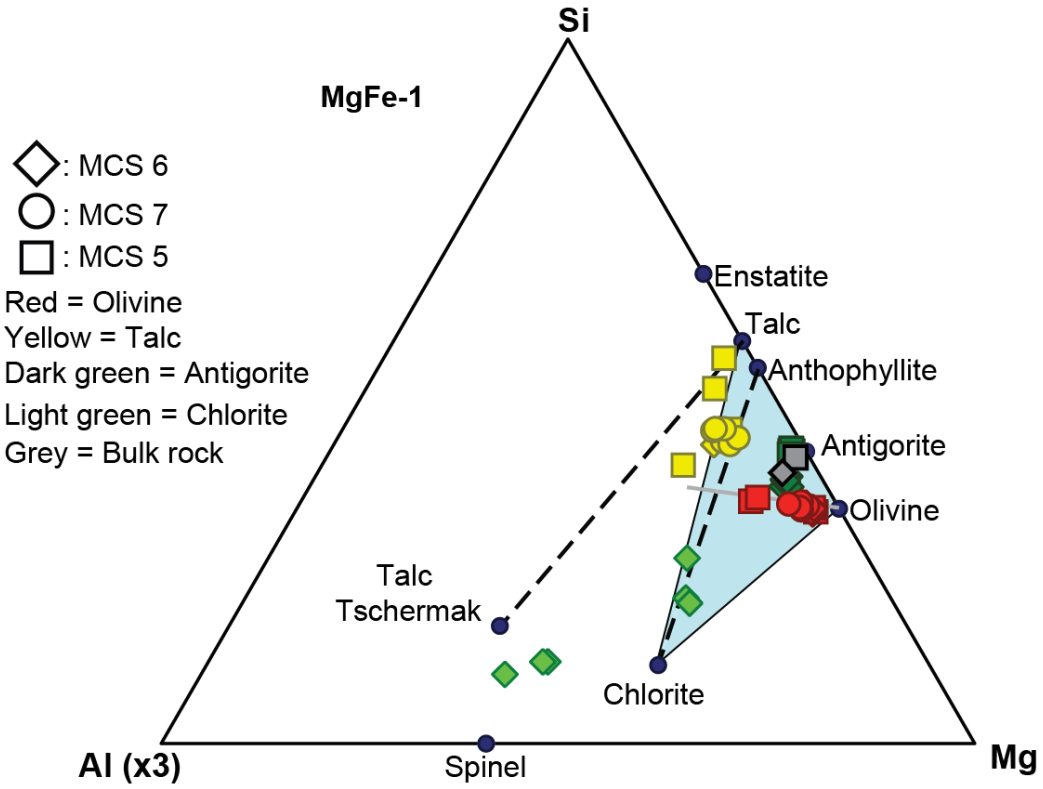

Figure 41 - Ternary MAS diagram projected with Mg-Fe_{-1} vector showing the bulk composition of Val Malenco and Almirez serpentinite in grey, antigorite composition in dark green, olivine composition in red, talc composition in yellow and chlorite composition in light green. Symbols are square for MCS 5, diamond for MCS 6 and circle for MCS 7.

3.2. Foliated serpentinite, sample MCS6

After dehydration of foliated serpentinite (foliation plane parallel to the elongation of the capsule), two populations of olivines are identified based on their aspect ratio, both in the foliation plane: (1) elongated olivine with aspect ratio higher than tree (blue olivine in **Fig.** 38b) with tabular and acicular shape and length between 5-20 µm, and (2) equant and granular olivine with aspect ratio lower than three (red olivines in **Fig.** 38b) and grain size between 5 and 20 µm. The Si-rich phase associated with olivine in **Figure** 38b is talc, which is not preferentially oriented

and well intermixed with olivine. Porosity is estimated to 25 area % and is randomly distributed.

At the vicinity of drained top and bottom porous alumina multiple crack-like structures are visible, occasional filled with oxides. The oxides are unfortunately too small to be analyzed, but they most probably correspond to magnetite as they occur spatially correlated with unreacted magnetite from the starting serpentinite. Olivine in these crack-like structures is elongated in the direction of the center of the crack. Magnetite grains are still present, but appear unstable (reaction rims enriched in Al_2O_3). Magnetite is also commonly fractured with no displacement; fractures are filled with elongated olivine and talc (**Fig.** 38b and 40b).

EBSD analyses of run products show that the elongated olivine (blue in **Fig.** 38b) have a strong CPO with J-index of 2.10 and marked crystallographic relationships with the former antigorite as shown by [010] axes of olivines parallel to [001] axes of antigorite (**Fig.** 39). The [001] axes of olivine also define a maximum in the foliation plane (XY plane in **Figure** 38b) and is correlated with the elongation. This texture is highly similar to the [010]-fiber described by Tommasi et al. (2008), referred also as AG-type olivine texture in the literature (Mainprice, 2007). Equant olivines (red in **Figure** 38b) have also well-developed CPO with a J-index of 1.51, but the crystallographic relationships with antigorite is different, with the [100] axes of olivine parallel to the [001] axes of antigorite as shown in **Figure** 39b. The second population of olivine does not define a lineation (**Fig.** 39b).

Chemical analyses of the minerals produced by dehydration of antigorite confirm that they are olivine + talc + chlorite and then H_2O. Olivine is forsteritic (Fo_{93}), but with an unusual amount of aluminum (2.63 wt%) and silica (43.13 wt%), which are due to high amount of chlorite/talc/spinel inclusions in them. Talc is also Al-rich (6.03 wt% Al_2O_3) and appears to be a mixed with talc and chlorite, as they fall between the pole of talc and the pole of chlorite as shown in **Fig.** 41. Chlorite has also unusual composition with very high amount of Al_2O_3 and very low amount of SiO_2 (42.75 wt% and 15.23 wt%, respectively), which is a mixed composition between spinel and chlorite with high proportion of spinel (Table 1, **Fig.** 41).

3.3. Foliated serpentinite, sample MCS7

After dehydration of foliated serpentinite (foliation plane normal to the elongation of the capsule), only one population of olivines is identified with olivine preferentially elongated and flattened parallel to the foliation plane with tabular or acicular shapes and length of ~10 µm as seen in **Figure** 38c. They display then a strong SPO. Talc crystals are also flattened parallel to foliation plane and intermixed with olivines. Porosity has been estimated to 20 area % (from **Fig.** 38b), thus again higher than in the starting material. Microstructures of run products at the vicinity of the drained central porous alumina show olivine rich layers, from which elongated olivine (~ 5 µm in length) has grown generally perpendicular to the former foliation as shown in **Figure** 40c. Since these olivine rich layers are also visible perpendicular to the foliation plane, they are located in planar structures rather than in channels. A transverse section of MCS7 was cut (i.e., parallel to foliation plane) and show similar microstructures than in the same equivalent section of MCS6, that is the olivine rich structures oriented toward the drained portion of the capsule (central, top and bottom porous alumina).

EBSD analyses of run products show that the olivines elongated parallel to the former foliation plane have a CPO with J-index of 1.83 and a crystallographic relationships with antigorite illustrated by the [010] axes of olivine parallel to the [001] axes of antigorite, both being normal to foliation plane as for MCS 6 (**Fig.** 39). The [001] axes define a weak maximum on the foliation plane although this depends on the surface map considered; other EBSD maps in the same section suggest that the distribution of [001] is closer to a girdle in the former foliation plane (**Fig.** 39c). The chemical compositions of run products minerals are identical to MCS6.

4. DISCUSSION

4.1. Fluid drainage and dehydration kinetics

At the experimental conditions (730 °C and 300 MPa), the dehydration reaction was not expected to be total. Moreover the equilibrium run products in undrained conditions are olivine + enstatite + chlorite + H_2O (Trommsdorff and Evans 1972). However, in drained conditions, the reaction is complete within 10 hours and antigorite destabilization yields well-grown talc crystal as the silica-rich phase. An explanation for the observed metastable assemblage at the experimental conditions

would be that dehydration of antigorite producing olivine + talc + chlorite + H_2O occurred very early during the experiment close to the equilibrium temperature (560 °C, 300 MPa), and have been completed very rapidly.

Experimental dehydration of antigorite at high pressure resulting in olivine + enstatite + H_2O under undrained conditions (e.g., in piston-cylinder experiments) allows to estimate the minimum time (t, in seconds) required to complete dehydration reaction according the formulae from Eggler and Ehmann (2010):

$$t = \frac{r\ F_r}{K_r\ A_\theta^\circ \left[-171\left(1-\frac{T_{eq}}{T}\right)\right]} \quad (1)$$

where, r is the density/molecular weight (2.54/4536 in mol/cm^3) which is a scaling factor to transform the reaction progress (F_r) into conventional reaction rates in mol/cm^3, F_r is the dimensionless reaction progress, K_r is rate constant (-9.2x10^{-16} mol/cm^2/s), A_θ^0 the initial specific surface area of antigorite (assumed to be equal to the experimental work, 79300 cm^2/cm$^3_{rock}$), T_{eq} is equilibrium temperature and T is temperature of dehydration, both in K. The reaction progress is a function of the progress of the reaction (F = 1, for a fully reacted case) and a shape factor depending of the geometry of the reactant antigorite (here assumed as prisms). From Eq. (1), a duration of 7 days is required to completely dehydrate a serpentinite under undrained conditions with an overstep in temperature of 170 °C. Thus, our experiments confirm the results from previous experimental studies, which have reported significant enhancement of reaction kinetics in drained system for serpentinites and gypsum (Perrillat et al. 2005; Llana-Fúnez et al. 2012; Leclère et al. 2018).

It has been recently shown (Leclère et al. 2018; Bedford et al. 2018) that compaction during dehydration might reduce porosity therefore controlling the velocity of propagation of reaction front. A decrease of porosity may then lead to an increase in the pore fluid pressure and thus a reduction of the reaction rate. We infer therefore, that compaction was negligible during the course of our experiments, which is in agreement with the preserved high porosity of the run products (from 20% to 30% in **Fig.** 38) and macroscopic preservation of the shape and dimension of the serpentine cylinders after the experiments.

Similar results of dehydration of serpentine without collapsing of pore space has been observed with effective pressure of up to 80 MPa (Llana-Fuñez et al. 2007). Combination of temperature overstepping and pore fluid decreasing (not quantified) with no compaction may therefore have allowed ultrafast dehydration of antigorite into olivine + talc + H_2O with a total fluid migration within short a time and thus preventing the reequilibration of the system toward olivine + enstatite assemblage.

4.2. Fluid flow anisotropy

Since temperature distribution was almost homogeneous along the serpentinite cylinders and because both SPO and CPO of run products are observed, temperature overstepping due to fluid drainage may have dominantly controlled the texture of the run products. Drained conditions imposed by porous alumina induced a decrease of fluid pressure, while confining pressure remained constant leading to faster reaction rates than in the hydrostatic systems. Here, fluid flow may have been controlled and enhanced by the presence of foliation plane from the starting serpentinite. The striking observation that olivine is elongated on the foliation plane (**Fig.** 38c; **Fig.** 39c; **Fig.** 40c) but have variable length and random orientation of its long axes in the foliation plane (**Fig.** 38b; **Fig.** 39b; **Fig.** 40b) suggest preferential flow parallel to the former foliation plane resulting in an abnormal fast-growth of [001] axes of olivine. Moreover, it indicates that the flow direction was not focused in a particular direction in the foliation plane but was most probably distributed and controlled by the details of permeability and the distance to the porous alumina (**Fig.** 38a,b; **Fig.** 39a,b; **Fig.** 40a,b). Higher fluid flow parallel to foliation plane than normal to it has been experimentally demonstrated by Kawano *et al* (2011). However, permeability of dehydrating serpentinites may also vary locally during the course of dehydration changing locally reaction rate.

In poorly foliated sample MCS5, similar process may have occurred as elongated olivine with random orientation and variable length of the elongation are also observed (**Fig.** 38a; **Fig.** 40a) but with less intensity due to less anisotropic flow than in initially strongly-foliated serpentinites.

Observed granular equant olivines (**Fig.** 38) might correspond to the initial stages of crystallization. An example of the very first step of crystallization would be the spherical nano-scale olivine located at the contact with of central porous alumina (**Fig.** 40a) which are growing to form the granular olivines, which become progressively elongated as they undergo fluid flow gradient during dehydration reactions.

Crystallographic relationships observed between antigorite and olivine (**Fig.** 39) have already been described (Boudier et al. 2010; Padrón-Navarta et al. 2015; Morales et al. 2018) and might be attributed to interface-coupled precipitation-dissolution mechanisms of parent phase (Putnis 2002; Putnis and Putnis 2007). We inferred however that this crystallographic relationship could be a consequence of focused fluid flow imposed by anisotropic fluid pressure gradient controlled by the orientation of antigorite (i.e., the foliation). We conclude that crystallographic relationship between parent and product phases it is ultimately controlled by the permeability imposed by the starting material rather than a simple transfer of parent crystal lattice. This is corroborated by the significant change in grain size of the dehydration products compared to the initial size of the antigorite crystals.

Other topotaxial relationships between antigorite and olivine have been reported in experimentally undrained dehydrated serpentinite in piston cylinder apparatus (Padrón-Navarta et al. 2015) and in partially dehydrated serpentinites (Nogaya et al. 2014; Morales et al. 2018). In this case the correlation with [001] axes of antigorite being parallel to [100] axes olivine as observed for the low aspect ratio olivine in the foliation plane (**Fig.** 39b) would indicate that limited fluid flow corresponding to undrained conditions or minor fluid released associated to partial (brucite) dehydration resulting in olivine porphyroblasts prevent anisotropic grain growth. Alternatively focused fluid flow would indirectly favor the other topotactic relationship $[010]_{Ol}//[001]_{Atg}$ by promoting olivine grain growth parallel to [001] along the fluid flow direction. Such change was most likely indirectly controlled by the orientation of (001) antigorite planes in the former serpentinite.

4.3. Similarities with natural observations

The crack-like network observed close to the draining part of the capsule suggests that brittle deformation occurred at the initial stages of dehydration. This in

line with the recent modeling by Okamoto et al. (2017) that shows the development of interconnected cracks during dehydration in order to accommodate fast volumetric changes. Static and differential stress conditions control the geometry of the crack network (either parallel or perpendicular to the initial foliation) thus modifying the anisotropy of permeability during reaction (Okamoto et al. 2017). Our experimental observations suggest a clear geometric arrangement between the growth of elongated olivines and the development of the initial crack network. This would allow a rapid drainage of fluids through the interior or the initial crack that promotes a fluid pressure gradient with respect of the interior (unreacted) domains. This is in agreement with the smaller olivine grain size marking the position of the initial crack network (high nucleation rate) compare to the interior where grain growth dominates over nucleation. The increase of olivine grain size and elongation toward the exterior of the initial crack network suggest an outward growth of the reaction products (i.e. in opposite direction of fluid flow) under lower reaction affinity.

Olivine morphology observed on planes where natural focused fluid flow has been inferred in Val Malenco show striking similarities with our experimental results. The microstructure observed in the former foliation plane of the serpentinite (**Fig.** 42a) would be equivalent to the jackstraw Ol-Tlc (described in detailed in Chapter III) and shown in **Figure** 42b. These natural veins show elongated and minor granular olivine of cm-scale randomly oriented on the plane of the vein. **Figure** 42 shows that the distribution of olivine long-axis orientation is roughly the same between experimental and natural sample and it is randomly distributed on the plane containing the focused fluid flow. The random orientation of the SPO and CPO (girdle distribution of [001] olivine axes) would imply that the direction of fluid flow in that plane was not strongly oriented.

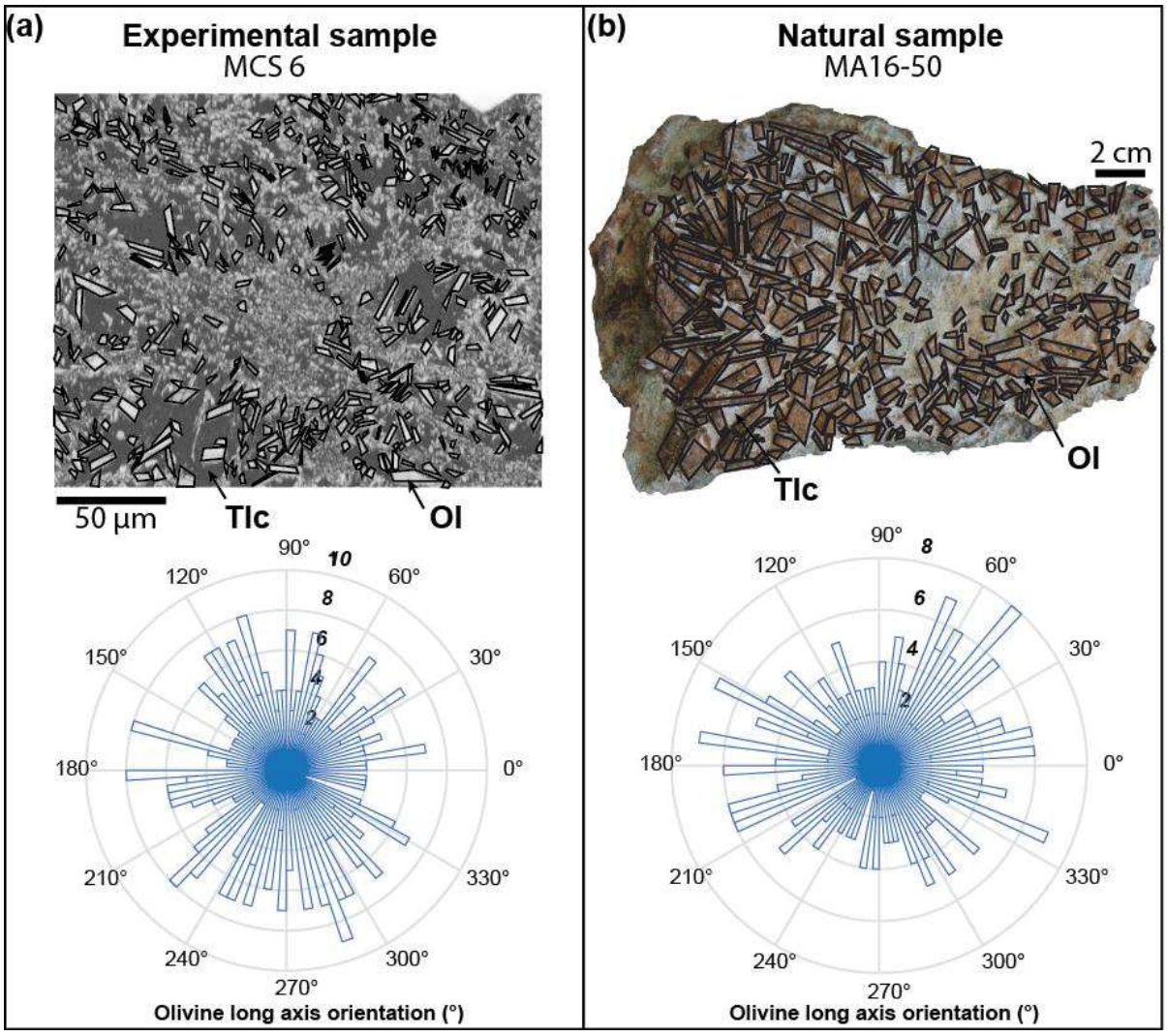

Figure 42 - Rose diagram of (a) olivine from experimental sample MCS6 from this study, and (b) jackstraw olivine in Ol-Tlc vein from Val Malenco (this thesis, chapter III).

5. CONCLUSIONS

Dehydration of antigorite under high temperature overstepping and high fluid pore pressure has triggered fast antigorite transformation to olivine and talc. We infer that small granular olivine with low aspect ratio initially crystallized with topotactic relationship $[100]_{Ol}//[001]_{Atg}$. Flow gradient however enhanced parallel flow on foliation plane and toward the interior or an initial crack network resulting in a change in the olivine SPO and CPO. Anisotropic fluid flow produces elongated flattened olivine parallel to the plane of fluid flow, with fast-growing [001] axes elongated in the flow direction. We infer that pure topotaxial crystallographic relationship between

antigorite and olivine is rather a consequence of focused fluid induced by anisotropy in permeability. Local permeability variation may have occurred by the development of a crack network system, which can still be recognized in the dehydrated products. These cracks, which look like “veins” in quenched samples, may have connected with each other during the progress of the reaction and have led to a significant drop of fluid pressure once connected to the drained end of the capsule resulting in a fast kinetics of the reactions. The experimental results from this study have important implications for constraining the fluid flow in natural systems by using the anisotropic growth of olivine as a marker vector for fluid direction.

CHAPITRE V

COMPACTION METAMORPHIQUE ET MIGRATION DE FLUIDES

ARTICLE PUBLIÉ

Non-hydrostatic stress field orientation inferred from orthopyroxene (Pbca) to low-clinoenstatite (P21/c) inversion in partially dehydrated serpentinites

ABSTRACT

The direction of the main compressional stress, at the origin of the orthoenstatite (Oen) inversion to low-clinoenstatite (LCen) lamellae observed in partially dehydrated antigorite-serpentinites, has been inferred based on the crystallographic orientation relationship between Oen host crystals and the LCen lamellae by means of electron backscattered diffraction (EBSD) combined with optical microscopy. This technique was applied to two samples: a transitional lithology (Atg-Chl-Ol-Opx) and a metaperidotite (Chl-Ol-Opx), both collected within 3 m from the serpentinite dehydration front exposed in Cerro del Almirez (Betic cordillera, South Spain). The metaperidotite displays a clear crystal-preferred orientation (CPO) of both Oen and LCen. The transitional lithology shows weaker CPOs. The meta- peridotite contains LCen crystals representative of two possible variants of the Oen to LCen martensitic transformation with distinct orientations, which are consistent with a unique compression direction at ca. 45° to the normal to the foliation and to the lineation of the precursor serpentinite. In contrast, in the transitional sample, calculated compressional stresses display an almost random orientation. The observation of such a variation in the stress field recorded by two samples separated by <3 m rules out a tectonic origin for the stresses producing the LCen in these metaperidotites. We interpret therefore these stresses as resulting from compaction during dehydration. The present analysis implies that compaction-related stresses, though variable at the meter scale, may be organized at the centimeter scale during dehydration reactions of serpentinite.

V. COMPACTION MÉTAMORPHIQUE ET MIGRATION DE FLUIDES

1. INTRODUCTION

Experimental work (Sclar et al. 1964; Boyd and England 1965; Grover 1972; Yamamoto and Akimoto 1977; Khodyrev and Agoshkov 1986; Angel et al. 1992; Wunder and Schreyer 1992, 1997; Luth 1995; Ulmer and Stalder 2001; Jahn and Martoňák 2009) provides evidence for the existence of several polymorphs of enstatite $MgSiO_3$ (**Fig.** 1): protoenstatite with a space group (*Pbcn*), orthoenstatite *Pbca* (Oen), a high-pressure clinoenstatite *C2/c* (HCen), a low-pressure high-temperature clinoenstatite *C2/c*, and a low pressure and low temperature clinoenstatite with a space group $P2_1/c$ (LCen). More recently, Zhang *et al.* (2012) discovered a second high-pressure clinoenstatite with the space group $P2_1/c$. Enstatite occurs in mantle and crustal rocks almost exclusively in the Oen form. LCen is known to occur in stony meteorites for some time, but its occurrence on Earth was not reported until the work of Dallwitz et al. (1966). Most terrestrial descriptions are related to volcanic rocks, which contain multiply twinned LCen (Dallwitz et al. 1966; Dietrich et al. 1978; Komatsu 1980; Shiraki et al. 1980; Yasuda et al. 1983). A minor proportion of described LCen crystals has a metamorphic or a deformational origin; these crystals are typically untwinned (Trommsdorff et al. 1968; Frost et al. 1978; Bozhilov et al. 1999; Ruiz Cruz et al. 1999; Padrón-Navarta et al. 2015; Zhang et al. 2017) . Twinned LCen in meteorites and in terrestrial rocks were interpreted to form by cooling from protoenstatite (Brown and Smith 1963; Boyd and England 1965; Yasuda et al. 1983), whereas untwinned LCen is interpreted to form by martensitic transformation from Oen due to shear on (100) planes in the [001] direction (Turner et al. 1960; Coe 1970; Raleigh et al. 1971; Coe and Muller 1973; Coe and Kirby 1975; Frost et al. 1978). Clinoenstatite with a space group $P2_1/c$ has also been described in peridotites from presumed ultra-high pressure origin such as Alpe Arami (Bozhilov et al. 1999), Dabie-Sulu garnet pyroxenites (Zhang et al. 2002), Indus ophiolite (Das et al. 2015) and in the Luobusa ophiolite (Zhang et al. 2017). In these cases, the occurrence of LCen was interpreted as the result of decompression from the stability field of HCen with a space group *C2/c* (**Fig.** 43), implying exposure of

these rocks to ultrahigh pressures >10 GPa corresponding to more than 300 km depth, although a martensitic transformation from Oen can not be discarded.

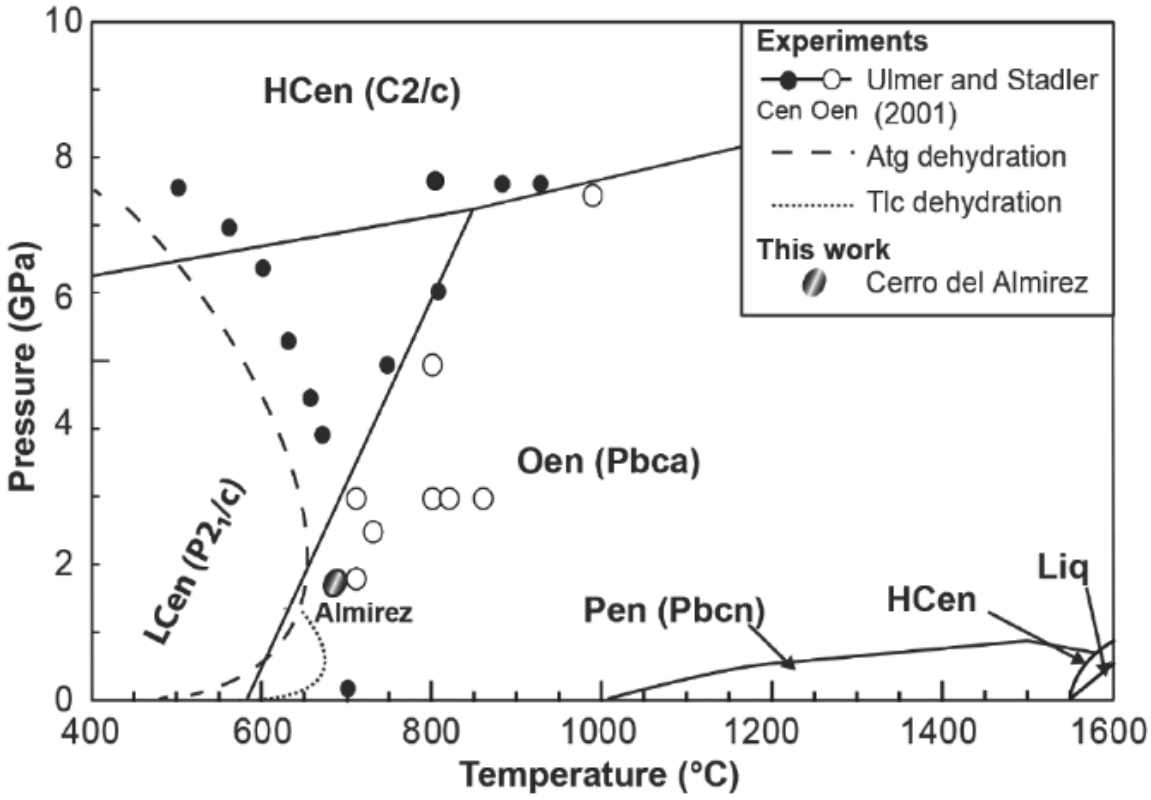

Figure 43 - Phase diagram of enstatite (modified from Ulmer and Stadler, 2001 and Gasparik (2014)). HCen refers to High-clinoenstatite, LCen to Low-clinoenstatite, Pen to protoenstatite and Oen to orthoenstatite. Dehydration conditions in the Cerro del Almirez serpentinite-metaperidote body (Padron-Navarta et al., 2011) are indicated by the grey ellipsoid. Filled symbols are for Oen and empty symbols are for Cen. Composition of representative orthopyroxene used by Ulmer et Stadler (2001) to determine transitions between each phases is indicated. Orthopyroxenes compositions in transitional lithology sample (T) and chl-harzburgite (G) from Almirez are also indicated.

Coe and Muller (1973) established experimentally the relation between the Oen/LCen crystallographic orientations and the sense of shear during the transformation (**Fig.** 44), providing a potential technique to infer the orientation of the principal stresses in a similar way to the analysis of calcite, diopside, and plagioclase mechanical twins (e.g. Turner, 1953; Raleigh and Talbot, 1967, Egydio-Silva and Mainprice, 1999). The study of Frost et al. (1978) was the first one (and the last, to our knowledge) to apply this method. They analyzed a metaperidotite produced by serpentine dehydration in the Mount Stuart Batholith in the Central Cascades of Washington and determined that orientation of Oen host crystals containing LCen lamellae measured by universal stage differed significantly from the Oen bulk fabric

in the metaperidotite. Based on these data, they suggested that the Oen to LCen inversion was unrelated to the dehydration event and most likely caused by stresses related to the activity of a nearby shear zone.

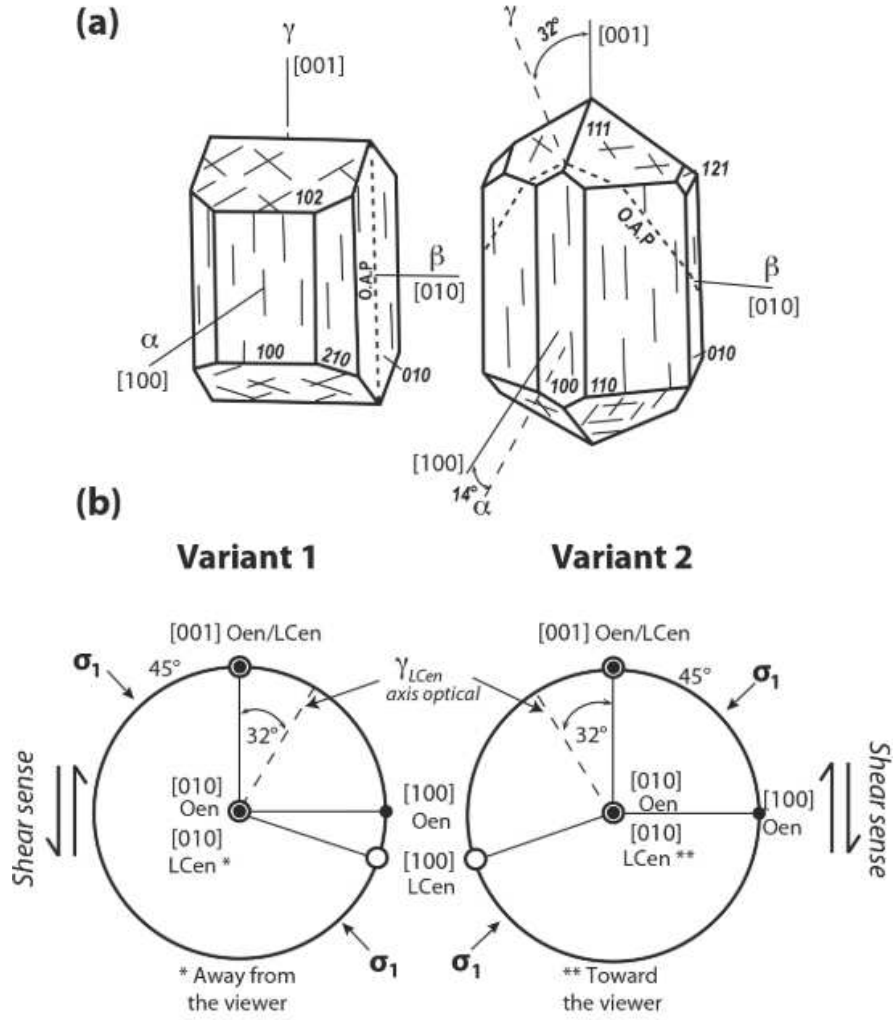

Figure 44 - Sketches (modified from Bambauer *et al.,* 1979) of orthoenstatite (Oen) and low-clinoenstatite (LCen) crystals and associated pole figures. (a) Orthoenstatite crystal with [100], [010] and [001] parallel to Y, X and Z optical indicatrices, respectively. $\alpha = \beta = \gamma = 90$ and optical axial plane (O.A.P) parallel to [001] in dashed black lines. (b) Low-clinoenstatite crystal with [010] parallel to X, [100] at 8-20° and [001] at 22-34° from the Y and Z optical indicatrices, respectively. $\alpha = \gamma = 90°$ and $\beta = 108.35°$ between the positive [100] and [001] axes according to Ohashi (1984). (c) Stereographic projection of LCen and Oen crystals illustrating the two transformation variants, associated shear senses and orientation of the maximum compressive stress.

The recent description of LCen lamellae in Oen in Cerro del Almirez metaperidotites (Padrón-Navarta et al. 2015) opens the possibility to investigate the Oen-LCen inversion in the context of a near-hydrostatic dehydrating system. These metaperidotites formed by serpentine dehydration at high-pressure conditions (eclogite facies, López Sánchez-Vizcaíno et al. 2005, Padrón-Navarta et al. 2010a, **Fig.** 43). They display no evidence of tectonic deformation after the dehydration event consistently with the absence of macroscopic shear zones within the

metaperidotite part of this unit. However, they show microstructures indicative of grain-scale deformation in response to compaction of the fluid-filled porosity produced by the serpentine dehydration reaction, which may reach ca. 20 vol. % (Padrón-Navarta et al. 2015). Compaction of a transient fluid-filled porosity produced by dehydration reactions should be associated with a complex stress field with variable orientation and magnitude at the grain scale (Wheeler 1987; Llana-Fúnez et al. 2012). The analysis of the orientation of LCen lamellae in the Cerro del Almirez peridotites allow testing this model by constraining the orientation of compressional stresses during porosity compaction. This work presents the first Electron Backscattered Diffraction (EBSD) study of the Oen to LCen inversion. Based on these data, we discuss the mechanisms of Oen transformation to LCen and the origin of the stresses responsible for this phase transformation in the Cerro del Almirez metaperidotites.

2. STRATEGY AND METHODS

2.1. Geological background and samples selection

The Cerro del Almirez (Nevado–Filábride Complex, Betic Cordillera, SE Spain) displays an undisturbed serpentine dehydration front, in which antigorite-schists are transformed to chlorite-harzburgites with granofels and spinifex-like textures (Trommsdorff et al. 1998; Garrido et al. 2005; López Sánchez-Vizcaíno et al. 2005, 2009, Padrón-Navarta et al. 2008, 2010a, 2011, 2015; Kahl et al. 2017). The reaction occurred at 680-710°C and 1.6-1.9 GPa (Fig.1) (López Sánchez-Vizcaíno et al., 2005, Padrón-Navarta et al., 2010a) during subduction of the Nevado-Filábride Complex in the Middle Miocene (López Sánchez-Vizcaíno et al. 2001). Later extensional tectonics resulted in exhumation of the reaction front (Martinez-Martinez et al., 2002), but this deformation was localized along the contacts of the ultramafic bodies with the metapelites and did not affect the internal parts of the ultramafic bodies (Jabaloy et al. 2015). The penetrative foliation of the antigorite serpentinite protolith is obliquely crosscut by the irregularly shaped reaction front marked by growth of the prograde assemblage (olivine + enstatite + chlorite +/- tremolite), suggesting that the dehydration reactions producing the clinoenstatite-bearing metaperidotites occurred under nearly static conditions (Padrón-Navarta et al., 2011, 2015).

In this study, we analyse the orientation of Oen and LCen in two samples from Cerro del Almirez: an antigorite-bearing transitional lithology (sample Al10-10, antigorite present), a chlorite-serpentinite collected ca. 70 cm away from the first isograd of the dehydration reaction, which is marked by the growth of coarse-grained chlorite, and an antigorite-absent chlorite-harzburgite with granofels texture collected ca. 3 m away from the same isograd (Al10-11, **Fig.** 45) (Padrón-Navarta et al. 2015).

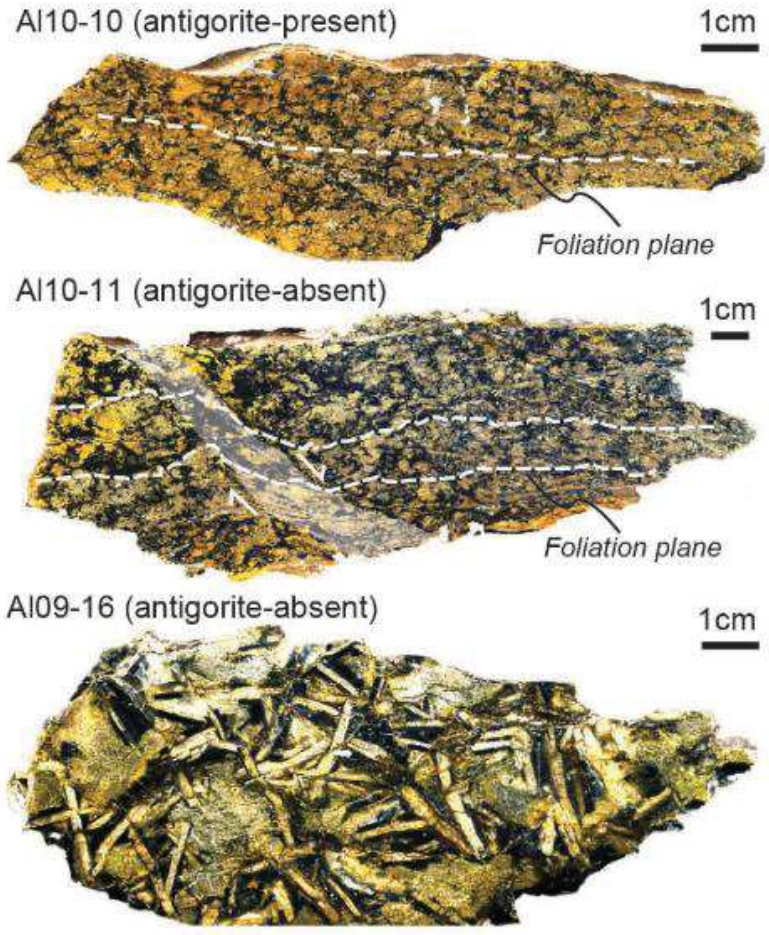

Figure 45 - Studied samples: Al10-10: transitional lithology sample with antigorite crystals, Al10-11: chl-harzburgite with no antigorite, Al09-16: chl-harzburgite with granofels texture and no antigorite crystals. Note the bent foliation plane of antigorite in Al10-11.

These two samples are oriented in a similar way and are distant by <2,5 m. The composition of orthopyroxene in both transitional and granofels texture metaperidotite is typically low in aluminium (0.10 wt. % Al_2O_3) with an X_{Mg} ($Mg/(Fe^{2+}+Mg)$ of 0.90-0.91 (Padrón-Navarta et al. 2011). Because LCen lamellae are only visible optically when the Oen [010] axis is at high angle to the thin section plane (see later discussion), four oriented sections - two XZ sections (A_1 and A_2), one

XY (B), and one YZ (C) section, where X defines the lineation and Z the normal to the foliation plane - were analyzed for each sample.

In addition, we performed detailed observations of a large bent Oen crystal (4 mm in length) from a coarse grained chlorite-harzburgite with granofels texture (Al09-16) collected at 25 m from the reaction front. The continuous and strong variation of the orientation of the host Oen crystal allowed us to test the relation between the sense of the shear during the LCen martensitic transformation and the orientation of the host Oen relative to the local stresses (Coe and Muller, 1973). Although chlorite-harzburgites with pseudospinifex texture also contain nanometer size LCen (Ruiz-Cruz et al. 1999), metaperidotites with this texture were not investigated, since the LCen lamellae in these peridotites are below both optical and EBSD resolution.

2.2. Analytical techniques

We performed EBSD analyses at Géosciences Montpellier (France). We used a Camscan Crystal Probe XF500 with a EBSD HKL NordlysNano detector to measure the crystallographic orientation of the LCen lamellae and a JEOL 5600 with a EBSD NordlysNano detector to map the orientation of Oen with a resolution of 16-27 μm over the whole thin section. In order to obtain the clearest Kikuchi patterns, the binning mode was set to 2x2 for both spot analyses and orientation mapping of small areas containing LCen lamellae (Table 1). Frame averaging was set to 2 to decrease noise. Reference LCen diffraction patterns were indexed using the crystallographic data of Morimoto *et al.*, (1960) with a=9.620 Å, b=8.825 Å, c=5.188 Å, and β = 71.67°, because these parameters resulted in the best fit of the observed patterns, producing Mean Angular Deviation (MAD) values ≤ 0.50° (Table 1). For further treatment, we transformed the LCen orientations to the conventional monoclinic setting (**Fig.** 44, β = 108.33°; Ohashi, 1984) by adding 180° to the third Bunge Euler angle.

Apparent thickness of LCen lamellae varies from <1 μm to 50 μm. This implies in EBSD measurements steps of 0.2-0.5 μm and makes EBSD mapping of the whole thin section too time consuming. Therefore crystals of Oen containing LCen were first identified by optical microscopy and then the orientation of both Oen host and LCen host was measured by EBSD using either spot analysis or small-scale maps. We

successfully indexed more than 84% of the optically identified LCen crystals despite the small size of the lamellae.

This grain-by-grain analysis is also time consuming. To enhance the statistics, we used a mixed EBSD-optical technique, in which the orientation of LCen crystals was calculated from the host Oen crystal determined by EBSD mapping and the phase transformation variant (dextral or sinistral shearing, **Fig.** 44) was identified by optical microscopy. Optical microscopy observations under crossed-polarized light allow the determination of the relative orientation of the γ-optical axis of LCen relatively to the host Oen (i.e. right or left LCen extinction relative to the [001] Oen/LCen direction, Coe and Muller, 1973). Since the LCen γ-optical axis is at 32° to [001] and lies in the obtuse angle [100]^[001] in the monoclinic setting of Ohashi (1984) (**Fig.** 44), knowledge of the orientation of this optical axis allows the determination of the full orientation of the LCen crystal and therefore the orientation of the main compressional stress. The number of Oen crystals hosting LCen lamellae identified in each thin section, as well as the proportions of the two LCen variants are listed in Table 1.

Orientation data for both LCen and Oen were analyzed using MTEX (Hielscher & Schaeben, 2008, Bachmann et al., 2010;; Mainprice et al., 2014). They are displayed as pole figures in the XYZ reference frame, which is based on the orientation of the foliation and lineation of the precursor serpentinite. The calculated LCen orientations based on the orientations of the measured host Oen orientations given by EBSD data and optical determinations of the variant selection are consistent with the EBSD data of LCen for both samples (**Fig.** 46).

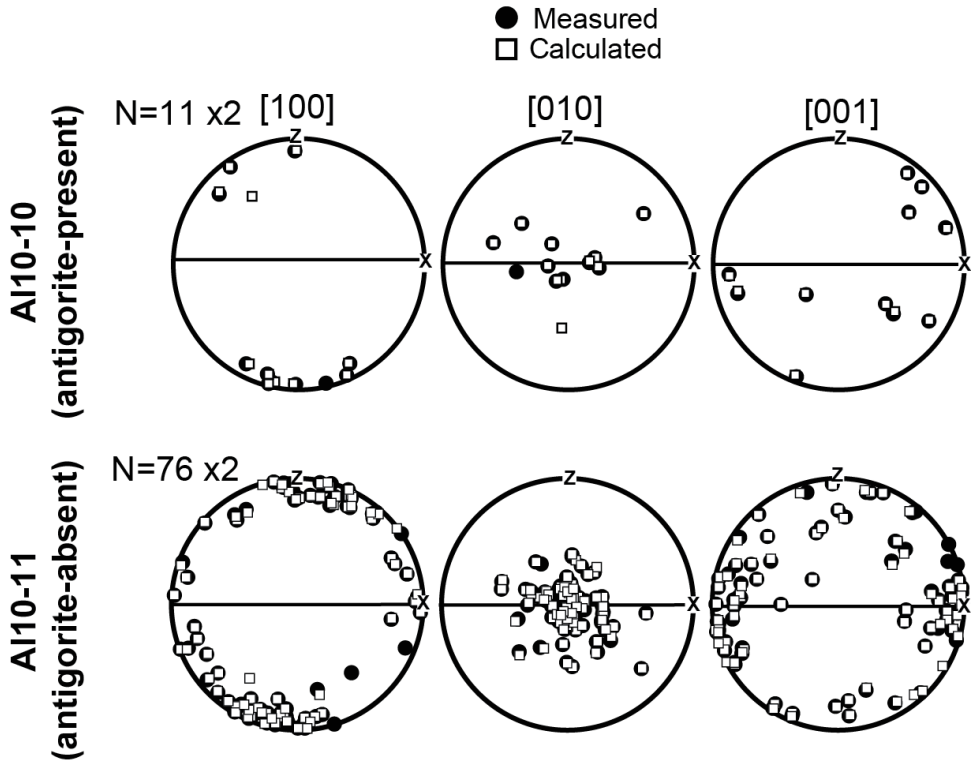

Figure 46 - Comparison between measured (black circles) and calculated (white squares) LCen data for samples Al10-10 (antigorite-present) and Al10-11 (antigorite-absent). Note the coherence between the two datasets. The rare discordant points may be attributed to errors in the optical estimation of the transformation variant

This validates the mixed EBSD-optical approach, which is considerably faster than the LCen EBSD analysis. In addition, to evaluate what would be the LCen population if all Oen crystals in the rock contained LCen lamellae, we wrote a MTEX script, which, based on the theoretical transformation relation (**Fig.** 44), converted the Oen orientations measured over the entire thin section by EBSD mapping into LCen orientations with a random variant choice. When the orientation of LCen is measured by EBSD, the type of variant and the orientation of the main compressional stress (σ_1) for each Oen grain hosting LCen is uniquely determined. The orientation of σ_1 can be then computed, for instance, by a 45° clockwise rotation of the orientation data for LCen around the positive $[010]_{LCen}$ axis (c.f. **Fig.** 44, note that in this figure the positive $[010]_{LCen}$ axis points away from the viewer in case of variant 1). The orientation of σ_1 is parallel to the orientation of $[001]_{LCen}$ of the rotated data. More generally, however, the orientation of σ_1 can be determined by knowing (1) the orientation of the Oen host and (2) the type of LCen variant, which can be obtained

by optical microscopy. Because two crystallographically opposite orientations of $[010]_{Oen}$ are compatible for each type of LCen variant (only the one with $[010]_{Oen}$ away from the viewer is represented in **Fig.** 44), the sign of rotation (clockwise or anticlockwise) depends on the orientation of the positive $[010]_{Oen}$ axis. A simple MTEX Matlab script is provided as Appendix to compute the orientation of σ_1 based exclusively on the orientation data for Oen and the type of LCen variant.

Table 1. Orthoenstatite (Oen) and low clinoenstatite (LCen) analyzed per section and details of EBSD settings used[a].

Sample	Al10-10				Al10-11			
Section	A_1	A_2	B	C	A_1	A_2	B	C
Nb Oen	96	43	46	23	211	116	94	3
Nb Oen hosting LCen	11	7	1	6	76	34	3	3
Variant 1	7	3	0	3	50	14	1	1
Variant 2	4	4	1	3	26	20	2	2
% of Oen hosting LCen	11	16	2	26	36	29	3	100
Crystal Probe								
Exposure Time (ms)	175	132	132	132	175	131	395	395
MAD (LCen)	0.54	0.27	0.33	0.39	0.59	0.33	0.44	0.36
JEOL5600								
Exposure Time (ms)	12	21	21	21	12	20	21	21
Step Size (µm)	19	27	27	27	19	16	17	17

[a]Binning mode for Crystal probe is 2x2 (672x512 pixels) and for JEOL 5600: 4x4 (336x256) pixels)

3. RESULTS

3.1. Low-clinoenstatite optical features

In optical microscopy with cross-polarized light, LCen lamellae generally appear as light to dark grey <1 µm to up to 50 µm wide elongated bands within the Oen crystals (**Fig.** 47a). Sample Al09-16 contains a large bent Oen grain hosting LCen lamellae, whose extinction position changes abruptly across the microfold hinge, indicating a change in phase transition variant (**Fig.** 44) in response to the change in the orientation of the Oen crystal relative to the main compressive stress (**Fig.** 47a). EBSD orientation mapping validates this interpretation (Figs. 5b and c). Comparison of Kikuchi patterns from the Oen host and both LCen lamellae highlights that they differ by the aspect of the (121) band, which is composite for Oen, but single and thick in LCen, with asymmetric contrast for the two variants (**Fig.** 47c).

Projection of all Oen orientations obtained by EBSD mapping of the whole thin section for the antigorite-present sample Al10-10 and for the antigorite-absent sample Al10-11 reveals a weak but consistent crystal preferred orientation (CPO) characterized by [100] axes dominantly at low angle to the normal to the foliation (Z) and [001] axes forming a wide girdle at low angle to the foliation XY plane (**Fig.** 48a). In Al10-10, [010] axes are highly dispersed, but in Al10-11 they form a weak maximum at low angle to the Y direction.

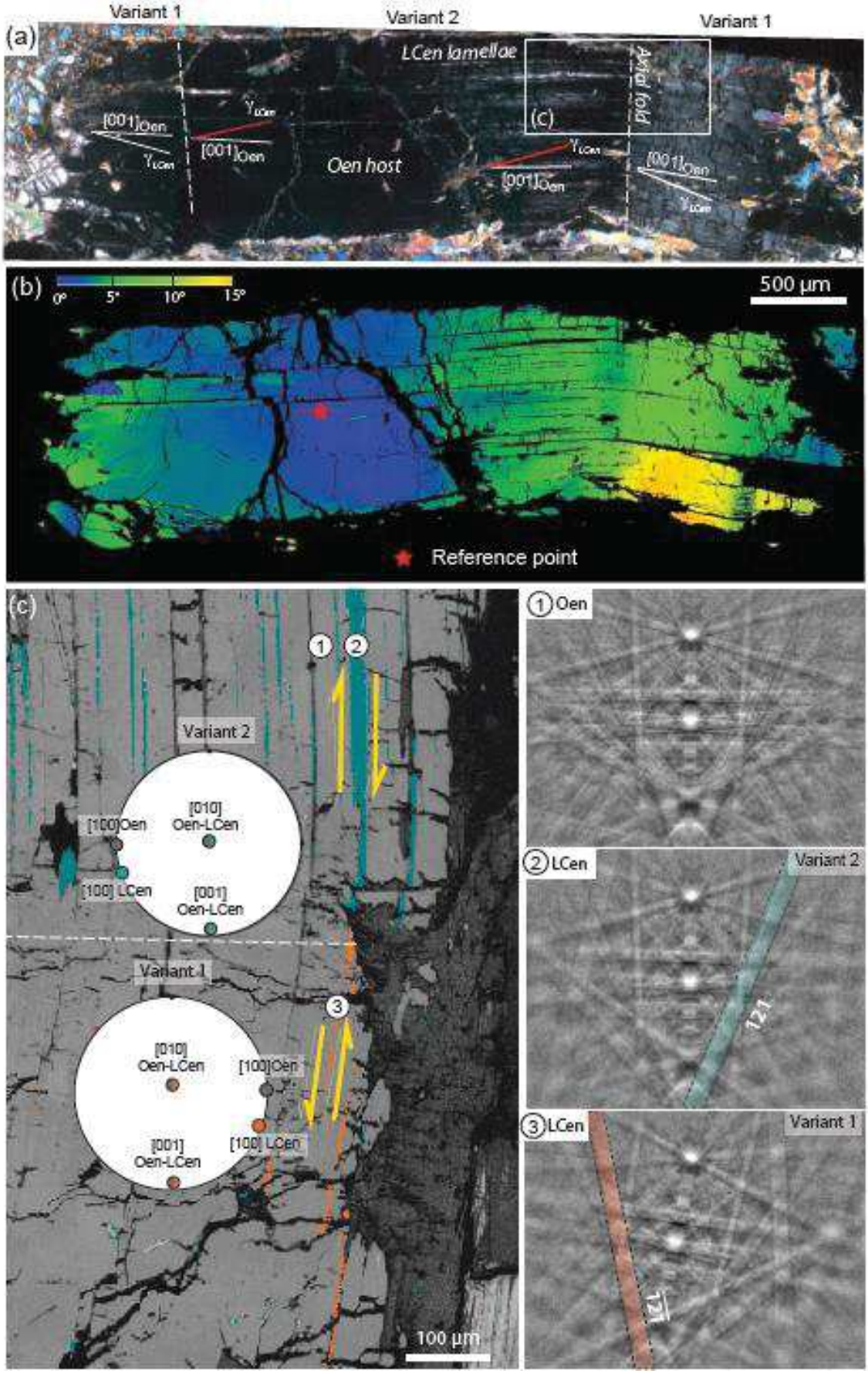

Figure 47 - (a) Cross-polarized light image of a kinked Oen grain from Al09-16 sample with LCen lamellae (white thin bands). Extinction position of LCen lamellae changes abruptly at the fold hinge indicating a change in transformation variant, which is confirmed by the change in the Kikuchi patterns in (d). Opposite shear sense assumed to have produced the two variants is indicated in the figure. (b): Misorientation map of the bent grain showing variation of Euler angle. Red star indicates reference point from which Euler angles are compared. (c): Band contrast image of the fold hinge zone with Euler colours for LCen lamellae. Note the change in orientation of the LCen lamellae. (d): Electron back-scattered diffraction pattern (Kikuchi bands) from Oen host and LCen lamellae. The main difference between the Oen host and the LCen lamellae is the 1-21 band, which is composed by multiple bands in Oen, but is single and thick in LCen, with asymmetric contrast for the two variants.

Orientation data from EBSD spot analyses of LCen-hosting Oen crystals shows a consistent, but apparently stronger crystal preferred orientation (**Fig.** 48a,b), probably due to the smaller number of grains analyzed and the biasing effect of optical identification of LCen (see below). Oen and LCen have subparallel [010] and [001] axes. The [010] directions tend to concentrate parallel to the structural Y direction, whereas [001] is dispersed at low angle to the XZ plane, with a weak concentration subparallel to X in sample Al10-11. Analysis of LCen data for sample Al10-11 highlights that the two LCen variants have significantly different orientations, with concentration of [100] axes at low angle to the Z direction for the variant 1 and close to the X direction for variant 2 (**Fig.** 48c). This phenomenon is less marked in sample Al10-10, maybe because of the lower number of LCen-bearing Oen crystals observed in this sample. In sample Al10-11, the population of variant 1 is slightly more abundant than the variant 2 one; it represents 66% of measured data in this section (Table 1).

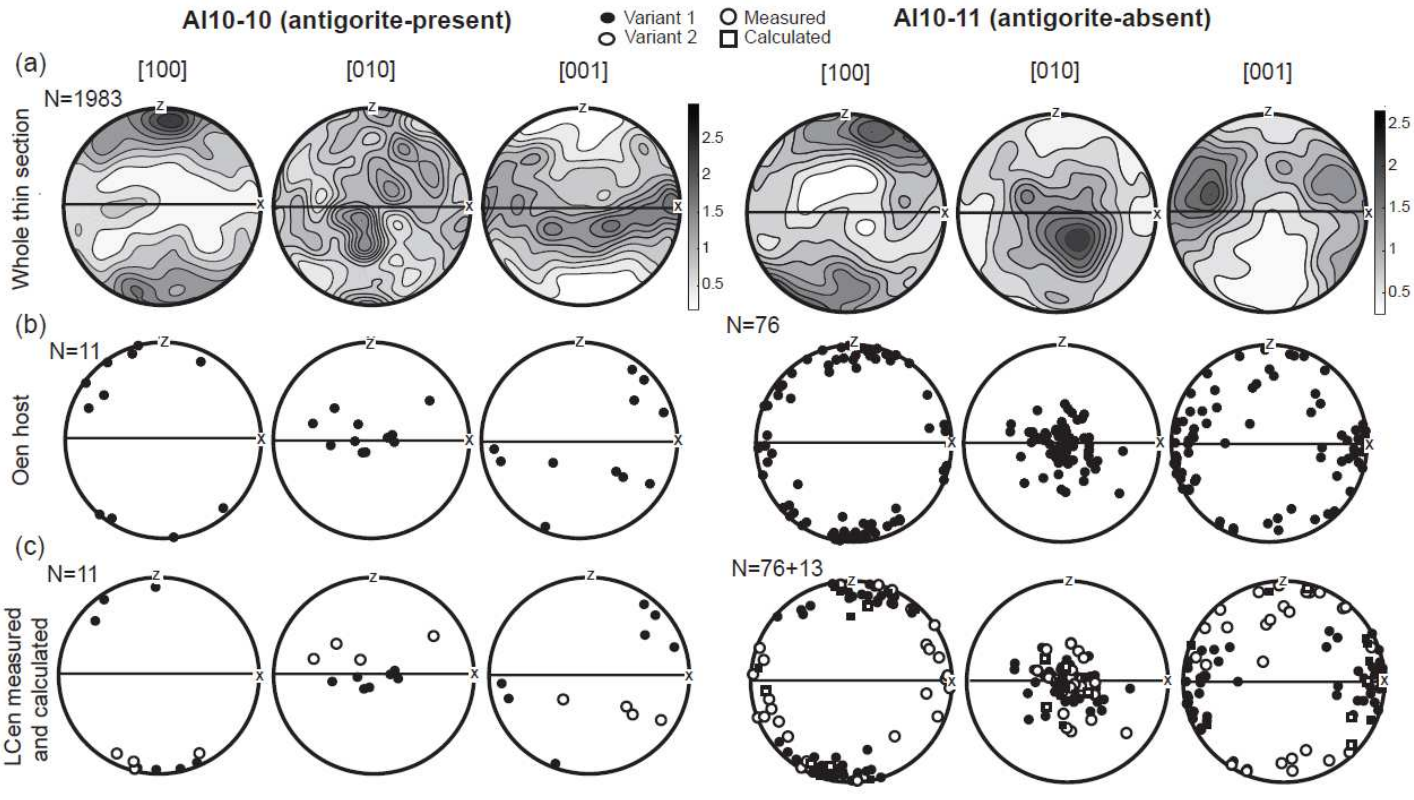

Figure 48 - Crystallographic orientations of Oen and LCen in samples Al10-10 (antigorite-present, section A_1) and Al10-11 (antigorite-absent, section A_1). (a) Oen orientations over the entire thin section. (b) LCen-bearing Oen. (c) Same projection than (c) but with variant 1 (black) and variant 2 (white) for measured (circles) and calculated (squares) data. LCen of variant 2 are distinct from LCen of variant 1. N indicates number of grains. The same reference frame for all projections was used. Horizontal black thick line represents the foliation plane, which is vertical and oriented E-W. Projections are in lower hemisphere.

3.3. Correcting for bias in LCen optical detection

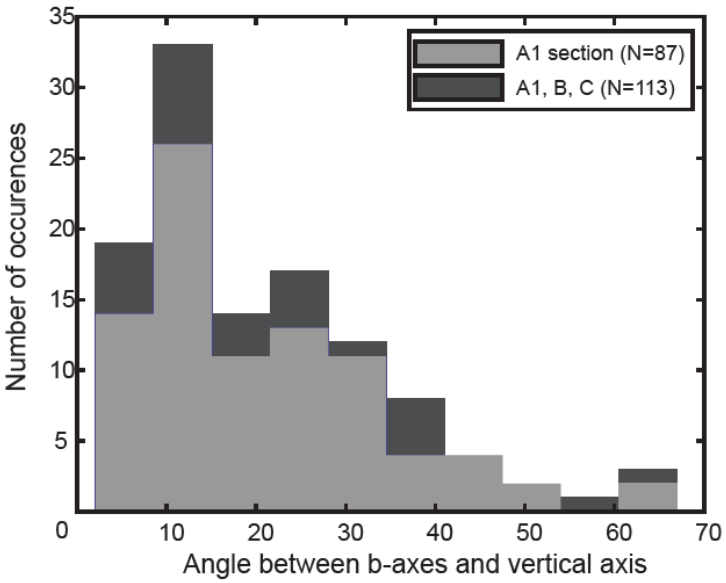

Figure 49 - Histograms of distribution of angles between [010] axis and the thin section normal for LCen-bearing Oen.

LCen lamellae are only visible optically when their [010] axis is nearly parallel to the microscope axis. Thus the thin sections studied may have LCen that are not detectable optically. Calculation of the angle between [010] axes of measured and calculated LCen data and the normal to the thin section show that observed LCen-bearing Oen grains have their [010] axes within 50° of the normal to the thin section (**Fig.** 49).

This may result in bias in the estimation of main compressive stress direction. To minimise this bias, orientation analyses were performed on 3 orthogonal sections (**Fig.** 50). LCen orientations derived from these additional sections (**Fig.** 50) are consistent with those in **Figure** 48, in particular for the antigorite-absent sample (AI10-11). For the antigorite-present sample AI10-10, despite doubling the number of measurements, no clear preferred orientation of the two variants can be defined.

3.4. Compressional stress orientation

Main compressional stresses (σ_1) calculated based on LCen orientation data in the antigorite-present sample AI10-10 shows no clear preferred orientation, except for a weak maximum normal to the foliation, which is mainly derived from the data from the A_1 section (**Fig.** 50a). In contrast, main compressional stresses calculated for the antigorite-absent sample AI10-11 show a marked preferred orientation in the XZ plane, between 0-90° clockwise from the X direction, with a maximum at 49° of the foliation plane. It is noteworthy that the orientation data from the two variants add up consistently for the definition of a single stress orientation.

To evaluate what would be the predicted main compressive stress orientation if all Oen grains in the two samples were LCen-bearing, we estimated the associated LCen orientations considering a random variant selection. Both datasets result in a

very weak orientation of the main compressive stress, which is almost random for sample Al10-10 (**Fig.** 50a) and forms a wide girdle at high angle to the Y direction for sample Al10-11 clearly differing from the prediction based on the measured LCen orientations (**Fig.** 50b).

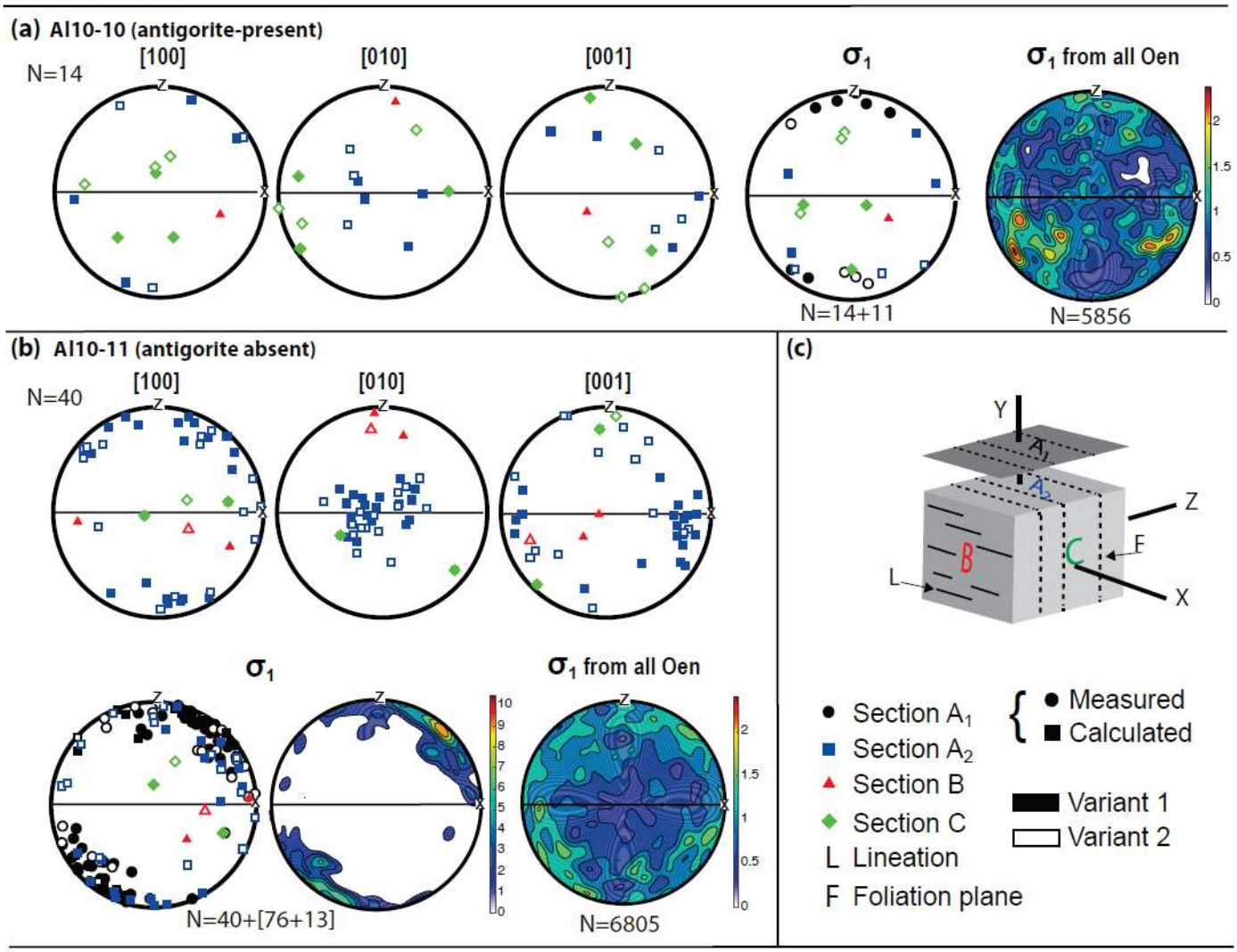

Figure 50 - (a) Crystallographic orientations of LCen lamellae calculated for thin sections A_2, B, and C of samples Al10-10 (antigorite-present) and Al10-11 (antigorite-absent). (b) Calculated orientation of the main compressional stress based on the entire LCen orientation dataset. (c) Sketch showing the orientation of A_2 (blue), B (red) and C (green) thin sections relative to the foliation plane and lineation. Filled markers represent variant 1 LCen and empty markers, variant 2. Squares represent calculated data and dots, measured data in A_1 section. N indicates number of data in each pole figure. Reference frame is the foliation and lineation of the serpentinite protolith, as in Figure 5.

4. DISCUSSION

4.1. Stress-induced Oen to LCen inversion

The present microstructural observations clearly point to the formation of LCen lamellae by martensitic transformation of Oen. A key observation is the occurrence of LCen lamellae in sample Al09-16 with two different extinctions in a single large bent Oen grain (**Fig.** 47), which suggests that projection of the local stress on the two fold limbs gives rise to shear stresses with opposite senses leading to development of different LCen variants in the two fold limbs.

Peak metamorphic conditions, which led to dehydration of the serpentinite and formation of the host Oen crystals in the Cerro del Almirez metaserpentinites, are estimated at 1.6-1.9 GPa and temperatures of 680-710°C (**Fig.** 43) (Padrón-Navarta *et al.*, 2010a, 2011). These conditions are within the Oen field according to the phase diagram of Ulmer and Stalder (2001), which was based on experiments on orthopyroxenes with compositions ranging from pure enstatite (Mg# = 1,00) to 10% ferrosilite (Mg# =0.90), that is, for compositions similar to those of the studied samples (Mg# = 0.89-0.90). The phase transition between LCen and Oen is, however, displaced to higher temperatures if shear stresses are applied in the [001] direction on (100) planes of orthoenstatite (Coe, 1970). Because of the different nature and rheology of neighboring grains and, more important, of the reduced solid-solid contact points in the presence of porosity, a heterogeneous stress field, with locally high stresses, might form during compaction of porosity (e.g. Llana-Fúnez *et al.*, 2012). Such stresses may induce the phase transition from Oen to LCen at lower pressures than those predicted for static conditions. Padrón-Navarta *et al* (2015) estimated the magnitude of the stresses required to trigger orthoenstatite inversion at the peak conditions recorded by the Chl-harzburgite with granofels texture in Cerro Almirez based on the coexistence of plastic deformation microstructure in Oen hosts and coeval Oen inversion to LCen (**Fig.** 47) following the approaches of Raleigh et al. (1971) and Coe and Kirby (1975). Estimated differential stresses are on the order of 5-70 MPa.

The most favorable orientation for promoting the transformation of Oen to LCen is when the compression is applied at 45° from [100] and [001] axes, since this results in the highest shear stresses on (100) planes, allowing the transformation to

occur at minimum compressive stress levels. The present calculations of the maximum compressive stress orientation are based on this assumption.

The two samples, which are separated by less than 2.5 m, have recorded different stress fields (**Fig.** 50a,b). Such short wavelength changes in the stress field are not compatible with a tectonic origin related to subduction or to the exhumation of the massif. This further corroborates the hypothesis that the stresses producing the Oen to LCen transformation were associated with the compaction of the fluid-filled porosity produced by the antigorite dehydration.

The consistent orientation of the maximum compressive stress from the two variant populations of LCen in the antigorite-absent sample Al10-11 indicates that two populations of Oen with markedly different orientations have recorded the same orientation of compressional stress (**Fig.** 48c, **Fig.** 50b). This observation implies a homogeneous stress field at the thin section (cm) scale and is at odds with the strong variations in the compressive stress orientation at the grain-scale modelled by Llana-Fúnez *et al* (2012). A highly variable orientation of the maximum compressional stress applied on an Oen population with strong CPO would result in a lack of clear orientation distribution of the two LCen variant populations, as predicted for the antigorite-present sample Al10-10 and for the calculations in which we considered that all Oen in the sections were LCen-bearing (**Fig.** 50a).

4.2. Spatial variation of the stress field and compaction scales

The variation in degree of dehydration and in the associated porosity could be at the origin of the differences in the stress field between the two samples. The antigorite-present sample Al10-10 was only partially dehydrated. Lack of or incomplete fluid extraction at this early stage of the process might have resulted in a small region of solid grain-to-grain contacts and in an increase of the hydrostatic component, producing a highly heterogeneous stress field with no macroscopic preferred orientation of σ_1, similar to the one modeled by Wheeler (1987, see also Fig 1 in Llana-Fúnez *et al* 2012). The antigorite-absent sample Al10-11, on the other hand, records a more developed stage of the process, in which fluid extraction by compaction and porosity collapse might have resulted in a more homogeneous stress field. Macroscopic (> 1-2 cm) diffuse shear zones that might be related to the

compaction processes are observed in this sample (**Fig.** 45b), pointing to a coherent stress field at the sample scale.

The compaction length scale (δ, in m) during dehydration reactions is the deformation length scale over which pore fluids are at hydrostatic pressure and can move independently of the compaction process. It can be expressed as (Connolly 1997, 2010):

$$\delta \approx \sqrt{\frac{3}{4}\frac{\eta}{\mu}\frac{k}{\phi}} \quad (1)$$

where k is the permeability, μ is the fluid viscosity (10^{-4} Pa·s, Connolly 1997), η is the dynamic viscosity, and ϕ is the porosity. The viscosity of serpentinite before dehydration at the temperature and pressure of interest (680°C and 1.7 GPa) is $4.0\text{x}10^{20}$ Pa·s for a shear stress of 1 MPa (using the power law equation of Hilairet et al. 2007), which is in the same range as the estimated viscosity of the fluid-bearing metaperidotites during the compaction process ($1.0\text{x}10^{20}$ Pa·s at 680°C for a shear stress of 70 MPa, Padrón-Navarta et al. 2015). Therefore the evolution of the compaction scale during the dehydration processes is expected to be influenced by the relative changes in the ratio of k/ϕ during dehydration rather than by contrasting viscosities between the serpentinite and compacting metaperidotite. This is supported by the limited macroscopic perturbation of the dehydration front and the serpentinite foliation plane during the dehydration event (**Fig.** 45).

Direct experimental measurements of permeability and porosity in serpentinite are only available at 50 MPa (Kawano et al., 2011, Katayama et al., 2012). Extrapolation to higher pressure (1.7 GPa) following the approach used by Kawano et al. (2011) results in extremely low permeability perpendicular to foliation ($3.5\text{x}10^{-27}$ m^2). Assuming this porosity (k) and using the theoretical approach of Gueguen and Palciauskas (1994), which considers cylindrical tube channels, to relate permeability and porosity:

$$k = k_0 \left(\frac{\phi}{\phi_0}\right)^2 \quad (2)$$

the porosity (ϕ) in the serpentinite at 1.7 GPa before dehydration is also estimated to be very low (0.002 %), using the reference permeability (k_0) and porosity (ϕ_0) values at 50 MPa (Kawano et al. 2011).

During the initial stages of dehydration (represented by the antigorite-present sample Al10-10), the increase in porosity would lead to an increase in compaction length compatible with the near-hydrostatic stress recorded in this sample. An increase in porosity by three orders of magnitude (up to 2 %) relative to the background porosity in the serpentinite as a consequence of solid volume reduction during the reaction would result in a compaction length in the order of 150m using Eq. (1) and (2). The observation of non-hydrostatic stresses in the antigorite-absent sample Al10-11 suggests that porosity reduction due to fluid extraction resulted in significantly smaller compaction lengths. The poor knowledge of the quantitative relationship between permeability and porosity during the reaction progress makes quantifying the reduction in the compaction length challenging. However, the observed meter-scale variation in stress distribution (interpreted as a change from hydrostatic to non-hydrostatic conditions) requires a reduction in compaction length equivalent to the one that might be produced by a decrease in porosity by two orders of magnitude, that is, almost complete fluid extraction.

5. IMPLICATIONS

The present observations imply that compaction during dehydration of serpentinites may generate differential stresses on the order of several tens of MPa. These stresses might be recorded by shear-induced phase transformations such as the inversion of orthoenstatite produced by the dehydration reaction to low-clinoenstatite. The present observations, which record variable stress fields in two samples separated by <3 m and recording different stages of the reaction, suggest that the stress field varies both in time and space in response to the reaction progress and evolution of compaction. At the initial stages of the reaction, when porosity is high and most grain-boundaries are wet (reducing solid-solid contacts) the system behaves as near-hydrostatic and compaction length-scales are large (hundreds of meters). When reaction progresses, decrease in porosity reduces the compaction length to the meter scale and compaction may organize the stress field. This might influence fluid migration resulting in macroscopic compaction structures

(from dm to m) that can be potentially identified in the field in the absent of post-dehydration deformation.

CHAPITRE VI

CONCLUSIONS ET PERSPECTIVES

VI. CONCLUSIONS ET PERSPECTIVES

1. RAPPEL DE LA PROBLEMATIQUE

Les fluides interviennent dans de nombreux processus d'importance économique et sociétale. Leurs déplacements sont associés par exemple aux dépôts de minéraux d'intérêt économique (Ding *et al.*, 2018; Fyfe, 1987; Morales *et al.*, 2016) ou à la formation de volcans d'arc à éruptions explosives provoquée par la fusion partielle du coin du manteau au niveau des zones de subduction (Defant and Drummond, 1993; Elliott *et al.*, 1997; Kelemen *et al.*, 2003). Ainsi, comprendre la manière dont se déplacent les fluides permet en retour de comprendre ces phénomènes.

Bien que de nombreuses études aient déjà été menées sur la manière dont se déplacent les fluides dans les parties les plus superficielles de la terre (<5 km), apportant de nombreuses contraintes sur le sujet (Gay and Migeon, 2017; Kyser and Hiatt, 2003), la manière dont se déplacent les fluides dans les parties plus profondes (transition croûte-manteau, zones de subduction) et les processus qui y sont associés restent encore largement débattus.

Les réactions de déshydratation des serpentinites libérant d'importantes quantités de fluides au niveau des zones de subduction sont l'objet de nombreuses études portant sur le changement de comportement rhéologique des serpentinites qui se déshydratent et qui pourrait être à l'origine de tremblements de terre (Hacker, 2003; Peacock, 2001; Raleigh and Paterson, 1965) lorsque les fluides présents dans les pores produits par la déshydratation s'échappent.

Un modèle numérique d'échappement des fluides : le « porosity wave » a notamment été proposé (Connolly, 1997, 2010). Il repose sur la manière dont la serpentinite se déforme par compaction/dilatation de la matrice solide ou par fracturation hydraulique lors de la déshydratation, qui produit en même temps de la porosité où les fluides générés sont stockés. Le cycle de compaction de la porosité (réduction du volume de pores) et de dilatation de la matrice (ouverture de volume de pores) permet aux fluides de se déplacer.

Des études expérimentales (Leclère *et al.*, 2018; Llana-Fúnez *et al.*, 2012) ou basées sur des modèles numériques (Miller *et al.*, 2003; Wang and Wong, 2003) montrent que l'échappement des fluides produits par déshydratation conduit à une

augmentation de la cinétique de réaction. Une étude naturaliste a suggéré qu'il pouvait y avoir un lien entre la texture des minéraux produits par déshydratation de l'antigorite et le mode d'échappement des fluides (Padrón-Navarta *et al.*, 2011).

Cette thèse a pour objectif d'étudier les mécanismes de déplacements des fluides générés par déshydratation de la serpentinite en analysant les textures des minéraux produits par la réaction. Elle comporte trois parties, la première est une étude de terrain des serpentinites de Val Malenco (Italie) déshydratées au contact de l'intrusion du Bergell. La deuxième est une étude expérimentale de déshydratation d'échantillons naturels pour confronter les résultats aux observations de terrain. La troisième partie est consacrée à une étude microstructurale pour décrire l'orientation de la contrainte lors de la compaction métamorphique liée à la déshydratation.

2. RESULTATS OBTENUS

2.1. Etude de serpentinites déshydratées de manière naturelle

L'étude est basée sur des échantillons de serpentinites de Val Malenco déshydratées au contact de l'intrusion du Bergell de manière quasi-statique (sans épisode de déformation majeure post déshydratation). Ces serpentinites ont été choisies parce que les isogrades correspondant aux différentes réactions de déshydratation de l'antigorite sont préservées et parallèles à l'intrusion. Cette particularité permet de suivre l'évolution des réactions et les textures associées. La cartographie des orientations des serpentinites, métapéridotites et veines rencontrées et échantillonnées ainsi que l'analyse des échantillons au microscope optique, à l'EBSD et à la microsonde électronique ont permis de montrer les résultats suivants :

- Les serpentinites se transforment progressivement en métapéridotites. Le contact entre les deux n'est pas franc, à la différence des serpentinites déshydratées au massif de Cerro del Almirez (Padrón-Navarta et al. 2011). La foliation des serpentinites est préservée lors de la transformation. Les olivines des métapéridotites montrent une grande variabilité de taille et de forme.

- Les veines sont composées de minéraux issus des réactions de déshydratation (Ol, Ol-Tr, Ol-Tc) et sont localisées dans des zones de plus basses températures que les isogrades correspondantes. Les veines ont deux morphologies différentes : droite ou diffuse, mais ont toutes globalement la même orientation : N°70 et un pendage sub-vertical. Les olivines ont une texture de type jackstraw dans les veines à olivine-talc ou granulaires dans les veines à olivine et olivine-tremolite.

- A l'échelle microscopique, les serpentinites sont majoritairement foliées, la foliation étant marquée par l'orientation préférentielle de l'antigorite. La transformation en métapéridotite est progressive avec l'apparition d'olivine et de talc allongés dans le plan de foliation. Les métapéridotites ont des olivines granulaires ou allongées dans le plan de foliation avec de la surcroissance dendritique. Des marques de déformation sont visibles : extinctions onduleuses des olivines et cristaux de talc et de chlorite parfois pliés.

- L'analyse des veines à olivine-talc à l'échelle microscopie montre que la transition vers la serpentinite est progressive et que les olivines sont allongées parallèlement au plan de la veine. Quelques cristaux d'olivine présentent de faibles extinctions onduleuses.

- L'antigorite et l'olivine des métapéridotites ont des orientations cristallographiques préférentielles très marquées et qui sont corrélées entre elles. Les axes [100] des olivines granulaires et les axes [010] des olivines allongées sont parallèles aux axes [001] de l'antigorite.

- Les olivines des veines à olivine-talc montrent aussi une orientation cristallographique préférentielle corrélée avec le plan de la veine, les axes [010] des olivines étant perpendiculaires au plan de la veine. Il n'y a pas d'orientation préférentielle des axes [100] et [001] dans ce plan.

- Les compositions des minéraux restent globalement constantes au cours des réactions de déshydratation mais du métasomatisme peut avoir lieu au niveau des veines avec des appauvrissements en SiO_2.

- Pour des temps d'ouverture des veines suffisamment longs, les fluides générés au front de réaction sont drainés et évacués dans le plan de fracture entrainant ainsi la propagation du front de réaction dans la direction opposée.

Ces résultats montrent que les veines sont des fractures qui ont été ouvertes par extension lors de l'intrusion du Bergell et qui ont servi de chemin d'échappement aux fluides produits par déshydratation de l'antigorite. Ce drainage focalisé des fluides par les veines a permis aux réactions d'avoir lieu à plus basse température et de produire des textures d'olivine en déséquilibre. L'aplatissement des olivines et leur élongation aléatoire dans le plan des veines indiquent qu'un gradient de fluide parallèle au plan de la veine contrôlait leur croissance. Ce gradient de fluide anisotrope est attribué à l'anisotropie de perméabilité de la foliation définie par l'antigorite comme démontré expérimentalement par Kawano et al. (2011). Durant leur temps d'ouverture, les fluides produits au front de réaction avec l'antigorite ont été évacués à travers le cœur de la veine, propageant le front de réaction dans la direction opposée. Les veines se sont fermées par compaction ou par obstruction provoquée par la cristallisation des produits de réaction.

Parallèlement, les serpentinites qui se déshydrataient ont produit des olivines granulaires corrélées à l'antigorite par relation topotactique dans le cas où les fluides s'échappaient lentement de manière pervasive. Dans le cas des serpentinites foliées, celles-ci ont produit lors de la déshydratation des olivines aplaties et allongées de manière aléatoire parallèlement au plan de foliation. Ceci est dû au fait que les fluides produits circulant de manière pervasive s'échappaient plus facilement parallèlement au plan de foliation des serpentinites (= anisotropie de perméabilité). Dans ce cas, le gradient de pression était parallèle à la foliation de l'antigorite, de la même manière que dans les veines à olivine-talc où le gradient était contrôlé par la géométrie de la veine. Les marqueurs de déformation observés sont attribués à la compaction métamorphique.

2.2. Etude de serpentinites déshydratées de manière expérimentale

Ce travail a été réalisé sur la presse Paterson au laboratoire de hautes pressions à Géosciences Montpellier. Une serpentinite faiblement foliée de Val Malenco et une serpentinite fortement foliée du massif de Cerro del Almirez ont été

utilisées comme matériel de départ pour les expériences. Ces serpentinites ont été déshydratées de manière statique (sans déformation appliquée) à 730°C et 300 MPa pendant dix heures, et les fluides produits ont été partiellement drainés par de l'alumine poreuse. Plusieurs expériences ont été réalisées en changeant l'orientation de la foliation pour évaluer l'effet du gradient de pression sur la texture. L'analyse des produits de réactions par microscopie électronique couplée à des analyses EDS et les analyses par EBSD ont permis d'obtenir les résultats suivants :

- La déshydratation de la serpentinite faiblement foliée de Val Malenco produit un assemblage d'olivine-talc (+H_2O) avec des olivines aciculaires de longueur < 20 µm au cœur de l'échantillon et des olivines sphériques nanomètriques (200 nm) à proximité de l'alumine poreuse. La porosité atteint jusqu'à 30%. L'olivine et l'antigorite ont de faibles orientations cristallographiques préférentielles corrélées, les axes [010] de l'olivine sont parallèles aux axes [001] de l'antigorite. Les olivines sont forstéritiques avec des inclusions de chlorite et/ou spinel.

- La déshydratation de la serpentinite fortement foliée de Cerro del Almirez produit aussi un assemblage olivine-talc avec des olivines aciculaires aléatoirement allongées dans le plan de foliation et des olivines granulaires. La porosité est de 25%. Des fractures orientées perpendiculairement à l'orientation de l'alumine poreuse sont visibles dans le plan de foliation et aussi perpendiculairement à ce plan. On observe de la croissance aciculaire d'olivine normale à l'orientation des fractures. Des olivines allongées parallèlement au plan de foliation sont également visibles. Ces olivines ont une très forte orientation cristallographique préférentielle corrélée avec celle de l'antigorite, les axes [010] des olivines allongées étant globalement parallèles aux axes [001] de l'antigorite tandis que pour les olivines granulaires, la corrélation est avec les axes [100]. Les olivines sont également forstéritiques et riches en inclusions.

L'assemblage minéralogique produit ne correspond pas à l'assemblage minéralogique à l'équilibre pour les conditions P-T expérimentales. La réaction a donc dû avoir lieu très rapidement au début de l'expérience, expulsant partiellement

les fluides vers l'alumine, empêchant ainsi le rééquilibrage de l'assemblage olivine-talc en assemblage olivine-enstatite. Plus précisément, des fractures se sont formées par expansion du volume du système puis se sont connectées les unes avec les autres jusqu'à l'alumine poreuse où les fluides se sont échappés, provoquant une augmentation très rapide de la vitesse de réaction et la cristallisation d'olivines aciculaires perpendiculaires à ces fractures.

La texture des olivines éloignées de l'alumine qui draine le système est contrôlée par l'anisotropie de perméabilité des serpentinites initiales. Dans le cas de la serpentinite fortement foliée, la circulation de fluide est circonscrite dans le plan de foliation, produisant des olivines aplaties dans ce plan sans direction préférentielle d'allongement. La corrélation entre les axes [010] de l'olivine et les axes [001] de l'antigorite de départ est contrôlée par le gradient de pression de fluide. Les microstructures des échantillons déshydratés expérimentalement sont similaires à celles des échantillons naturels étudiés dans le premier volet de la thèse.

Les olivines granulaires semblent s'être formées dans un contexte où la circulation de fluide est plus pervasive. Elles pourraient aussi correspondre au premier stade de cristallisation. La corrélation entre les axes [100] de l'olivine et les axes [001] de l'antigorite de départ semble être contrôlée par des relations topotactiques.

2.3. Impact de la compaction métamorphique sur la texture des serpentinites déshydratées

Ce travail est basé sur l'analyse de trois serpentinites qui enregistrent un gradient de déshydratation. Elles ont été collectées dans le massif de Cerro del Almirez, séparées de quelques mètres à partir de l'isograde. Elles contiennent toutes des orthoenstatites avec des lamelles de clinoenstatite. L'analyse au microscope optique et à l'EBSD, pour chaque échantillon, de trois sections perpendiculaires permet de retrouver l'orientation de la contrainte qui est à l'origine des clinoenstatites. Les résultats sont les suivants :

- L'orientation des orthoenstatites et des clinoenstatites de l'échantillon partiellement déshydraté est dispersée.
- Dans l'échantillon où l'antigorite est complètement déshydratée, deux populations correspondant aux orientations préférentielles des deux

variantes des clinoenstatites sont observées. Cela est la signature d'une forte orientation de la contrainte dans une seule direction.

La clinoenstatite se forme par transformation martensitique (=maclage mécanique). Ici, la contrainte a pour origine la compaction métamorphique. Dans le cas de l'échantillon partiellement déshydraté, la contrainte est hydrostatique elle correspond à la pression de fluide dans les pores connectés. Quand la déshydratation progresse, les fluides sont extraits et la compaction contrôle l'orientation de la contrainte qui devient directionnelle.

3. SYNTHÈSE GENERALE ET PERSPECTIVES

Cette thèse a montré au travers de trois études complémentaires que le mode de circulation des fluides lors de la déshydratation des serpentinites est enregistré par les textures de croissance de l'olivine.

Le travail expérimental a permis d'identifier les processus responsables des microstructures observées dans les échantillons naturels collectés à Val Malenco.

Ces résultats ont permis de proposer un scénario complet de migration des fluides depuis l'initiation de la déshydratation jusqu'à la compaction lorsque les fluides sont extraits.

La caractérisation des microstructures des grains d'olivine peut donc permettre de tracer la déshydratation et les trajets suivis par les fluides produits.

A Val Malenco, les serpentinites ont été déshydratées par l'intrusion du Bergell de manière quasi statique. L'extrapolation des processus observés aux zones de subduction devra prendre en compte des déformations plus importantes liées à la dynamique de la plaque plongeante, et en particulier les interactions entre la compaction résultant de la déshydratation et la composante tectonique.

Les réactions de déshydratation à une pression caractéristique des zones de subduction devrait résulter entre autre en un front de réaction plus court que celui observé à Val Malenco à cause des plus hautes pression de confinement qui limitent le développement de la perméabilité (Leclère et al., 2018). Ceci a effectivement été observé puisque le front de réaction du massif de Cerro del Almirez n'est que d'un mètre (Padrón-Navarta et al. (2011) et celui de Val Malenco de 125m (Figure 20).

L'impact de la déformation sur les réactions de déshydratation des serpentinites reste toutefois à éclaircir. Une manière d'aborder le problème serait d'utiliser l'approche employée dans cette thèse sur des échantillons naturels et expérimentaux déshydratés dans des contextes de déformation active. Une nouvelle étude récente sur les roches du massif de Cerro del Almirez (Dilissen et al., 2018) a montré des processus similaires à ceux exposés dans cette étude (couplage entre processus d'échappement de fluides et textures) mais en tenant compte des contraintes exercées pendant la déshydratation de la plaque plongeante qui contrôlent la texture de l'antigorite et donc celle des produits de déshydratation. Il reste toutefois fondamental de quantifier les échelles de temps des différents processus impliqués: croissance cristalline, compaction et déformation pour pouvoir discuter les rétroactions.

REFERENCES

Ague, J. J. (2013). Fluid Flow in the Deep Crust. *Treatise on Geochemistry: Second Edition* **4**, 195–228.

Amiguet, E., Van de Moortèle, B., Cordier, P., Hilairet, N. & Reynard, B. (2014). Deformation mechanisms and rheology of serpentines in experiments and in nature. *Journal of Geophysical Research: Solid Earth* **119**, 4640–4655.

Angel, R. J., Choplelas, A. & Ross, N. L. (1992). Stability of high-density clinoenstatite at upper-mantle pressures. *Nature* **358**, 322–324.

Arkwright, J. C., RUtter, E. H., Brodie, K. H. & Llana-Fúnez, S. (2008). Role of porosity and dehydration reaction on the deformation of hot-pressed serpentinite aggregates. *Journal of the Geological Society* **165**, 639–649.

Auzende, A., Escartin, J., Walte, N. P., Guillot, S., Hirth, G. & Frost, D. J. (2015). Deformation mechanisms of antigorite serpentinite at subduction zone conditions determined from experimentally and naturally deformed rocks. *Earth and Planetary Science Letters*. Elsevier B.V. **411**, 229–240.

Bachmann, F., Hielscher, R., Jupp, P. E., Pantleon, W., Schaeben, H. & Wegert, E. (2010). Inferential statistics of electron backscatter diffraction data from within individual crystalline grains. *Journal of Applied Crystallography* **43**, 1338–1355.

Barnes, J. D. & Sharp, Z. D. (2006). A chlorine isotope study of DSDP/ODP serpentinized ultramafic rocks: Insights into the serpentinization process. *Chemical Geology* **228**, 246–265.

Bedford, J., Fusseis, F., Leclère, H., Wheeler, J. & Faulkner, D. (2017). A 4D view on the evolution of metamorphic dehydration reactions. *Scientific Reports* **7**, 1–7.

Bezacier, L., Reynard, B., Bass, J. D., Sanchez-Valle, C. & Van de Moortèle, B. (2010). Elasticity of antigorite, seismic detection of serpentinites, and anisotropy in subduction zones. *Earth and Planetary Science Letters*. Elsevier B.V. **289**, 198–208.

Bostock, M. G., Hyndman, R. D., Sondenay, S. & Peacock, S. M. (2002). An inverted continental Moho and serpentinization of the forearc mantle. **417**, 536–538.

Boudier, F., Baronnet, A. & Mainprice, D. (2010). Serpentine mineral replacements of natural olivine and their seismic implications: Oceanic lizardite versus subduction-related antigorite. *Journal of Petrology* **51**, 495–512.

Boyd, F. R. & England, J. L. (1965). The rhombic enstatite-clinoenstatite inversion. *Carnegie Institution Yearbook* **64**, 117–120.

Bozhilov, K. N., Green II, H. W. & Dobrzhinetskaya, L. (1999). Clinoenstatite in Alpe Arami Peridotite: Additional Evidence of Very High Pressure. *Science* **284**, 128–132.

Bromiley, G. & Pawley, A. (2003). The stability of antigorite in the systems MgO-SiO2-H2O (MSH) and MgO-Al2O3-SiO2-H2O (MASH): The effects of Al3+ substitution on high-pressure stability. *American Mineralogist* **88**, 99–108.

Brown, W.L. and Smith, J. V. (1963). High-temperature x-ray studies on the polymorphism. *Zeitschrift fur Kristallographie* **212**, 186–212.

Bunge, H. J. (1993). Texture Analysis in Materials Science: Mathematical Methods. , 593.

Chen, S., Hiraga, T. & Kohlstedt, D. L. (2006). Water weakening of clinopyroxene in the dislocation creep regime. *Journal of Geophysical Research: Solid Earth* **111**, 1–14.

Chernak, L. J. & Hirth, G. (2010). Deformation of antigorite serpentinite at high temperature and pressure. *Earth and Planetary Science Letters*. Elsevier B.V. **296**, 23–33.

Clément, M., Padrón-Navarta, J. A., Tommasi, A. & Mainprice, D. (2018). Non-hydrostatic stress field orientation inferred from orthopyroxene (Pbca) to low-clinoenstatite (P21/c) inversion in partially dehydrated serpentinites. *American Mineralogist* **103**, 993–1001.

Coe, R. S. (1970). The thermodynamic effect of shear stress on the ortho-clino inversion in enstatite and other coherent phase transitions characterized by a finite simple shear. *Contributions to Mineralogy and Petrology* **26**, 247–264.

Coe, R. S. & Kirby, S. H. (1975). The Orthoenstatite to Clinoenstatite Transformation by Shearing and Reversion by Annealing: Mechanism and Potential Applications. *Contributions to Mineralogy and Petrology* **52**, 29–55.

Coe, R. S. & Muller, W. F. (1973). Crystallographic orientation of clinoenstatite produced by deformation of orthoenstatite. *Science* **180**, 64–66.

Connolly, J. A. D. (1997). Devolatilization-generated fluid pressure and deformation-propagated fluid flow during prograde regional metamorphism. *Journal of Geophysical Research* **102**, 149–173.

Connolly, J. A. D. (2010). The mechanics of metamorphic fluid expulsion. *Elements* **6**, 165–172.

Coombs, D. S. (1993). Dehydration veins in diagenetic and very-low-grade metamorphic rocks: features of the crustal seismogenic zone and their significance to mineral facies. Journal of Metamorphic Geology 11, 389-399.

Coombs, D. S., Ellis, A. J., Fyfe, W. S. & Taylor, A. M. (1959). The zeolite facies, with comments on the interpretation of hydrothermal syntheses. Geochimica et Cosmochimica Acta 17, 53-107.

Dallwitz, W. B., Green, D. H. & Thompson, J. E. (1966). Clinoenstatite in a volcanic rock from the cape vogel area, papua. *Journal of Petrology* **7**, 375–403.

Das, S., Mukherjee, B. K., Basu, A. R. & Sen, K. (2015). Peridotitic minerals of the

Nidar Ophiolite in the NW Himalaya: sourced from the depth of the mantle transition zone and above. *Geological Society, London, Special Publications* **412**, 271–286.

Defant, M. J. & Drummond, M. S. (1993). Mount St. Helens: potential example of the partial melting of the subducted lithosphere in a volcanic arc. *Geology*, 547–550.

Demouchy, S. (2010). Diffusion of hydrogen in olivine grain boundaries and implications for the survival of water-rich zones in the Earth's mantle. *Earth and Planetary Science Letters*. Elsevier B.V. **295**, 305–313.

Demouchy, S., Mackwell, S. J. & Kohlstedt, D. L. (2007). Influence of hydrogen on Fe-Mg interdiffusion in (Mg,Fe)O and implications for Earth's lower mantle. *Contributions to Mineralogy and Petrology* **154**, 279–289.

Dietrich, V., Emmerman, R., Oberhänsli, R. & and Puchelt, H. (1978). Geochemistry of basaltic and gabbroic rocks from the west Mariana trench. *Earth and Planetary Science Letters* **39**, 127–144.

Dilissen, N., Hidas, K., Garrido, C. J., Kahl, W.-A., Sánchez-Vizcaíno, V. L. & Padrón-Navarta, J. A. (2018). Textural evolution during high-pressure dehydration of serpentinite to peridotite and its relation to stress orientations and kinematics of subducting slabs: Insights from the Almirez ultramafic massif. *Lithos*. Elsevier B.V. **320**–**321**, 470–489.

Ding, X., Harlov, D. E., Chen, B. & Sun, W. (2018). Fluids , Metals , and Mineral / Ore Deposits. **2018**.

Eggler, D. H. & Ehmann, A. N. (2010). Rate of antigorite dehydration at 2 GPa applied to subduction zones. *American Mineralogist* **95**, 761–769.

Elliott, T., Plank, T., Zindler, A., White, W. & Bourdon, B. (1997). Element transport from to volcanic front at the Mariana arc. *Most* **102**, 14 991-15019.

Etheridge, M. A., Wall, V. J. & Vernon, R. H. (1983). The role of the fluid phase during regional metamorphism and deformation. *Journal of Metamorphic Geology* **1**, 205–226.

Etschmann, B., Brugger, J., Pearce, M. A., Ta, C., Brautigan, D., Jung, M. & Pring, A. (2014). Grain boundaries as microreactors during reactive fluid flow: Experimental dolomitization of a calcite marble. *Contributions to Mineralogy and Petrology* **168**, 1–12.

Evans, B. W. (2004). The Serpentinite Multisystem Revisited: Chrysotile Is Metastable. *International Geology Review* **46**, 479–506.

Ferry, J. M. (1980). A case study of the amount and distribution of heat and fluid during metamorphism. *Contrib. Mineral. Petrol.* **71**, 373–385.

Ferry, J. M. (1994). A historical review of metamorphic fluid flow. *Journal of Geophysical Research* **99**, 15487.

Ferry, J. M., Sorensen, S. S. & Rumble, D. (1998). Structurally controlled fluid flow during contact metamorphism in the Ritter Range pendant, California, USA. *Contributions to Mineralogy and Petrology* **130**, 358–378.

Frost, B. R. (1975). Contact metamorphism of serpentinite, chloritic blackwall and rodingite at paddy-go-easy pass, central cascades, Washington. *Journal of Petrology* **16**, 272–313.

Frost, B. R., Coe, R. S. & Okamura, F. P. (1978a). Principal stress directions from a natural occurrence of stress-induced clinoenstatite. *Contributions to Mineralogy and Petrology* **67**, 119–126.

Frost, B. R., Coe, R. S. & Okamura, F. P. (1978b). Principal stress directions from a natural occurrence of stress-induced clinoenstatite. *Contributions to Mineralogy and Petrology* **67**, 119–126.

Fyfe W.S., Turner, F.J., Verhoogen J. (1958). Metamorphic reactions and metamorphic facies. Geol. Soc. Am. Mem., 73, p. 259.

Fyfe, W. S. (1987). Tectonics, fluids and ore deposits: Mobilization and remobilization. *Ore Geology Reviews* **2**, 21–36.

Galvez, M. E., Connolly, J. A. D. & Manning, C. E. (2016). Implications for metal and volatile cycles from the pH of subduction zone fluids. *Nature*. Nature Publishing Group **539**, 420–424.

Galvez, M. E., Manning, C. E., Connolly, J. A. D. & Rumble, D. (2015). The solubility of rocks in metamorphic fluids: A model for rock-dominated conditions to upper mantle pressure and temperature. *Earth and Planetary Science Letters*. Elsevier B.V. **430**, 486–498.

Garrido, C. J., Sánchez-Vizcaíno, V. L., Gómez-Pugnaire, M. T., Trommsdorff, V., Alard, O., Bodinier, J. L. & Godard, M. (2005). Enrichment of HFSE in chlorite-harzburgite produced by high-pressure dehydration of antigorite-serpentinite: Implications for subduction magmatism. *Geochemistry, Geophysics, Geosystems* **6**.

Gasc, J., Schubnel, A., Brunet, F., Guillon, S., Mueller, H.-J. & Lathe, C. (2011). Simultaneous acoustic emissions monitoring and synchrotron X-ray diffraction at high pressure and temperature: Calibration and application to serpentinite dehydration. *Physics of the Earth and Planetary Interiors*. Elsevier B.V. **189**, 121–133.

Gay, A. & Migeon, S. (2017). Geological fluid flow in sedimentary basins Les. *Earth Science Bulletin* **188**, 6.

Greenwood, H. J. (1961). The system NaAlSi2O6-H2O-argon: Total pressure and water pressure in metamorphism. Journal of Geophysical Research 66, 3923-3946

Grover, J. (1972). The stability of low-clinoenstatite in the system Mg2Si2 O6 - CaMgSi2O6. *EOS, Transactions of the American Geophysical Union* **53**, 539.

Gualtieri, A. F., Giacobbe, C. & Viti, C. (2012). The dehydroxylation of serpentine group minerals. *American Mineralogist* **97**, 666–680.

Hacker, B. R. (2003). Subduction factory 2. Are intermediate-depth earthquakes in

subducting slabs linked to metamorphic dehydration reactions? *Journal of Geophysical Research* **108**.

Hanor, J. S. (1994). *Origin of saline fluids in sedimentary basins*. *Geological Society, London, Special Publications*.

Heinrich, C. A., Bain, J. H. C., Mernagh, T. P., Wyborn, L. A. I., Andrew, A. S. & Waring, C. L. (1995). Fluid and mass transfer during metabasalt alteration and copper mineralization at Mount Isa, Australia. *Economic Geology* **90**, 705–730.

Hielscher, R. & Schaeben, H. (2008). A novel pole **Figure** inversion method: specification of the *MTEX* algorithm. *Journal of Applied Crystallography*. International Union of Crystallography **41**, 1024–1037.

Hilairet, N., Reynard, B., Wang, Y., Daniel, I., Merkel, S., Nishiyama, N. & Petitgirard, S. (2007). High-Pressure Creep of Serpentine, Interseismic Deformation, and Initiation of Subduction. *Science* **318**, 1910–1913.

Horton, S. (2012). Disposal of Hydrofracking Waste Fluid by Injection into Subsurface Aquifers Triggers Earthquake Swarm in Central Arkansas with Potential for Damaging Earthquake. *Seismological Research Letters* **83**, 250–260.

Hyndman, R. D. & Peacock, S. M. (2003). Serpentinization of the forearc mantle. *Earth and Planetary Science Letters* **212**, 417–432.

Jabaloy-Sánchez, A., Gómez-Pugnaire, M. T., Padrón-Navarta, J. A., López Sánchez-Vizcaíno, V. & Garrido, C. J. (2015). Subduction- and exhumation-related structures preserved in metaserpentinites and associated metasediments from the Nevado-Filábride Complex (Betic Cordillera, SE Spain). *Tectonophysics*. Elsevier B.V. **644**, 40–57.

Jahn, S. & Martoňák, R. (2009). Phase behavior of protoenstatite at high pressure studied by atomistic simulations. *American Mineralogist* **94**, 950–956.

Jamtveit, B. & Hammer, Ø. (2012). Sculpting of Rocks by Reactive Fluids. *Geochemical Perspectives* **1**, 341–481.

Janecky, D. R. & Seyfried, W. E. (1986). Hydrothermal serpentinization of peridotite within the oceanic crust: Experimental investigations of mineralogy and major element chemistry. *Geochimica et Cosmochimica Acta* **50**, 1357–1378.

Jonas, L., John, T., King, H. E., Geisler, T. & Putnis, A. (2014). The role of grain boundaries and transient porosity in rocks as fluid pathways for reaction front propagation. *Earth and Planetary Science Letters*. Elsevier B.V. **386**, 64–74.

Jung, H., Green II, H. W. & Dobrzhinetskaya, L. F. (2004). Intermediate-depth earthquake faulting by dehydration embrittlement with negative volume change. *Nature* **428**, 545–549.

Kahl, W.-A., Dilissen, N., Hidas, K., Garrido, C. J., López-Sánchez-Vizcaíno, V. & Román-Alpiste, M. J. (2017). 3-D microstructure of olivine in complex geological materials reconstructed by correlative X-ray μ-CT and EBSD analyses. *Journal of Microscopy* **00**, 1–15.

Kawano, S., Katayama, I. & Okazaki, K. (2011). Permeability anisotropy of serpentinite and fluid pathways in a subduction zone. *Geology* **39**, 939–942.

Kelemen, P. B., Rilling, J. L., Parmentier, E. M., Mehl, L. & Hacker, B. R. (2003). *One view of the geochemistry of subduction-related magmatic arcs, with emphasis on primitive andesite and lower crust*. .

Khodyrev, O. Y. & Agoshkov, V. M. (1986). Phase transitions in serpentine in the MgO-SiO2 -H2 O system at 40–80 kbar. *Geochemistry International* **23**, 47–52.

Komatsu, M. (1980). Clinoenstatite in volcanic rocks from the Bonin Islands. *Contributions to Mineralogy and Petrology* **74**, 329–338.

Kyser, K. & Hiatt, E. E. (2003). Fluids in sedimentary basins: An introduction. *Journal of Geochemical Exploration* **80**, 139–149.

Lasaga, A. C. (1989). Fluid flow and chemical reaction kinetics in metamorphic systems: a new simple model. *Earth and Planetary Science Letters* **94**, 417–424.

Leclère, H., Faulkner, D., Llana-fúnez, S., Bedford, J. & Wheeler, J. (2018). Permeability and fluid pressure development during dehydration reactions. *Earth and Planetary Science Letters*. Elsevier B.V. **496**, 1–24.

Lienert, B. R. & Wasilewski, P. J. (1979). A magnetic study of the serpentinization process at Burro Mountain, California. *Earth and Planetary Science Letters* **43**, 406–416.

Llana-Funez, S., Brodie, K. H., Rutter, E. H. & Arkwright, J. C. (2007). Experimental dehydration kinetics of serpentinite using pore volumometry. *Journal of Metamorphic Geology* **25**, 423–438.

Llana-Fúnez, S., Wheeler, J. & Faulkner, D. R. (2012). Metamorphic reaction rate controlled by fluid pressure not confining pressure: Implications of dehydration experiments with gypsum. *Contributions to Mineralogy and Petrology* **164**, 69–79.

López Sánchez-Vizcaíno, V., Gómez-Pugnaire, M. T., Garrido, C. J., Padrón-Navarta, J. A. & Mellini, M. (2009). Breakdown mechanisms of titanclinohumite in antigorite serpentinite (Cerro del Almirez massif, S. Spain): A petrological and TEM study. *Lithos*. Elsevier B.V. **107**, 216–226.

López Sánchez-Vizcaíno, V., Rubatto, D., Gómez-pugnaire, M. T., Trommsdorff, V. & Müntener, O. (2001). Middle Miocene high-pressure metamorphism and fast exhumation of the Nevado- Filabride Complex , SE Spain. *Terra Nova* **13**.

López Sánchez-Vizcaíno, V., Trommsdorff, V., Gómez-Pugnaire, M. T., Garrido, C. J., Müntener, O. & Connolly, J. A. D. (2005). Petrology of titanian clinohumite and olivine at the high-pressure breakdown of antigorite serpentinite to chlorite harzburgite (Almirez Massif, S. Spain). *Contributions to Mineralogy and Petrology* **149**, 627–646.

Luth, R. W. (1995). Is phase A relevant to the Earth's mantle? *Geochimica et Cosmochimica Acta* **59**, 679–682.

Mainprice, D., Bachmann, F., Hielscher, R. & Schaeben, H. (2014). Descriptive tools for the analysis of texture projects with large datasets using MTEX: strength, symmetry and components. *Geological Society, London, Special Publications*.

Mainprice, D. & Ildefonse, B. (2009). Seismic Anisotropy of Subduction Zone Minerals–Contribution of Hydrous Phases. .

Malvoisin, B., Brunet, F., Carlut, J., Rouméjon, S. & Cannat, M. (2012). Serpentinization of oceanic peridotites: 2. Kinetics and processes of San Carlos olivine hydrothermal alteration. *Journal of Geophysical Research: Solid Earth* **117**, 1–13.

Manning, C. E. (2004). The chemistry of subduction-zone fluids. *Earth and Planetary Science Letters* **223**, 1–16.

Martinez-Martinez, J. M., Soto, J. I. & Balany, J. C. (2002). Orthogonal folding of extensional detachments: Structure and origin of the Sierra Nevada elongated dome (Betics, SE Spain). *Tectonics* **21**.

McCammon, C.A., 2005. The paradox of mantle redox. *Science* 308, 807.

Mei, S. (2000). Influence of water on plastic deformation of olivine aggregates 1 . Diffusion creep regime. *Cities* **105**.

Mellini, M. (1986). Chrysotile and Polygonal Serpentine from the Balangero Serpentinite. *Mineralogical Magazine* **50**, 301–305.

Merlet, C. (1994). An accurate computer correction program for quantitative electron probe microanalysis. *Mikrochimica Acta* **114–115**, 363–376.

Mével, C. (2003). Serpentinisation des péridotites abysales aux dorsales océaniques. *Comptes Rendus - Geoscience* **335**, 825–852.

Miller, S. A., van der Zee, W., Olgaard, D. L. & Connolly, J. A. D. (2003). A fluid-pressure feedback model of dehydration reactions: experiments, modelling, and application to subduction zones. *Tectonophysics* **370**, 241–251.

Moody, J. B. (1976). Serpentinization: a review. *Lithos* **9**, 125–138.

Morales, L. F. G., Mainprice, D. & Kern, H. (2018). Olivine-antigorite orientation relationships: Microstructures, phase boundary misorientations and the effect of cracks in the seismic properties of serpentinites. *Tectonophysics*. Elsevier **724–725**, 93–115.

Morales, M. J., Figueiredo e Silva, R. C., Lobato, L. M., Gomes, S. D., Gomes, C. C. C. O. & Banks, D. A. (2016). Metal source and fluid-rock interaction in the Archean BIF-hosted Lamego gold mineralization: Microthermometric and LA-ICP-MS analyses of fluid inclusions in quartz veins, Rio das Velhas greenstone belt, Brazil. *Ore Geology Reviews*. Elsevier B.V. **72**, 510–531.

Morimoto, N., Appleman, D. E. & Evans, H. T. (1960). The crystal structures of clinoenstatite and pigeonite. *Zeitschrift fur Kristallographie* **147**, 120–147.

Nagaya, T., Wallis, S. R., Kobayashi, H., Michibayashi, K., Mizukami, T., Seto, Y., Miyake, A. & Matsumoto, M. (2014). Dehydration breakdown of antigorite and the formation of B-type olivine CPO. *Earth and Planetary Science Letters*. Elsevier B.V. **387**, 67–76.

Nakamura, M. & Watson, E. B. (2001). Experimental study of aqueous fluid infiltration into quartzite: Implications for the kinetics of fluid redistribution and grain growth driven by interfacial energy reduction. *Geofluids* **1**, 73–89.

Nakashima, Y. (1995). Transport model of buoyant metamorphic fluid by hydrofracturing in leaky rock. *Journal of Metamorphic Geology* **13**, 727–736.

Ohashi, Y. (1984). Polysynthetically-twinned structures of enstatite and wollastonite. *Physics and Chemistry of Minerals* **10**, 217–229.

Okamoto, A., Shimizu, H., Fukuda, J. ichi, Muto, J. & Okudaira, T. (2017). Reaction-induced grain boundary cracking and anisotropic fluid flow during prograde devolatilization reactions within subduction zones. *Contributions to Mineralogy and Petrology*. Springer Berlin Heidelberg **172**, 1–23.

Padrón-Navarta, J. A., Hermann, J., Garrido, C. J., López Sánchez-Vizcaíno, V. & Gómez-Pugnaire, M. T. (2010a). An experimental investigation of antigorite dehydration in natural silica-enriched serpentinite. *Contributions to Mineralogy and Petrology* **159**, 25–42.

Padron-Navarta, J. A., Tommasi, A., Garrido, C. J. & Sanchez-Vizcaino, V. L. (2012). Plastic deformation and development of antigorite crystal preferred orientation in high-pressure serpentinites. *Earth and Planetary Science Letters* **349**, 75–86.

Padrón-Navarta, J. a., López Sánchez-Vizcaíno, V., Garrido, C. J., Gómez-Pugnaire, M. T., Jabaloy, a., Capitani, G. C. & Mellini, M. (2008). Highly ordered antigorite from Cerro del Almirez HP-HT serpentinites, SE Spain. *Contributions to Mineralogy and Petrology* **156**, 679–688.

Padrón-Navarta, J. A., Sánchez-Vizcaí, V. L., Garrido, C. J. & Gómez-Pugnaire, M. T. (2011). Metamorphic record of high-pressure dehydration of antigorite serpentinite to chlorite harzburgite in a subduction setting (Cerro del Almirez, Nevado-Filábride complex, Southern Spain). *Journal of Petrology* **52**, 2047–2078.

Padrón-Navarta, J. A., Sánchez-Vizcaíno, V. L., Hermann, J., Connolly, J. a D., Garrido, C. J., Gómez-Pugnaire, M. T. & Marchesi, C. (2013). Tschermak's substitution in antigorite and consequences for phase relations and water liberation in high-grade serpentinites. *Lithos*. Elsevier B.V. **178**, 186–196.

Padrón-Navarta, J. A., Tommasi, A., Garrido, C. J. & Mainprice, D. (2015). On topotaxy and compaction during antigorite and chlorite dehydration: an experimental and natural study. *Contributions to Mineralogy and Petrology*. Springer Berlin Heidelberg **169**, 1–20.

Padrón-Navarta, J. A., Tommasi, A., Garrido, C. J., Sánchez-Vizcaíno, V. L., Gómez-Pugnaire, M. T., Jabaloy, A. & Vauchez, A. (2010b). Fluid transfer into the wedge controlled by high-pressure hydrofracturing in the cold top-slab mantle. *Earth and Planetary Science Letters*. Elsevier B.V. **297**, 271–286.

Paterson, M. S. (1990). Rock deformation experimentation. *Geophysical Monograph*.

Pattison, D. R. M., de Capitani, C. & Gaidies, F. (2011). Petrological consequences of variations in metamorphic reaction affinity. *Journal of Metamorphic Geology* **29**, 953–977.

Peacock, S. M. (2001). Are the lower planes of double seismic zones caused by serpentine dehydration in subducting oceanic mantle? *Geology* **29**, 299–302.

Pedrosa, E. T., Putnis, C. V. & Putnis, A. (2016). The pseudomorphic replacement of marble by apatite: The role of fluid composition. *Chemical Geology*. Elsevier B.V. **425**, 1–11.

Perrillat, J. P., Daniel, I., Koga, K. T., Reynard, B., Cardon, H. & Crichton, W. a. (2005). Kinetics of antigorite dehydration: A real-time X-ray diffraction study. *Earth and Planetary Science Letters* **236**, 899–913.

Plümper, O., John, T., Podladchikov, Y. Y., Vrijmoed, J. C. & Scambelluri, M. (2017). Fluid escape from subduction zones controlled by channel-forming reactive porosity. *Nature Geoscience* **10**, 150–156.

Proctor, B. & Hirth, G. (2015). Role of pore fluid pressure on transient strength changes and fabric development during serpentine dehydration at mantle conditions: Implications for subduction-zone seismicity. *Earth and Planetary Science Letters*. Elsevier B.V. **421**, 1–12.

Pruess, K. (2008). On CO2 fluid flow and heat transfer behavior in the subsurface, following leakage from a geologic storage reservoir. *Environmental Geology* **54**, 1677–1686.

Putnis, A. (2002). Mineral replacement reactions: from macroscopic observations to microscopic mechanisms. *Mineralogical Magazine* **66**, 689–708.

Putnis, A. (2015). Transient Porosity Resulting from Fluid – Mineral Interaction and its Consequences. *Reviews in Mineralogy and Geochemistry* **80**, 1–23.

Putnis, A. & John, T. (2010). Replacement processes in the earth's crust. *Elements* **6**, 159–164.

Putnis, A. & Putnis, C. V. (2007). The mechanism of reequilibration of solids in the presence of a fluid phase. *Journal of Solid State Chemistry* **180**, 1783–1786.

Raleigh, C. B. and Talbot, J. L. (1967). Mechanical twinning in naturally and experimentally deformed diopside. *American Journal of Science* **265**, 151–165.

Raleigh, C. B., Kirby, S. H., Carter, N. L. & Lallemant, H. G. A. (1971). Slip and the clinoenstatite transformation as competing rate processes in enstatite. *Journal of Geophysical Research* **76**, 4011–4022.

Raleigh, C. B. & Paterson, M. S. (1965). Experimental deformation of serpentinite and its tectonic implications. *Journal of Geophysical Research* **70**, 3965.

Reynard, B. (2013). Serpentine in active subduction zones. *Lithos*. Elsevier B.V. **178**, 171–185.

Ruiz-Agudo, E., Putnis, C. V. & Putnis, A. (2014). Coupled dissolution and precipitation at mineral-fluid interfaces. *Chemical Geology*. Elsevier B.V. **383**, 132–146.

Ruiz Cruz, M. D., Puga, E. & Nieto, J. M. (1999). Silicate and oxide exsolution in pseudo-spinifex olivine from metaultramafic rocks of the Betic ophiolitic association: A TEM study. *American Mineralogist* **84**, 1915–1924.

Rutter, E. H. & Brodie, K. H. (1988). Experimental "sytectonic" dehydration of serpentinite under conditions of controlled pore water pressure. **93**, 4907–4932.

Rutter, E. H. & Brodie, K. H. (1995). Mechanistic interactions between deformation and metamorphism. *Geological Journal* **30**, 227–240.

Rutter, E. H., Llana-Fúnez, S. & Brodie, K. H. (2009). Dehydration and deformation of intact cylinders of serpentinite. *Journal of Structural Geology* **31**, 29–43.

Scambelluri, M., Rampone, E. & Piccardo, G. B. (2001). Fluid and element cycling in subducted serpentinite: A trace-element study of the Erro-Tobbio high-pressure ultramafites (Western alps, NW Italy). *Journal of Petrology* **42**, 55–67.

Schmidt, M. W. & Poli, S. (2013). *Devolatilization During Subduction*. *Treatise on Geochemistry: Second Edition*. Elsevier Ltd.

Schwartz, S., Guillot, S., Reynard, B., Lafay, R., Debret, B., Nicollet, C., Lanari, P. & Auzende, A. L. (2013). Pressure–temperature estimates of the lizardite/antigorite transition in high pressure serpentinites. *Lithos*. Elsevier B.V. **178**, 197–210.

Sclar, C.B., Carrison, L.C. & Schwartz, C. . (1964). High pressure stability fields of clinoenstatite, and the orthoenstatite- clinoenstatite transition. *EOS, Transactions of the American Geophysical Unionactions of the American Geophysical Union* **45**, 121.

Segall, P. (1989). Earthquakes triggered by fluid extraction. *Geology* **17**, 942–946.

Shiraki, K., Kuroda, N., Nurano, H. & Maruyama, S. (1980). Clinoenstatite in volcanic rocks from the Bonin Islands, Japan. *Nature* **285**, 30–32.

Thieme, M., Demouchy, S., Mainprice, D., Barou, F. & Cordier, P. (2018). Stress evolution and associated microstructure during transient creep of olivine at 1000–1200 °C. *Physics of the Earth and Planetary Interiors*. Elsevier **278**, 34–46.

Tommasi, A., Vauchez, A. & Ionov, D. A. (2008). Deformation, static recrystallization, and reactive melt transport in shallow subcontinental mantle xenoliths (Tok Cenozoic volcanic field, SE Siberia). *Earth and Planetary Science Letters* **272**, 65–77.

Trittschack, R. & Grobéty, B. (2013). The dehydroxylation of chrysotile: A combined in situ micro-Raman and micro-FTIR study. *American Mineralogist* **98**, 1133–1145.

Trittschack, R., Grobéty, B. & Koch-Müller, M. (2012). The lizardite phase transformation followed by in situ high-temperature Raman and FTIR spectroscopy. *American Mineralogist* **97**, 1965–1976.

Trommsdorff, H., Baker, V. & David, W. (1968). Inverse pole-**Figure**s of two carbonate fabrics. .

Trommsdorff, V. & Evans, B. W. (1972). Progressive metamorphism of antigorite schist in the Bergell tonalite aureole (Italy). *American Journal of Science*, 423–437.

Trommsdorff, V. & Evans, B. W. (1974). Alpine metamorphism of peridotitic rocks. *Schweizerische Mineralogische Und Petrographische Mitteilungen* **54**, 333–354.

Trommsdorff, V., Sanchez-Vizcaino, V. L., Gomez-Pugnaire, M. T. & Muntener, O. (1998). High pressure breakdown of antigorite to spinifex-textured olivine and orthopyroxene, SE Spain. *Contributions to Mineralogy and Petrology* **132**, 139–

148.

Trommsdorff, V. & Wenk, H. R. (1968). Terrestrial metamorphic clinoenstatite in kinks of bronzite crystals. *Contributions to Mineralogy and Petrology* **19**, 158–168.

Turner, F. J. (1953). Nature and dynamic interpretation of deformation lamellae in calcite of three marbles. *American Journal of Science*, 276–298.

Turner, F. J., Heard, H. & Griggs, D. T. (1960). Experimental deformation of enstatite and accompanying inversion to clinoenstatite. *Report of 21st International Geological Congress, Copenhagen* **18**, 399–408.

Ulmer, P. & Stalder, R. (2001). The Mg (Fe) SiO3 orthoenstatite-clinoenstatite transitions at high pressures and temperatures determined by Raman-spectroscopy on quenched samples. *American Mineralogist* **86**, 1267–1274.

Ulmer, P. & Trommsdorff, V. (1995). Serpentine stability to mantle depths and subduction-related magmatism. *Science (New York, N.Y.)* **268**, 858–861.

Ulmer, P. & Trommsdorff, V. (1999). Phase relations of hydrous mantle subducting to 300 km. *Mantle Petrology: Field Observations and High-Pressure Experimentation. Spec. Publ. Geochem. Soc. No. 6* 259–281.

Violay, M., Gibert, B., Azais, P., Pezard, P. A. & Lods, G. (2012). A New Cell for Electrical Conductivity Measurement on Saturated Samples at Upper Crust Conditions. *Transport in Porous Media* **91**, 303–318.

Viti, C. & Mellini, M. (1998). Mesh textures and bastites in the Elba retrograde serpentinites. *Eur. J. Mineral* **10**, 1341–1359.

Wada, I., Wang, K., He, J. & Hyndman, R. D. (2008). Weakening of the subduction interface and its effects on surface heat flow, slab dehydration, and mantle wedge serpentinization. *Journal of Geophysical Research: Solid Earth* **113**, 1–15.

Walther, J. V. & Orville, P. M. (1982). Volatile production and transport in regional metamorphism. *Contributions to Mineralogy and Petrology* **79**, 252–257.

Wang, W. H. & Wong, T. F. (2003). Effects of reaction kinetics and fluid drainage on the development of pore pressure excess in a dehydrating system. *Tectonophysics* **370**, 227–239.

Wheeler, J. (1987). The significance of grain scale stresses in the kinetics of metamorphism. *Contributions to Mineralogy and Petrology* **97**, 397–404.

Wicks, F. J. & Whittaker, E. J. W. (1977). Serpentine Texture and Serpentinization. *Canadian Mineralogist* **15**, 459–488.

Wunder, B. & Schreyer, W. (1992). Metastability of the 10-A phase in the system MgO-SiO2-H2O (MSH). what about hydrous MSH phases in subduction zones? *Journal of Petrology* **33**, 877–889.

Wunder, B. & Schreyer, W. (1997). Antigorite: High-pressure stability in the system MgO□SiO2□H2O (MSH). *Lithos* **41**, 213–227.

Xia, F., Brugger, J., Chen, G., Ngothai, Y., O'Neill, B., Putnis, A. & Pring, A. (2009).

Mechanism and kinetics of pseudomorphic mineral replacement reactions: A case study of the replacement of pentlandite by violarite. *Geochimica et Cosmochimica Acta* **73**, 1945–1969.

Yamamoto, K. & Akimoto, S. (1977). The system MgO-SiO 2 -H 2 O at high pressures and temperatures; stability field for hydroxyl-chondrodite, hydroxyl-clinohumite and 10 A o -phase. *American Journal of Science*, 288–312.

Yasuda, M., Kitamura, M. & Morimoto, N. (1983). Electron microscopy of clinoenstatite from a boninite and a chondrite. *Physics and Chemistry of Minerals* **9**, 192–196.

Zhang, J. S., Dera, P. & Bass, J. D. (2012). A new high-pressure phase transition in natural Fe-bearing orthoenstatite. *American Mineralogist* **97**, 1070–1074.

Zhang, R. Y., Shau, Y. H., Liou, J. G. & Lo, C. H. (2002). Discovery of clinoenstatite in garnet pyroxenites from the Dabie-Sulu ultrahigh-pressure terrane, east-central China. *American Mineralogist* **87**, 867–874.

Zhang, R. Y., Shau, Y. H., Yang, J. S. & Liou, J. G. (2017). Discovery of clinoenstatite in the Luobusa ophiolitic mantle peridotite recovered from a drill hole, Tibet. *Journal of Asian Earth Sciences*.

ANNEXE

Scan d'une lame (3 cm x 4cm) d'une serpentinite pauvre en calcium de Val Malenco (Italie)

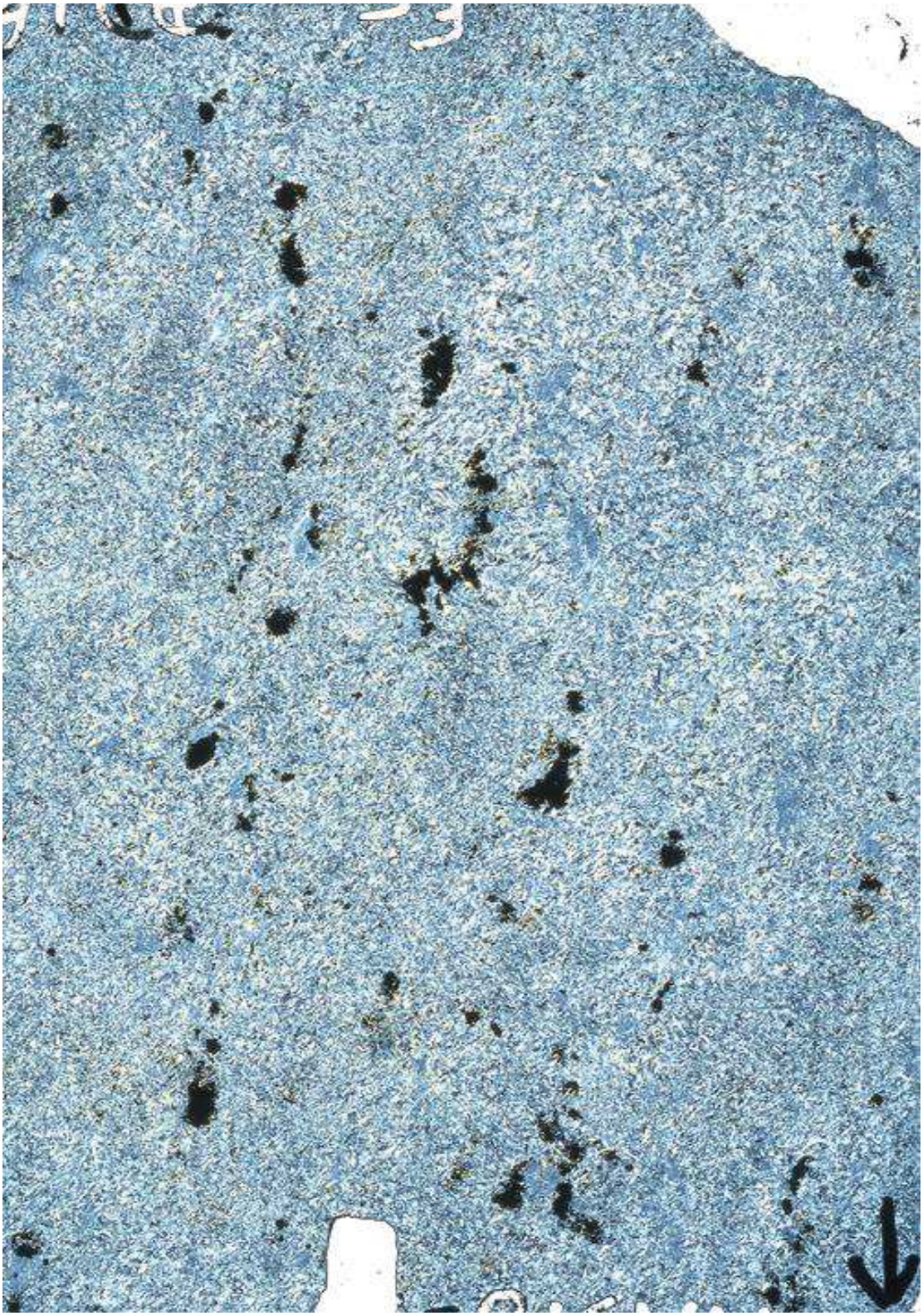

Scan d'une lame (3 cm x 4cm) d'une serpentinite riche en calcium de Val Malenco (Italie)

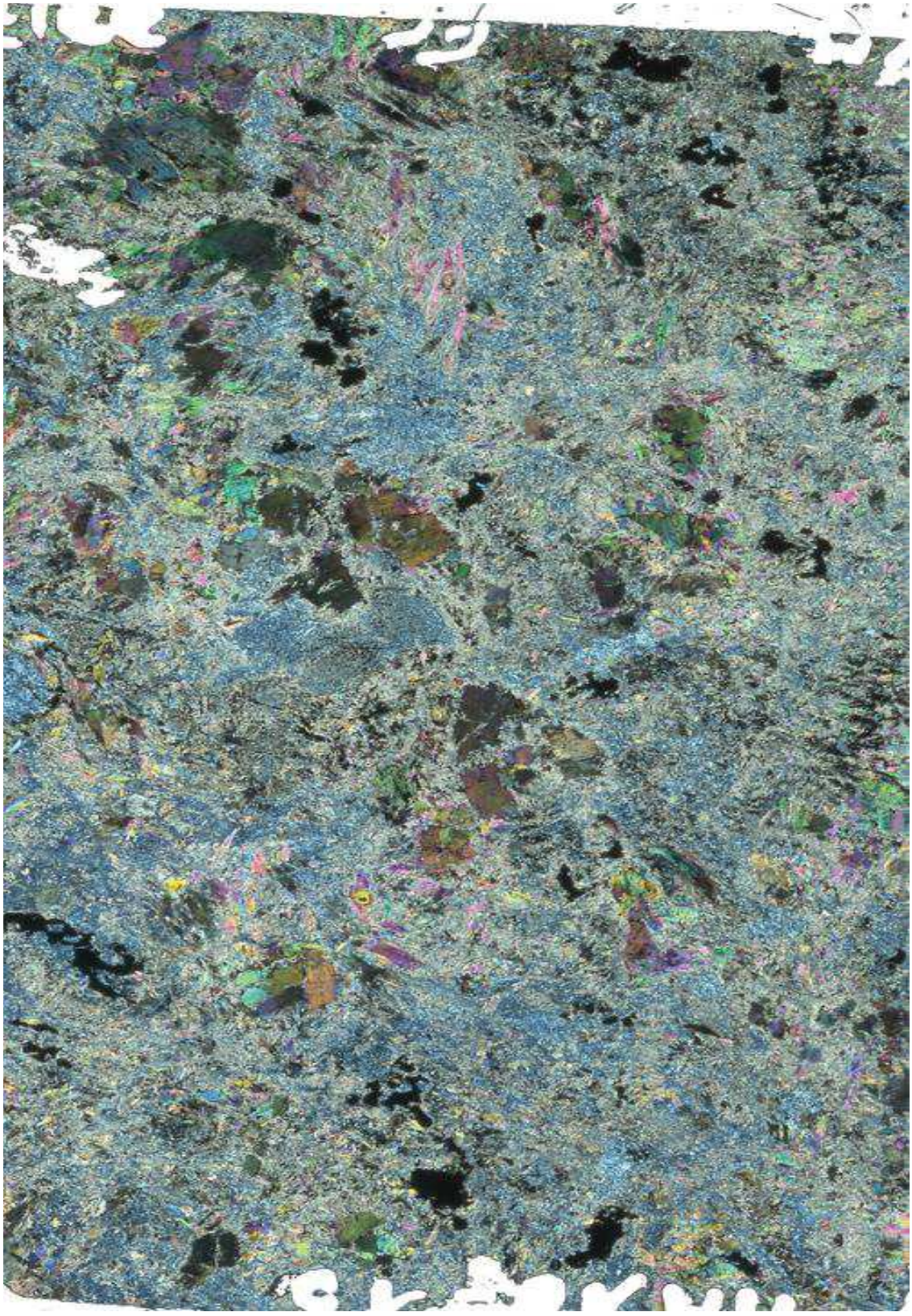

Scan d'une lame (3 cm x 4cm) de serpentinite riche en calcium de Val Malenco (Italie) partiellement réagie

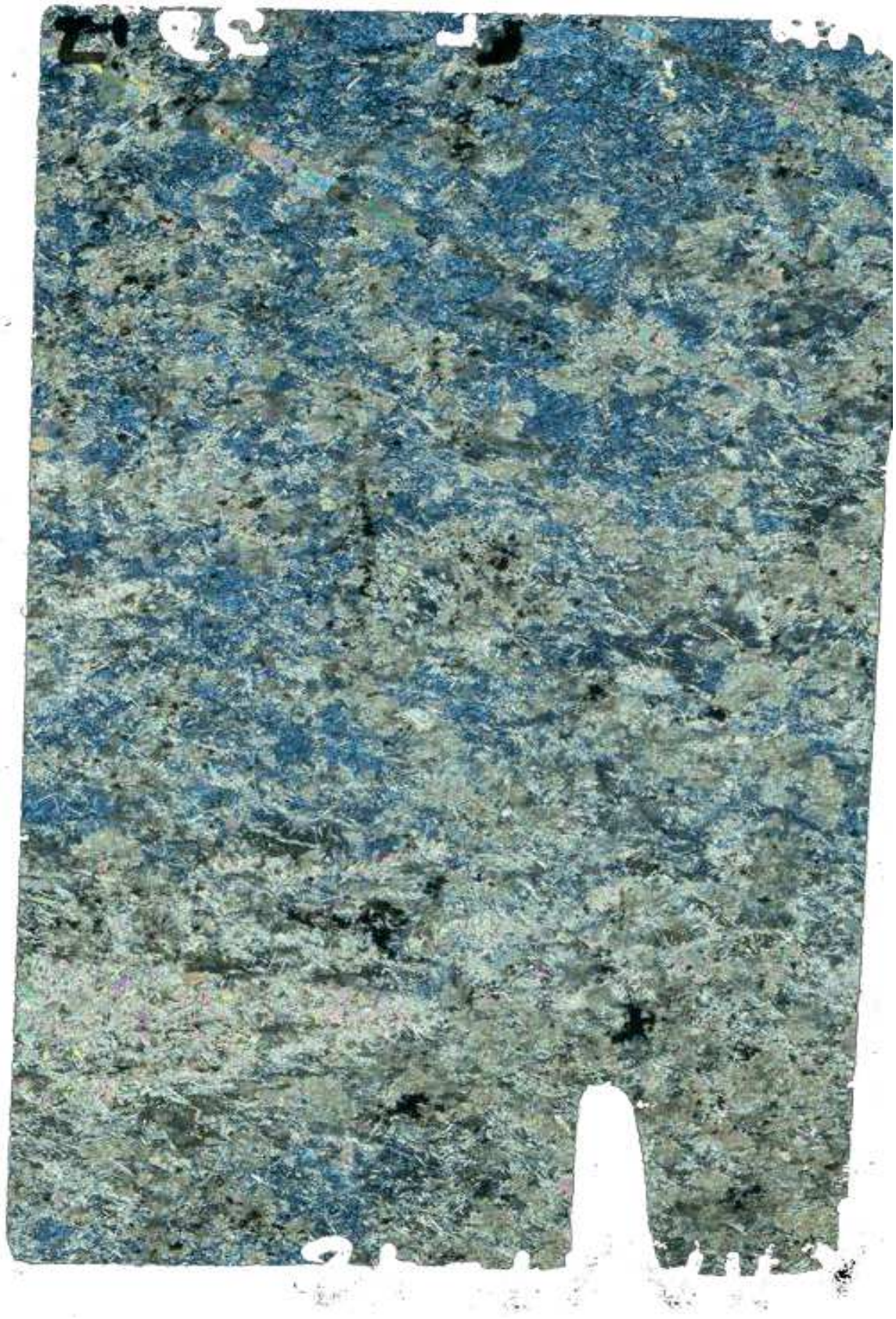

Scan d'une lame (3 cm x 4cm) d'une métapéridotite de Val Malenco (Italie)

Scan d'une lame (3 cm x 4cm) d'une métapéridotite riche en Ca-Al de Val Malenco (Italie)

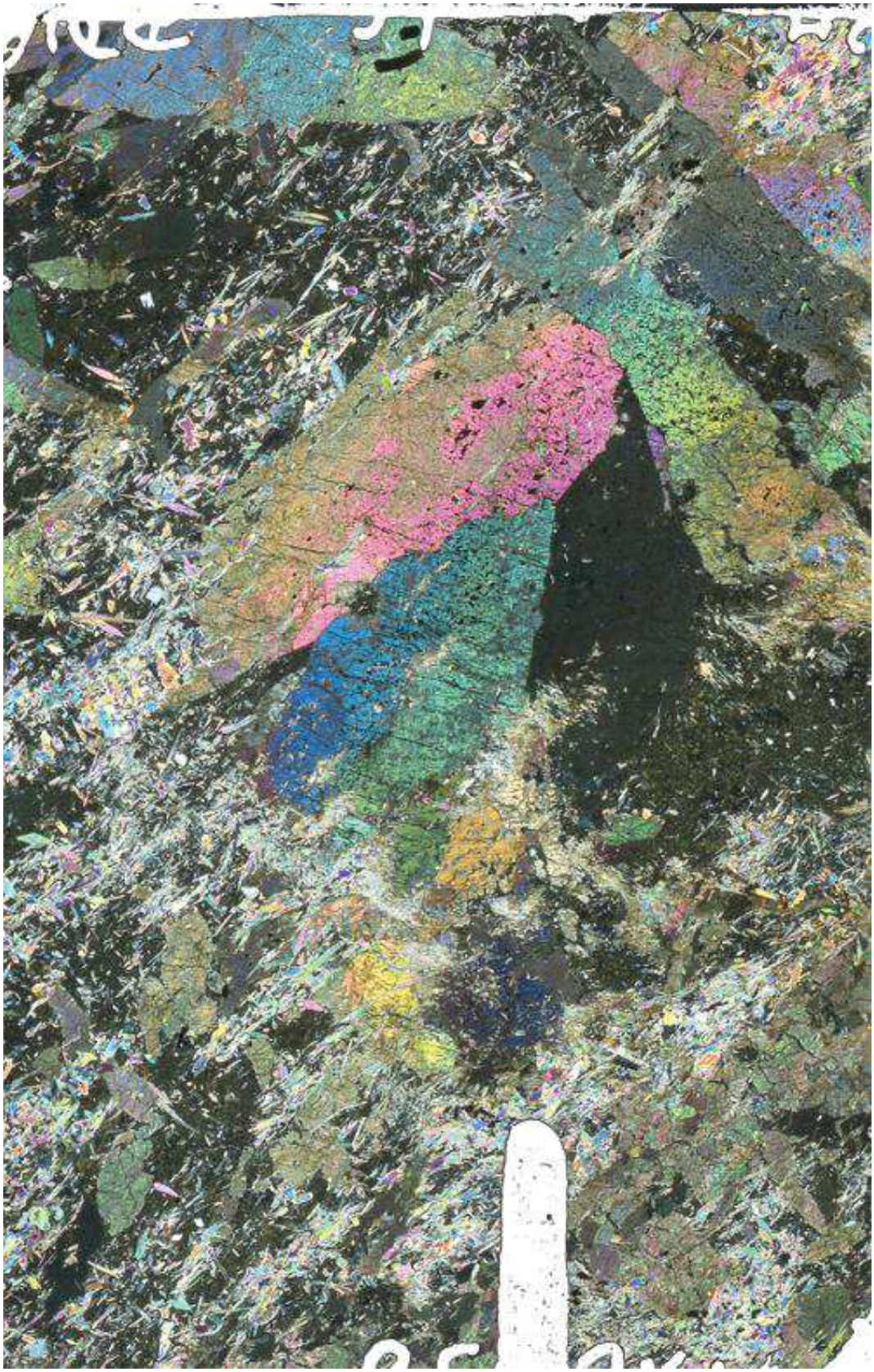

Table 6: Composition of mantelic and metamorphic diopside in representative samples from Valmalenco

	Ca-S		Ca-S		Ca-S		Mean	
Sample	MA16-63		MA16-59		MA16-23		Mantelic	Metamorphic
n	2	7	7	1	15	3		
SiO_2	51.83	53.67	52.81	54.92	51.04	54.83	51.89	54.47
TiO_2	0.54	0.02	0.16	0.00	0.83	0.02	0.51	0.01
Al_2O_3	4.54	0.18	4.09	0.03	4.18	0.02	4.27	0.07
Cr_2O_3	0.72	0.04	1.16	0.08	0.99	0.02	0.96	0.05
FeO	2.64	1.04	2.15	1.14	2.49	0.76	2.43	0.98
NiO	0.05	0.03	0.06	0.03	0.04	0.00	0.05	0.02
MgO	15.98	18.41	15.28	17.25	15.88	17.68	15.72	17.78
MnO	0.10	0.07	0.08	0.01	0.09	0.07	0.09	0.05
CaO	21.88	25.56	22.71	25.99	23.52	26.16	22.70	25.90
Na_2O	1.73	0.07	1.17	0.18	0.51	0.01	1.14	0.09
H_2O	0	0	0	0	0	0	0.00	0.00
Total	98.284	99.013	98.499	99.449	99.052	99.545	98.61	99.34
O	6.00	6.00	6.00	6.00	6.00	6.00	6.00	6.00
OH	0.00	0.00	0.00	0.00	0.00	0.00	0.00	0.00
Si	1.889	1.969	1.925	2.001	1.874	1.996	1.896	1.988
Ti	0.015	0.000	0.004	0.000	0.023	0.000	0.014	0.000
Al	0.195	0.008	0.176	0.001	0.181	0.001	0.184	0.003
Cr	0.021	0.001	0.033	0.002	0.029	0.000	0.028	0.001
Fe	0.081	0.032	0.066	0.035	0.076	0.023	0.074	0.030
Fe^{3+}	0.000	0.000	0.000	0.000	0.000	0.000	0.000	0.000
Ni	0.001	0.001	0.002	0.001	0.001	0.000	0.001	0.001
Mg	0.868	1.007	0.830	0.937	0.869	0.960	0.856	0.968
Mn	0.003	0.002	0.003	0.000	0.003	0.002	0.003	0.002
Ca	0.854	1.004	0.887	1.014	0.925	1.020	0.889	1.013
Na	0.122	0.005	0.083	0.013	0.036	0.000	0.080	0.006
Sum cation	4.050	4.029	4.008	4.004	4.017	4.003	4.025	4.012
XMg	0.915	0.969	0.927	0.964	0.919	0.976	0.920	0.970

Column in grey are composition of mantelic diopside
Cations were calculated with O= 6
Abbreviations are listed in Table 1

Table : Composition of Chlorite in representative samples from Valmalenco

Sample	S MA16-36	Js MA17-22	Js MA16-51	M MA17-36	M MA16-45	M MA16-46	M MA16-48	Al-M MA16-58	Al-M MA16-56
n	5	1	7	2	4	6	22	41	4
SiO_2	34.61	44.14	35.59	34.46	37.82	33.91	35.82	34.46	33.55
TiO_2	0.02	0.02	0.01	0.03	0.01	0.01	0.01	0.03	0.03
Al_2O_3	12.43	7.11	10.89	12.49	10.73	13.24	11.00	13.21	13.88
Cr_2O_3	1.45	1.76	1.77	2.94	2.08	1.11	1.79	0.92	0.24
FeO	3.24	3.62	4.13	3.30	3.13	3.53	3.20	3.81	5.89
NiO	0.22	0.14	0.14	0.15	0.19	0.21	0.17	0.09	0.22
MgO	34.13	32.91	33.60	35.09	34.72	35.39	34.89	34.84	32.14
MnO	0.02	0.02	0.03	0.02	0.03	0.02	0.02	0.02	0.03
CaO	0.01	0.01	0.01	0.01	0.01	0.01	0.02	0.16	0.01
Na_2O	0.00	0.05	0.02	0.02	0.02	0.00	0.01	0.01	0.01
H_2O	12.57	13.30	12.53	12.83	12.99	12.72	12.69	12.75	12.42
Total	98.71	103.04	98.70	101.31	101.71	100.16	99.61	100.30	98.41
O	28	28	28	28	28	28	28	28	28
OH	16	16	16	16	16	16	16	16	16
Si	6.604	7.961	6.812	6.442	6.969	6.395	6.767	6.482	6.477
Ti	0.002	0.002	0.002	0.004	0.002	0.002	0.002	0.005	0.004
Al	2.796	1.511	2.459	2.751	2.347	2.944	2.454	2.930	3.159
Cr	0.219	0.251	0.267	0.435	0.303	0.165	0.268	0.137	0.036
Fe	0.517	0.545	0.662	0.515	0.485	0.556	0.507	0.600	0.951
Fe^{3+}	0.000	0.000	0.000	0.000	0.000	0.000	0.000	0.000	0.000
Ni	0.034	0.021	0.022	0.022	0.028	0.032	0.026	0.014	0.034
Mg	9.709	8.848	9.590	9.781	9.559	9.951	9.836	9.775	9.252
Mn	0.003	0.004	0.004	0.004	0.004	0.003	0.004	0.004	0.005
Ca	0.003	0.003	0.002	0.003	0.002	0.002	0.004	0.032	0.002
Na	0.001	0.019	0.006	0.008	0.006	0.000	0.005	0.005	0.003
Sum cation	19.887	19.165	19.826	19.965	19.706	20.049	19.873	19.982	19.923
XMg	0.949	0.942	0.935	0.950	0.952	0.947	0.951	0.942	0.907

Abbreviations are listed in Table 1

Cations were calculated with O= 28

Spectre de diffraction des rayons X de la serpentinite de Val Malenco déshydratée expérimentalement

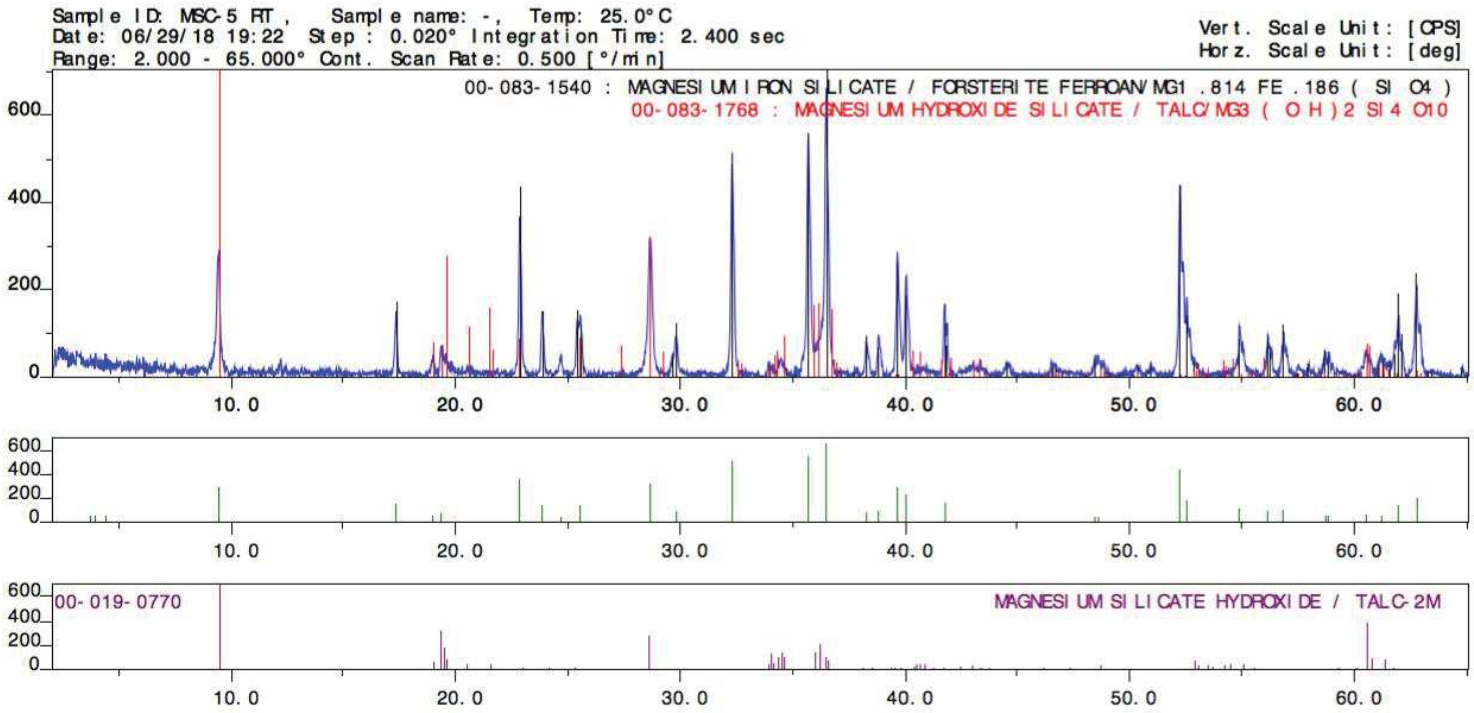

Script MTEX (Matlab) calculant l'orientation de la contrainte à partir de l'orientation de l'orthoenstatite

```
% MTEX version 4.5.2
%14/02/2018
% Script written by Maxime ClÈment, GÈoscience Montpellier, France.
%contact= maxime.clement@gm.univ-montp2.fr
clear all
close all
% define Oen crystal symmetry
cs = crystalSymmetry('mmm', [18.2406 8.8302 5.1852]);
%%%%%%%%%%%%%%%%%%%%%%%%%%%%%%%%%%%%%%%%%%%%%%%%%%%%%%%%%%%%%%%%%%%%%%%%%%%%
%% Example: define Oen Euler angles and variant vectors
%%%%%%%%%%%%%%%%%%%%%%%%%%%%%%%%%%%%%%%%%%%%%%%%%%%%%%%%%%%%%%%%%%%%%%%%%%%%
% Euler angles
E1=[0.8 177.6 173.3];
E2=[100.9 79.3 78.5];
E3=[0.9 179.2 0.4];
% variant vector
Var=[2 2 1];
% all 3 Oen orientations
ori=orientation('Euler',E1*degree,E2*degree,E3*degree,cs);
%%%%%%%%%%%%%%%%%%%%%%%%%%%%%%%%%%%%%%%%%%%%%%%%%%%%%%%%%%%%%%%%%%%%%%%%%%%%
%% compute the orientation of sigma
%%%%%%%%%%%%%%%%%%%%%%%%%%%%%%%%%%%%%%%%%%%%%%%%%%%%%%%%%%%%%%%%%%%%%%%%%%%%
% Define b-axes orientations of Oen
% positive and negative values plot in upper and lower
% hemisphere
% 3 orientations of Oen [010] in specimen coordinates
B=ori*Miller(0,1,0,cs,'uvw');%define b-axes of orthoenstatite as vectors
% calculation of sigma is done by rotating 45 degrees
% the Bunge Euler angles of Oen around around b-axis,
% For variant 1, rotation is + if B is +
% For variant 1, rotation is - if B is -
% For variant 2, rotation is - if B is +
% For variant 2, rotation is + if B is -
%
% Selection proceedure
for i=1:length(E1)
    if B(i).z>0 && Var(i)==1 || B(i).z<0 && Var(i)==2
        ori(i)=ori(i)*orientation('axis', ...
            Miller(0,1,0,cs),'angle',45*degree);
    else
        ori(i)=ori(i)*orientation('axis', ...
             Miller(0,1,0,cs),'angle',-45*degree);
    end
end
%%%%%%%%%%%%%%%%%%%%%%%%%%%%%%%%%%%%%%%%%%%%%%%%%%%%%%%%%%%%%%%%%%%%%%%%%%%%
%% plot sigma
% Red = Oen [001] lower hemisphere  Oen [001] lower hemisphere
%%%%%%%%%%%%%%%%%%%%%%%%%%%%%%%%%%%%%%%%%%%%%%%%%%%%%%%%%%%%%%%%%%%%%%%%%%%%
figure
% plot convention X-axis to east
plotx2east
for i=1:length(E1)
    if Var(i)==1
        plotPDF(ori(i),Miller(0,0,1,cs,'uvw'),...
            'lower','MarkerColor','blue','MarkerSize',16)
        hold on
    else
        plotPDF(ori(i),Miller(0,0,1,cs,'uvw'),...
```

```
            'lower','MarkerColor'...
            ,'red','MarkerSize',16)
        hold on
    end
end
% figure title
a=annotation('textbox',[0.420 0.939 0.174 0.055],'String',...
    'Sigma','LineStyle','none','BackgroundColor','white');
a.FontSize=20;
a=annotation('textbox',[0.015 0.815 0.175 0.179],'String',...
    'Blue: Variant 1 Red : Variant
2','LineStyle','none','BackgroundColor','white');
a.FontSize=20;
```